

A Toolbox for Exoplanet Exploration

Thesis by
Rebecca Jensen-Clem

In Partial Fulfillment of the Requirements for the
Degree of
Doctor of Philosophy

The logo for the California Institute of Technology (Caltech), featuring the word "Caltech" in a bold, orange, sans-serif font.

CALIFORNIA INSTITUTE OF TECHNOLOGY
Pasadena, California

2017
Defended May 18, 2017

© 2017

Rebecca Jensen-Clem
ORCID: 0000-0003-0054-2953

All rights reserved

ACKNOWLEDGEMENTS

I can only begin this thesis by thanking my parents and sister for their unending love and support. From the first living room conversation about black holes, to book signings, to keeping me sane as a harried student, I couldn't ask for better guides through this strange cosmos.

This thesis is also made possible by my many wonderful mentors in high school and college. I would like to thank Steve Murphy, John Heil, Peter Saxby, David Trowbridge, and Don McCarthy for encouraging my early interest in astronomy and helping me build a foundation of physics. At MIT, I was fortunate to learn from Jim Elliot, Matt Smith, and Sara Seager; I will always be grateful for their mentorship and generosity.

At Caltech, I've had the amazing good fortune of being advised by Shri Kulkarni. I can't imagine grad school without his wisdom and perspective, and I'm a better scientist for having him as an example. I am also grateful to have had the opportunity to work with Dimitri Mawet. His expertise, open door, and encouragement have been a continuous source of positivity. Thank you to Lynne Hillenbrand, Sterl Phinney, and Evan Kirby for many useful conversations and support throughout grad school. Thank you also to Kent Wallace for continuous mentorship and friendship throughout my time at Caltech.

I would also like to thank the many collaborators who have enriched the science in this thesis, among them Mike Bottom, Phil Muirhead, Ben Mazin, Seth Meeker, Rich Dekany, Jennifer Milburn, Carlos Gomez Gonzalez, Olivier Absil, James Graham, Max Miller-Blanchaer, Dmitry Duev, Reed Riddle, Christoph Baranec, and the staff at Palomar, Kitt Peak, and Keck Observatories.

I would like to thank my wonderful friends and fellow astro grads for always being there with movie nights, gym classes, and Red Door trips. In particular, I'd like to thank Marta Bryan: the best friend, officemate, and possible twin I could ever ask for.

Finally, thank you to Daniel for everything.

ABSTRACT

In this thesis, I develop a new suite of tools to address two questions in exoplanet science: how common are Earth-mass planets in the habitable zones of Solar-type stars, and can we detect signs of life on other worlds?

Answering the first question requires a method for detecting Earth-Sun analogs. Currently, the radial velocity (RV) method of exoplanet detection is one of the most successful tools for probing inner planetary systems. However, degeneracy between a spectrometer's wavelength calibration and the astrophysical RV shift has limited the sensitivity of today's instruments. In my thesis, I address a method for breaking this degeneracy: by combining a traditional spectrometer design with a dynamic interferometer, a fringe pattern is generated at the image plane that is highly sensitive to changes in the radial velocity of the target star. I augmented previous theoretical studies of the method, creating an end-to-end simulation to 1) introduce and recover wavelength calibration errors, and 2) investigate the effects of interferometer position errors on the RV precision. My simulation showed that using this kind of interferometric system, a 5-m class telescope could detect an Earth-Sun analog.

Addressing the occurrence rate of Earth twins also requires an understanding of planet formation in multiple star systems, which encompass half of all Solar-type stars. Gravitational interactions between binary components separated by 10 – 100 AU are predicted to truncate the outer edges of their respective disks, possibly reducing the disks' lifetimes. Consequently, the pool of material and the amount of time available for planet formation may be smaller than in single star systems. The stars' rotational periods provide a fossil record of these events: star-disk magnetic interactions initially prevent a contracting pre-main sequence star from spinning up, and hence a star with a shorter-lived disk is expected to be spinning more quickly when it reaches the zero age main sequence. In order to conduct a large-scale multiplicity survey to investigate the relationship between stellar rotation and binary system properties (e.g. their separations and mass ratios), I contributed to the commissioning of Robo-AO, a robotic laser guide star adaptive optics system, at the Kitt Peak 2.1-m. After the instrument's installation, I wrote a data pipeline to optimize the system's sensitivity to close stellar companions via reference star differential imaging. I then characterized Robo-AO's performance during its first year of operations. Finally, I used Robo-AO to search for binaries among the 759

stars in the Pleiades with rotational periods measured using the photometric data of the re-purposed Kepler telescope, K2.

Detecting signs of life on other worlds will require detailed characterization of rocky exoplanet atmospheres. Polarimetry has long been proposed as a means of probing these atmospheres, but current instruments lack the sensitivity to detect the starlight reflected and polarized by such small, close-in planets. However, the latest generation of high contrast imaging instruments (e.g. GPI and SPHERE) may be able to detect the polarization of thermal emission by young, gas giants due to scattering by aerosols in their atmospheres. Observational constraints on the details of clouds physics imposed by polarized emission will improve our understanding of the planets' compositions, and hence their formation histories. For the case of the brown dwarf HD19467 B orbiting a nearby Sun-like star, I demonstrated that the Gemini Planet Imager can detect linear polarizations on the order predicted for these cloudy exoplanets. My current pilot programs can produce the first detections of polarized exoplanet emission, while also building expertise for reflected starlight polarimetry with future observatories.

PUBLISHED CONTENT AND CONTRIBUTIONS

Jensen-Clem, R., D. A. Dey, et al. (2017). “The Performance of the Robo-AO Laser Guide Star Adaptive Optics System at the Kitt Peak 2.1-m Telescope”. In: *ArXiv e-prints*. arXiv: 1703.08867 [astro-ph.IM].

R. J.-C. contributed to the installation of the instrument, developed the faint star pipeline, developed the high contrast pipeline, contributed to the analysis of the weather and telescope jitter data, and contributed to the preparation of the manuscript.

Jensen-Clem, R., D. Mawet, et al. (2017, Submitted). “A New Standard for Assessing the Performance of High Contrast Imaging Systems”. In: *The Astronomical Journal*.

R. J.-C. participated in the conception of the project, performed the analysis, and prepared the manuscript.

Jensen-Clem, R., M. Millar-Blanchaer, et al. (2016). “Point Source Polarimetry with the Gemini Planet Imager: Sensitivity Characterization with T5.5 Dwarf Companion HD 19467 B”. In: *The Astrophysical Journal* 820, 111, p. 111. DOI: 10.3847/0004-637X/820/2/111. arXiv: 1601.01353 [astro-ph.EP].

R. J.-C. participated in the conception of the project, performed the post-GPI-pipeline data analysis, and prepared the manuscript.

Jensen-Clem, R., P. S. Muirhead, et al. (2015). “Attaining Doppler Precision of 10 cm s⁻¹ with a Lock-in Amplified Spectrometer”. In: *Publications of the Astronomical Society of the Pacific* 127, p. 1105. DOI: 10.1086/683796. arXiv: 1510.05602 [astro-ph.IM].

R. J.-C. wrote the instrument simulation and prepared the manuscript.

TABLE OF CONTENTS

Acknowledgements	iii
Abstract	iv
Published Content and Contributions	vi
Table of Contents	vii
List of Illustrations	ix
List of Tables	xviii
Chapter I: Introduction	1
1.1 Methods for Exoplanet Detection and Characterization	2
1.2 Technology for Exoplanet Imaging	10
Chapter II: Attaining Doppler Precision of 10 cm s^{-1} with a Lock-In Amplified Spectrometer	24
Abstract	25
2.1 Introduction	26
2.2 Theory	30
2.3 Simulation Architecture	31
2.4 Error Budget	34
2.5 The Feasibility of an Earth-Sun Analog Measurement	39
2.6 Conclusions	41
Acknowledgements	42
Chapter III: Point Source Polarimetry with the Gemini Planet Imager: Sensitivity Characterization with T5.5 Dwarf Companion HD 19467 B	43
Abstract	44
3.1 Introduction	45
3.2 Observations and Data Reduction	47
3.3 Polarimetric Analysis	49
3.4 Discussion	54
3.5 Conclusion	56
Acknowledgements	58
Chapter IV: A New Standard for Assessing the Performance of High Contrast Imaging Systems	59
Abstract	60
4.1 Introduction	61
4.2 Overview of Signal Detection Theory	61
4.3 Contrast Curves as Performance Metrics	65
4.4 Estimating the False Positive Fraction at Small Separations	67
4.5 Hypothesis Testing	74
4.6 Conclusion	74
Acknowledgments	76
4.7 Appendix: The Shapiro-Wilk Test	76

Chapter V: The Performance of the Robo-AO Laser Guide Star Adaptive Optics System at the Kitt Peak 2.1-m Telescope	78
Abstract	79
5.1 Introduction	80
5.2 Summary of the Robo-AO Imaging System	81
5.3 Data Reduction Pipelines	82
5.4 Site Performance	86
5.5 Adaptive Optics Performance	90
5.6 Data Archive	94
5.7 Near-infrared Camera	95
5.8 Conclusion	96
Acknowledgments	97
5.9 Appendix: Telescope Jitter	97
Chapter VI: The Effect of Companions on Stellar Angular Momentum in the Pleiades	101
Abstract	102
6.1 Introduction	103
6.2 Observations	105
6.3 Binary System Analysis	108
6.4 Discussion	111
6.5 Conclusion and Future Work	114
Chapter VII: Future Outlook	119
Bibliography	121

LIST OF ILLUSTRATIONS

<i>Number</i>	<i>Page</i>
1.1 The masses and separations of all exoplanets detected as of April 24th, 2017. The red points show planets detected using transits, the blue points radial velocities, the green points microlensing, and the magenta points direct imaging. This figure was generated using the Exoplanet Data Explorer at exoplanets.org (Han et al 2014).	2
1.2 A star (large filled circle) and planet (small black circle) are shown orbiting their mutual center of mass (black cross), with the star's spectrum represented schematically at the top of each panel. The observer is located at the bottom of the figure. When the star's velocity is entirely horizontal on the page, the observer sees no shift in the spectral features (first and third panels). When the star is moving away from the observer, the star's spectral features are redshifted (second panel). When the star is moving towards the observer, its spectral features are blueshifted (fourth panel). Hence, the periodic red and blue shift of the star's spectral features reveal the gravitational influence of the planet.	3
1.3 An illustration of a three dimensional Keplerian orbit. The labeled parameters are described in the main text. This figure is adopted from M. Perryman (2011).	3
1.4 A schematic illustration of the transit method of exoplanet detection and atmospheric characterization. Panel (a) shows a cartoon of a transit event as a planet passes in front of its host star. This event corresponds to the first flux diminution in the plot of stellar flux versus planet phase in panel (b). The second, smaller diminution corresponds to the occultation event. This figure is adapted from S. Seager and Deming (2010).	6
1.5 The flux as a function of wavelength for a solar system analog at 10 pc. This figure is adapted from S. Seager and Deming (2010).	8
1.6 The luminosity of stars, brown dwarfs, and planets are plotted as a function of age. Several directly imaged exoplanets are overplotted. This figure is adapted from Bonnefoy, Currie, et al. (2014).	9

1.7	The absolute H -band magnitude is plotted as function of $J - K$ color for various stars and brown dwarfs. Several directly imaged exoplanets are overplotted, with their color indicating their spectral type. This figure is adapted from B. P. Bowler (2016).	11
1.8	A circular aperture whose center is located at a distance R from a point of observation P (not to scale). This figure is inspired by Figure 4.2 in Hardy 1998.	12
1.9	A schematic of an adaptive optics system.	13
1.10	A schematic of a Lyot coronagraph optical setup. The lower part of the figure indicates the intensity patterns at the entrance pupil, first focal plane, second "Lyot" pupil plane, and second focal plane (Guyon, C. Roddier, et al. 1999, ©The Astronomical Society of the Pacific. Reproduced with permission. All rights reserved).	18
1.11	The planet-to-star contrast ratios achieved by current and future planet imaging instruments (black, red, and bold blue lines). Several young, massive planets that have already been detected in the near infrared are shown by the red dots. The open blue circles represent the visible-wavelength contrast ratios of planets that have been detected by the radial velocity method, but have not yet been directly imaged. The solar system planets at visible wavelengths are shown as black dots, with the thin blue curves representing different phase angles. This figure was adapted from Spergel et al. (2015).	19
1.12	An example of a post-AO, post-coronagraphic stellar point spread function (P1640/Nilsson, private communication). Many bright "speckles" are visible around the attenuated star in the center of the image. The speckles are slightly elongated due to the wide band-pass of the image ($\lambda_0 = 1.3 \mu\text{m}$, $\Delta\lambda = 25 \text{ nm}$). The four bright speckles are intentionally created in order to provide astrometric and photometric calibration sources.	20
2.1	A horizontal cut through Figure 2.2 reveals the simulated stellar spectrum. Note that for ease of viewing, Figure 2.2 shows the mean subtracted fringes.	32

- 2.2 A simulated mean subtracted spectrum vs. wavelength and $\Delta\tau$ for SNR = 500. The x-axis corresponds to wavelength, or pixels on the spectrometer detector. The y-axis corresponds to changes in the optical path difference of the interferometer, and therefore represents time as the interferometer optical path difference is modulated temporally. The regions of high fringe contrast correspond to absorption lines in the stellar spectrum. An error in the wavelength calibration is fundamentally different from a change in the radial velocity of the target star, as long as the wavelength calibration error does not occur during an interferometer scan. 33
- 2.3 Simulated likelihood contours describing the radial velocity and wavelength calibration error reconstructions for injected values of 1000 m s^{-1} and 500 m s^{-1} respectively, for SNR=100 and a spectral bandwidth of $\Delta\lambda = 88\text{\AA}$. In contrast to traditional RV reconstruction methods, the contours show an elliptical shape, demonstrating that the RV and wavelength calibration error measurements are not highly correlated. 35
- 2.4 Radial velocity precision is plotted against the signal-to-noise ratio for Poisson noise limited measurements, (no instrumental or astrophysical noise sources). Under these conditions, an SNR of about 94 per phase step, for 200 phase steps, is required to reach a precision of 10 cm s^{-1} . The RV precisions shown in this plot were calculated using a spectral bandwidth of $\Delta\lambda = 88\text{\AA}$, and were divided by $\sqrt{10}$ to reflect the RV precisions associated with the full V-band bandwidth of 880\AA 36
- 2.5 The radial velocity precision is shown to be approximately constant over 10 km s^{-1} ($\sim 0.2\text{\AA}$) wavelength calibration errors for SNR = 10, 100, and 1000. In contrast, the radial velocity precision is proportional to the wavelength calibration error in conventional spectroscopy. The RV precisions shown in this plot were calculated using a spectral bandwidth of $\Delta\lambda = 88\text{\AA}$, and were divided by $\sqrt{10}$ to reflect the RV precisions associated with the full V-band bandwidth of 880\AA . 37

2.6	The RV precision is plotted against the standard deviation of the phase step error. The horizontal dotted lines represent the Poisson limited RV precision for each SNR. In the phase step error limited regions, the RV precisions approach the limiting $SNR = \infty$ condition, shown by the black line. For $SNR = 100$, $\Delta\tau$ must be measured to less than 1 nm to reach the Poisson limited regime. Because the phase step errors are assumed to be uncorrelated, the total number of phase steps affects the final RV precision. In this simulation, we chose 200 steps (Table 2.1). The RV precisions shown in this plot were calculated using a spectral bandwidth of $\Delta\lambda = 88\text{\AA}$, and were divided by $\sqrt{10}$ to reflect the RV precisions associated with the full V-band bandwidth of 880\AA	38
3.1	The reduced Stokes images with the ring of comparison apertures superimposed (the white arrow indicates the companion in Stokes I). The companion's SNR (Equation 3.1) is 7.4 in Stokes I, but $SNR < 1.0$ in Stokes Q and U. Hence, no polarized radiation is detected from the companion.	49
3.2	Histograms of the summed counts in the Stokes comparison apertures. The aperture size is equal to the full width at half maximum of the companion (3.44 pixels, or 0.049"). The Stokes I histogram (a) has an excess of higher values due to speckle noise. Because HD 19467 A is an unpolarized star, there is little flux at the companion's separation in the Q and U frames. The large spread in Q and U values is due in part to the small number of apertures used (66).	51
3.3	The probability density function of $p = \frac{\sqrt{Q^2+U^2}}{I}$, via Equation 3.6. The four fits are to skewed Gaussian, Rayleigh, Rice, and Hoyt distributions. All but the skewed Gaussian are special cases of Equation 3.4 for different values of the means and standard deviations of Q and U . The best fit is the Hoyt distribution.	55
4.1	The Confusion Matrix	62

- 4.2 (a) The normally distributed PDF of a noise source with a mean of zero and standard deviation of one. Here, the detection criterion is arbitrarily set to 3σ (dashed line), which corresponds to $x = 3$ for this distribution. Because the noise PDF falls above the detection threshold a fraction 0.001 of the time, the false positive fraction in this example is 0.001. (b) The Gaussian PDF of a signal source with a mean of $x = 3$ and a standard deviation of one. Because half of the signal distribution's area falls above the detection criterion, the true positive fraction is 0.5. 63
- 4.3 Black line: an ROC curve corresponding to a range of criteria applied to the noise and signal distributions in Figure 4.2. The (TPF, FPF) locations corresponding to criteria of $1\sigma - 3\sigma$ are labeled to demonstrate the trade-offs between these key parameters. We note that FPF values larger than 0.5 require a criterion that is less than the mean of the noise distribution. Because the noise is normally distributed in this example, such criteria are negative. Grey line: the equivalent ROC curve for a signal distribution centered at $x = 1$. Because the noise distribution was unchanged, the $1\sigma - 3\sigma$ criterion points are located directly under their equivalent on the black curve. 64
- 4.4 The number of resolution elements of width λ/D at a distance r from the central star is $2\pi r$, where here we consider only whole numbers of resolution elements. 68
- 4.5 (a) The performance map shows the astrophysical flux ratio versus the separation, color-coded by the true positive fraction. The solid black line represents the approximate TPF = 0.95 contour. (b) The classic 5σ contrast curve. The regions interior to the inner working angle of $2\lambda/D$ are shaded in gray. The key difference between the performance map and the contrast curve is that the contrast curve fixes the detection criterion for all separations, while the performance map fixes the number of false positives for all separations. Because the false positive fractions are calculated empirically, we obtain a minimum of one false positive per separation for the case of a single image. In order to access smaller numbers of false positives per separation, we must either break the observation into several final images (Figure 4.6), which sacrifices the sensitivity, or make use of historical data from the same instrument. 69

- 4.6 A performance map where the detection criteria have been chosen to produce 0.1 false positives per separation. This is achieved by breaking the original 200-frame observation into ten 20-frame observations and appending the resolution elements at each separation. Hence, the number of false positives is reduced at the expense of sensitivity. 73
- 4.7 Even though the Rayleigh distribution (scale parameter = 2) is highly skewed compared with the normal distribution, the Shapiro-Wilk test cannot reliably distinguish it from a normal distribution for the sample sizes shown here. For separations less than $15 \lambda/D$, the Shapiro-Wilk test gives the wrong outcome (fails to reject the null hypothesis) for more than half of all trials. 77
- 5.1 The bright star pipeline (a) produces a superior Strehl ratio for the $V= 8.84$ double star HIP55872 compared with (b) the faint star pipeline. For the $V= 15.9$ star 2MASSJ1701+2621, however, the bright star pipeline (c) fails to correctly center the PSF, leading to an erroneously bright pixel in the center. The faint pipeline (d) successfully shifts and adds this observation. 84
- 5.2 Examples of Robo-AO i' -band images at Kitt Peak (square root scaling). The full-frame ($36'' \times 36''$) images on the left are the globular cluster Messier 5 (top) and Jupiter (bottom). The images on the right are examples of bright single stars and stellar binaries with a range of separations and contrasts. 85
- 5.3 An example of the reduction steps in the “high contrast” pipeline for a z' observation of the star EPIC228859428. 86
- 5.4 Seasonal fiducial ($\lambda = 500$ nm; see §5.4) seeing measurements. Nightly median values were used to fit a monthly distribution. The fraction of nights with seeing data for each month is shown. The quartile values and the actual measured range are shown. 87
- 5.5 A histogram of the seeing measurements (all referenced to a wavelength $\lambda = 500$ nm) from December 2015 to March 2017. A zenith distance dependent correction has been applied. The 25th, 50th, and 75th percentile seeing values are indicated by the vertical lines. . . . 88
- 5.6 Histograms of the difference between the primary mirror and dome temperatures (solid) and the dome temperature minus the outside air temperature (dashed). 88

- 5.7 A “wind rose” showing a stacked polar histogram of wind speeds and directions from December 2015 through June 2016. The wind most frequently blows from the NW, N, and NE, which correspond to the more mountainous region towards the direction of the Mayall 4-m telescope. These also tend to be the direction of the high wind speeds while slower wind speeds most often come from the south, where the terrain is less mountainous. 89
- 5.8 The mean binned seeing versus the wind speed for December 2015 through June 2016. The error bars are the standard deviation of the seeing values in a given wind speed bin divided by the square root of the number of seeing measurements in the bin. For wind speeds over 20 mph, the seeing is degraded by up to 0.3”. 90
- 5.9 The Strehl ratio versus the measured seeing values for 21 February 2017 through 10 March 2017 in the i' and lp600 filters. 92
- 5.10 A 1D cut through the PSF of HIP56051 is plotted with two Moffat functions fit to the PSF core and halo, respectively. The dashed curve is a Gaussian distribution with a FWHM corresponding to the seeing measurement and an area equal to the observed PSF’s area. 92
- 5.11 The contrast as a function of distance from the central star for the i' and lp600 filters. The dashed lines show the best 10% contrast curves for each filter. 94
- 5.12 A 5.5 s image of GJ1116 taken in H-band with the near-infrared camera (linear stretch). 96
- 5.13 The power spectral densities of the mean subtracted RA target positions for each sub-exposure at Kitt Peak (a) and Palomar (b). The peak at ~ 3.7 Hz is present at Kitt Peak, but not at Palomar. The solid black lines show the theoretical power-law dependencies of the tilt: $f^{-2/3}$ at low frequencies, and f^{-2} for 1 – 10 Hz (Hardy, 1998). 98
- 5.14 For a test observation, the standard deviation along the semi-major and semi-minor axes of 2D Gaussian fits to each 0.116s sub-exposure are plotted versus the rotation angle of the Gaussian. Here, -90° (dashed black line) indicates that the semi-major axis lies along the RA-axis. Clearly, the PSF is elongated along the RA-axis. 99

5.15	The power spectral densities of the mean subtracted RA target positions for the Kitt Peak sub-exposures since the telescope control upgrade (22 February 2017 through 8 March 2017). The peak that was present in Figure 5.13a is eliminated.	99
5.16	Strehl ratios of the observations taken in i' as a function of the seeing scaled to 500 nm before (December 2015 through 22 February 2017; black points) and after (22 February 2017 through 10 March 2017; gray stars) the enhancements. Note the significant improvement for seeing under ≈ 1.1 arcseconds.	100
6.1	The observed angular velocities of solar-type pre-main sequence stars in clusters as a function of age. The circle indicates the Sun. The solid lines show a simulation of the angular velocity of the convective envelope, while the colored dotted lines represent the radiative core. The blue, green, and red colors indicate fast, medium, and slow rotator categories respectively. The black dashed lines show the rotational evolution assuming conservation of momentum starting with the same initial rotations as the blue and red lines. This figure is adapted from Gallet and Bouvier (2013).	104
6.2	A summary of the Robo-AO Pleiades observations selected for companion searches.	107
6.3	An example sequence of images showing the Robo-AO observation of EPIC 211078780 on 22 February 2017 in (a). The i' image was processed with the faint star pipeline. Panel (b) shows the simultaneously fit models to the primary and secondary stars, where each star was modeled as the sum of two Gaussian distributions. Panel (c) shows the difference between the observation and the model. Panel (d) plots the histogram of the primary-to-secondary flux ratio measurements generated by many realizations of Poisson noise in the original image. The corresponding empirical cumulative distribution function of the flux ratio measurements is shown in panel (e), where the dotted lines represent the 68% confidence interval.	111
6.4	This figure shows the best fit mass versus the best fit separation for the binary candidates identified with Keck/NIRC2 (red points) and Robo-AO (blue points).	112

- 6.5 A period-color diagram where the periodic Pleiades members are shown in gray (Rebull et al., 2016), the subset observed with Robo-AO are shown in cyan (single stars) and blue (binary candidates), and the subset observed with Keck/NIRC2 are shown in orange (single stars) and red (binary candidates). 113
- 6.6 Left: A histogram of periodic Pleiades observations by K2 (gray), Robo-AO (cyan), and Keck/NIRC2 (orange). Right: A histogram of Robo-AO and Keck/NIRC2 observations with the binaries marked in dashed lines. 114
- 6.7 All periodic Pleiades members observed with K2 (gray circles) and Robo-AO binary candidates (circles colored by the projected separation of the binary) for the color range $1.1 < (V - K_s)_0 < 3.7$ (FGK stars). The “slow” sequence (dark gray shaded region) includes stars with periods falling within 30% of the best fit lines shown in black. The “intermediate” sequence (medium gray shaded region) includes star with periods 30% to 87% shorter than the best fit lines. Finally, the “fast” sequence (light gray shaded region) are stars with periods more than 87% shorter than the best fit lines. 115
- 6.8 All periodic Pleiades members observed with K2 (gray circles) and Robo-AO binary candidates (circles colored by the projected separation of the binary) for the color range $4.0 < (V - K_s)_0 < 7.0$ (M stars). The black circles are the binned points to which the black line ($P \propto M^{1.5}$) is fit. 116

LIST OF TABLES

<i>Number</i>	<i>Page</i>
2.1 Simulation Parameters	34
2.2 Instrument-Specific Parameters	39
3.1 HD 19467 System Properties, After J. R. Crepp, J. A. Johnson, A. W. Howard, G. W. Marcy, Brewer, et al. (2014) and J. R. Crepp et al. (2015)	47
3.2 Degree of Linear Polarization Upper Limits	54
5.1 The Specifications of the Robo-AO Optical Detector at Kitt Peak. . .	81
5.2 The Robo-AO Error Budget	93
6.1 Robo-AO EMCCD Gain Values	107
6.2 Derived Parameters for Pleiades Binaries	116

Chapter 1

INTRODUCTION

The last thirty years of astronomy have seen a revolution in planetary science. In 1990, the only known planets were those in our own solar system; as of May 2017, nearly 3000 planets have been discovered. Among these many “exoplanets” are worlds unlike any found orbiting the Sun: Jupiter-mass planets with years as short as a day, rocky planets twice as massive as the Earth, and planets so giant that they have more in common with brown dwarfs than with Jupiter. This new menagerie of exoplanets, however, is missing the most familiar specimen: a temperate, Earth-mass planet orbiting a solar-type star.

Our task as students of exoplanet science is therefore two-fold: 1) to develop the technology to detect the full range of exoplanet masses and orbital parameters, and 2) to understand the formation, dynamics, and physical properties of the planets that are already known. Chapter 2 of this thesis addresses the first task by simulating the performance of a new method for detecting Earth-mass exoplanets with medium-sized telescopes. Chapter 4 proposes a new methodology for describing the performance of planet-imaging instruments and choosing optimal detection thresholds. Chapter 3 addresses the second task by investigating the use of a so-far unexploited observable in exoplanet science – polarization – to understand the clouds that shroud the atmospheres of the most massive exoplanets. Finally, Chapters 5 and 6 describe the performance of a newly commissioned instrument for high-acuity imaging and its application to the study of multiple star systems. With nearly half of all solar-type stars residing in such multiple systems, their origins and evolution have significant implications for planet formation.

The remainder of this introductory chapter describes the various ways that exoplanets are detected and characterized, with special attention paid to the techniques that will be referenced later in this thesis. Figure 1.1 sets the stage for this discussion by showing all currently known exoplanets on a plot of mass versus orbital separation, with the different detection techniques marked in different colors. The diversity of technologies and interpretive frameworks represented by Figure 1.1 is a testament to the ingenuity of generations of astronomers and engineers; it is an honor to join this on-going effort.

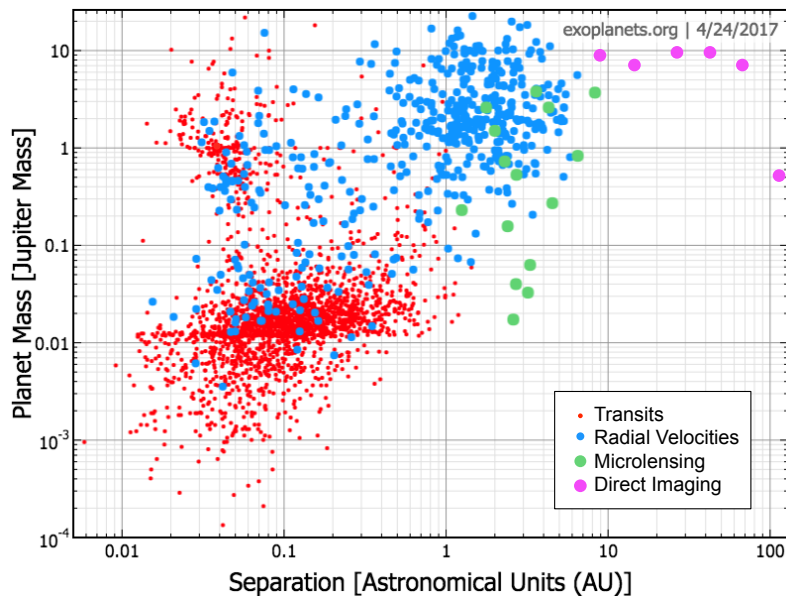


Figure 1.1: The masses and separations of all exoplanets detected as of April 24th, 2017. The red points show planets detected using transits, the blue points radial velocities, the green points microlensing, and the magenta points direct imaging. This figure was generated using the Exoplanet Data Explorer at exoplanets.org (Han et al 2014).

1.1 Methods for Exoplanet Detection and Characterization

The Radial Velocity Method

The radial velocity method of exoplanet detection refers to the periodic wavelength shift in a stellar spectrum that is induced by the star's line-of-sight motion as it orbits the star-planet center of mass (Figure 1.2). The relationship between the starlight's wavelength shift and the star's radial velocity is given by the Doppler effect:

$$\mathbf{k} \cdot \mathbf{v} = c \frac{\lambda_B - \lambda_0}{\lambda_0}, \quad (1.1)$$

where \mathbf{k} is the unit vector pointing from the observer to the star, \mathbf{v} is the velocity of the star, c is the speed of light, λ_B is the starlight's wavelength measured by an observer at our solar system's center of mass, and λ_0 is the starlight's wavelength in the rest frame of the star.

In order to derive the amplitude of a stellar radial velocity (RV) signal, we first consider the seven parameters describing the elliptical Keplerian orbit of a single body in a two-body system, where the system's center of mass is located at one of the foci of the ellipse (Figure 1.3). The semi-major axis and eccentricity of the ellipse are given by a and e , respectively. The body's orbital period is given by P , and the parameter t_p refers to a position of the body at a particular reference time.

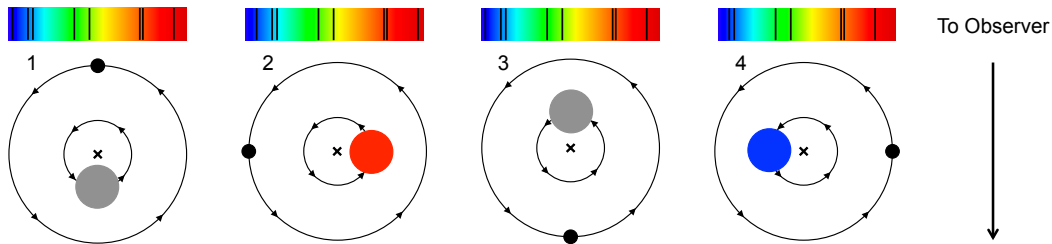


Figure 1.2: A star (large filled circle) and planet (small black circle) are shown orbiting their mutual center of mass (black cross), with the star's spectrum represented schematically at the top of each panel. The observer is located at the bottom of the figure. When the star's velocity is entirely horizontal on the page, the observer sees no shift in the spectral features (first and third panels). When the star is moving away from the observer, the star's spectral features are redshifted (second panel). When the star is moving towards the observer, its spectral features are blueshifted (fourth panel). Hence, the periodic red and blue shift of the star's spectral features reveal the gravitational influence of the planet.

The inclination i , longitude of the ascending node Ω , and argument of pericenter ω describe the projection of the three dimensional orbit onto the reference plane tangent to the observer's line of sight (the gray plane in Figure 1.3). We additionally define the true anomaly $\nu(t)$ as the time-dependent angle describing the body's location on the ellipse, and $z(t)$ as the body's height on the ellipse relative to the reference plane. Hence, $z(t)$ describes the body's motion along the observer's line of sight.

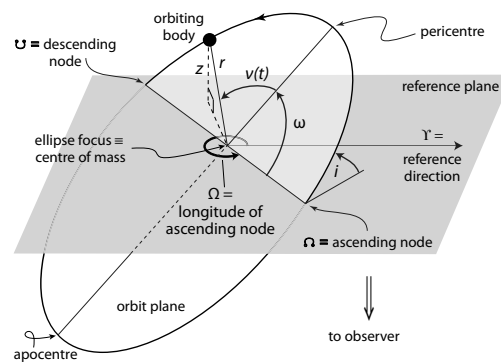


Figure 1.3: An illustration of a three dimensional Keplerian orbit. The labeled parameters are described in the main text. This figure is adopted from M. Perryman (2011).

Following M. Perryman (2011), if we consider Figure 1.3 to represent a star orbiting the center of mass of the planet-star system, the star's radial motion $z(t)$ is given by

$$z(t) = d(t) \sin i \sin(\omega + \nu(t)), \quad (1.2)$$

where $d(t)$ is the star's distance from the center of mass. Differentiating with respect to time and simplifying the result gives the radial velocity of the star:

$$v_r = K[\cos(\omega + \nu(t)) + e \cos \omega]. \quad (1.3)$$

Here, K is the semi-amplitude of the star's radial velocity. Substituting Kepler's laws gives a practical expression for K :

$$K = \frac{28.4329 \text{ m s}^{-1}}{\sqrt{1 - e^2}} \frac{m_2 \sin i}{M_{\text{Jup}}} \left(\frac{m_1 + m_2}{M_{\odot}} \right)^{-2/3} \left(\frac{P}{1 \text{ yr}} \right)^{-1/3}, \quad (1.4)$$

where m_1 is the mass of the star, m_2 is the mass of the planet, M_{Jup} is the mass of Jupiter, and M_{\odot} is the mass of the Sun. Using Kepler's third law, we can also express Equation 1.4 in terms of the planet's semi-major axis:

$$K = \frac{28.4329 \text{ m s}^{-1}}{\sqrt{1 - e^2}} \frac{m_2 \sin i}{M_{\text{Jup}}} \left(\frac{m_1 + m_2}{M_{\odot}} \right)^{-1/2} \left(\frac{a}{1 \text{ au}} \right)^{-1/2}. \quad (1.5)$$

A Jupiter-mass planet orbiting a solar-mass star at 5.0 au gives $K = 12.7 \text{ m s}^{-1}$, while an Earth-mass planet orbiting a solar-mass star at 1.0 au gives $K = 0.09 \text{ m s}^{-1}$.

If the planet is assumed to be much less massive than the star, and the star's mass is known, then fitting an observed radial velocity curve to K and e gives an estimate of the planet's minimum mass $m_2 \sin i$.

In the late 19th and early 20th Century, RV measurements were routinely employed to study stellar binaries and pulsations (Wilson, 1953). In 1952, University of California, Berkeley, astronomer Otto Struve suggested that RV measurements could be used to detect exoplanets. He wrote that "a planet might exist at a distance of 1/50 au ... causing the observed radial velocity of the star to oscillate with a range of 0.2 km/s - a quantity that might be just detectable" (Struve, 1952). It was not until 1995, however, that the first unambiguously planetary-mass companion was detected with the RV method: the $0.5 M_{\text{Jup}}$ planet orbiting the solar-type star 51 Pegasi b was the first of the 1000+ planets now discovered with RVs (Mayor and Queloz, 1995). While the radial velocity method continues to discover new exoplanets, its role as a follow-up technique is increasing in importance. This role will be discussed further in the transit method subsection below.

Figure 1.1 illustrates an important shortcoming of RV efforts to date: no planets with masses less than or equal to that of the Earth have yet been detected with the RV method. Detecting the radial velocity signals of such low-mass exoplanets is the subject of Chapter 2.

Additional Methods for Probing Exoplanet Masses

The radial velocity method is one among several techniques that are sensitive to exoplanet masses. While these additional techniques will not be discussed further in this thesis, they are briefly introduced below.

Figure 1.1 shows the ~ 20 planets that have been detected with gravitational microlensing. When two distant stars align radially from the perspective of the Earth, the gravitational influence of the foreground star bends the light of the background star. To the Earth-bound observer, the background star appears to temporarily brighten. For certain geometries, the gravity of a planet orbiting the foreground star will further brighten the image of the background star for a fraction of the duration of the full lensing event. These microlensing light curves can be used to reconstruct that planet's mass and orbital elements. The most important advantage of the microlensing technique is that it can detect planets at much larger distances from the Earth than any other method of exoplanet detection. Because it is a photometric technique, it is well-suited to monitoring many stars at one time. The principal disadvantages of the technique are that the microlensing events are non-repeating, and the planets it identifies cannot be followed up with other detection methods.

Exoplanets can also be detected by measuring the deflection of the parent star's position on the sky due to the gravitational influence of the planet. This astrometric technique produced the first claims of exoplanet detections in the 1940s (e.g. Strand, 1943). Unfortunately, these and all subsequent claims have been refuted with additional astrometric data and follow up with the radial velocity method. The space-based Gaia astrometric monitoring mission, however, is expected to identify tens of thousands of exoplanets by the end of its five-year mission (M. Perryman et al., 2014).

The Transit Method

An exoplanet transit occurs when a planet crosses the line of sight between the observer and the planet's host star (Figure 1.4). The planet is detected as a diminution of the starlight that recurs with the period of the planet's orbit. Assuming that the planet's nightside contributes negligible flux to the star-planet system, a full transit diminishes the starlight by the ratio of the planetary to stellar radii. In the infrared, sufficiently warm planets can also be detected as they pass behind their parent stars: during this "occultation" event, the total flux of the system is reduced as the planet's contribution is blocked by the star.

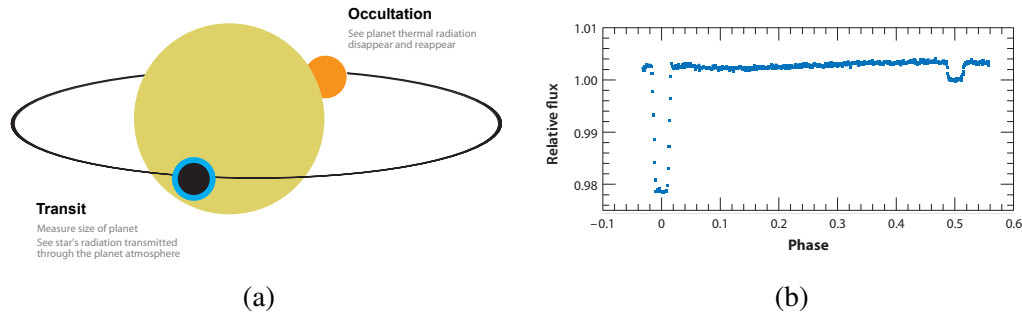


Figure 1.4: A schematic illustration of the transit method of exoplanet detection and atmospheric characterization. Panel (a) shows a cartoon of a transit event as a planet passes in front of its host star. This event corresponds to the first flux diminution in the plot of stellar flux versus planet phase in panel (b). The second, smaller diminution corresponds to the occultation event. This figure is adapted from S. Seager and Deming (2010).

Two years after the discovery of the first transiting exoplanet, D. Charbonneau, Brown, et al. (2002) detected the first exoplanet atmosphere: using the Hubble Space Telescope, the transit depth was observed to vary as a function of wavelength as the planet's atmosphere absorbed the starlight passing through it. Observations of planet occultations in the mid-IR also give spectroscopic results: as the occultation's depth varies with wavelength, features in the planet's thermal emission can be uncovered (e.g. D. Charbonneau, Allen, et al. 2005 and Deming, S. Seager, Richardson, et al. 2005). The Transiting Exoplanet Survey Satellite (TESS) mission, scheduled for launch in 2018, is designed to search for transiting exoplanets around bright stars – these will be the most favorable planets for transmission and emission spectroscopy studies in the future (Ricker, 2014).

The time between transits and occultations has also proven to be useful – Knutson et al. (2007) observed the first flux variations as the warm dayside of the transiting planet HD 189733 b rotated in and out of view. This “phase curve” measurement gave insight into the transport of heat between the tidally locked planet's perpetual day and night sides, revealing a hot spot displaced from the nearest point to the star.

Because the brightness of many stars can be monitored simultaneously with modern wide field imagers, the transit method is well suited to large-scale planet searches. From 2009 to 2013, the Kepler space telescope continuously monitored a 115 deg^2 region of the sky, identifying > 2300 transiting exoplanets (Borucki, D. Koch, et al., 2010; Batalha, 2014). While the Kepler mission was not sensitive to planets with years as long as the Earth's, the statistics of the many planets it did identify were

extrapolated to conclude that $5.7^{+1.7}_{-2.2}\%$ of Sun-like stars have an Earth-radius planet with an orbital period of 200 – 400 days (Petigura, A. W. Howard, and G. W. Marcy, 2013).

Since an observed transit ensures that the planet’s inclination is near zero, a detection of the same planet with the radial velocity method yields a powerful combination: the planet’s radius and mass, assuming that the host star’s mass and radius are also known. The bulk density given by these two values allows planets to be classified as gas giants (e.g. Jupiter), ice giants (e.g. Neptune), or rocky planets like the Earth.

Imaging

Direct imaging is perhaps the most intuitive method for exoplanet discovery and characterization: by detecting an exoplanet as a separate point source from its host star, the projected position and spectrum of the planet can be directly observed. Because direct imaging is currently the only method for obtaining spectra of non-transiting planets, its development is crucial to the success of the field – high resolution spectroscopy is required to probe the compositions of planets and their atmospheres. Furthermore, because the probability of transit decreases with the planet’s semi-major axis, direct imaging is particularly useful for obtaining spectra of exoplanets orbiting more than a few astronomical units from their host stars.

Direct imaging is challenging due to the combination of planets’ angular proximity to their host stars and the typically small planet-to-star flux ratios. Following S. Seager (2010), this flux ratio can be approximated as

$$\frac{f_p(i, \phi, \lambda)}{f_s(\lambda)} = p(\lambda) \left(\frac{R_p}{a} \right)^2 g(i, \phi) + \frac{B_\lambda(T_{\text{eff},p})R_p^2}{B_\lambda(T_{\text{eff},s})R_s^2}. \quad (1.6)$$

The first term on the right hand side of Equation 1.6 refers to the fraction of starlight reflected by the planet, where $p(\lambda)$ is the geometric albedo of the planet as a function of wavelength, R_p is the radius of the planet, a is the semi-major axis, and $g(i, \phi)$ is the phase function. If the planet is approximated as a fully reflecting, diffusively scattering sphere, $p(\lambda) = 2/3$. The phase function $g(i, \phi)$ gives the fraction of the planet’s disk that is illuminated by the star in terms of the orbital inclination i and the orbital phase ϕ . The second term on the right hand side of Equation 1.6 gives the relative contributions of the star and planet’s thermal radiations. Both objects are approximated as blackbodies with specific intensities B_λ given by the Plank function and effective temperatures $T_{\text{eff},s}$ and $T_{\text{eff},p}$ for the star and planet respectively.

To illustrate these contributions to the planet-to-star flux ratio, Figure 1.5 shows the flux of a solar system analog at a distance of 10 pc, where the Sun is approximated as a $T_{\text{eff}} = 5750$ K blackbody. The first hump in the maximum-phase planetary fluxes is due to reflected starlight (see the first term in Equation 1.6), where the reflected light flux ratio of the Earth-Sun analog reaches a maximum of about 10^{-10} . The second hump is due to the planets' thermal emission (see the second term in Equation 1.6). The Earth-Sun analog's flux ratio reaches a maximum of about 10^{-7} in the infrared.

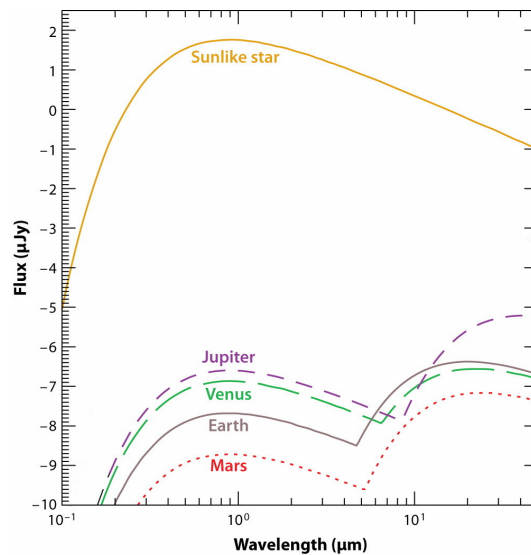


Figure 1.5: The flux as a function of wavelength for a solar system analog at 10 pc. This figure is adapted from S. Seager and Deming (2010).

At a distance of 10 pc, a planet with a semi-major axis of 1 au would appear at an angular separation of $0.1''$ from its parent star. Detecting such a planet is beyond the capabilities of current exoplanet imaging instruments. Section 1.2 explains the practical challenges and opportunities for such instruments.

Within the purview of modern instrumentation, however, is the direct imaging of young, massive planets located $\gtrsim 10$ au from their parent stars (see the pink dots on Figure 1.1). Unlike the ~ 4 Gyr Earth, whose infrared emission is dominated by re-radiated starlight, planets in the first ~ 100 Myrs of their lives thermally radiate their energy of formation and gravitational contraction.

Figure 1.6 plots models of the luminosity versus age of low mass stars, brown dwarfs, and planets of various masses, with several directly imaged planets and planet candidates indicated. All models plotted for $3 M_{\text{Jup}} - 2 M_{\text{Jup}}$ planets show

that their luminosity at 1 Myrs is more than an order of magnitude greater than their luminosity at 100 Myrs, emphasizing the advantageousness of young, massive planets for direct imaging studies. Indeed, the planet-to-star flux ratio of the directly imaged planet β Pictoris b (gray point on Figure 1.6) is 10^{-4} at $2.18 \mu\text{m}$ (Bonnefoy, Lagrange, et al., 2011).

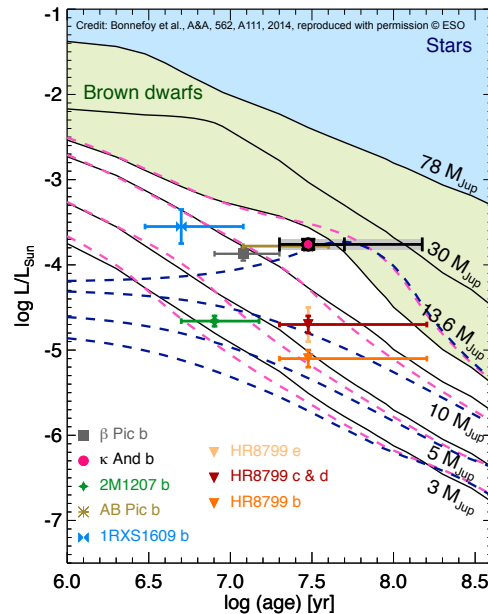


Figure 1.6: The luminosity of stars, brown dwarfs, and planets are plotted as a function of age. Several directly imaged exoplanets are overplotted. This figure is adapted from Bonnefoy, Currie, et al. (2014).

Figure 1.6 also illustrates several important questions raised by the discovery of $\sim 10 M_{\text{Jup}}$ substellar companions – namely, how these bodies formed, and what, if anything, distinguishes them from brown dwarfs. A simplistic division between brown dwarfs and giant planets is the $13 M_{\text{Jup}}$ mass cutoff for deuterium burning: in the absence of nuclear fusion at any point during its lifetime, perhaps a companion body could safely be called a planet. However, this demarcation was called into question with the discovery of the first directly imaged $M < 13 M_{\text{Jup}}$ companion: 2M1207–3932 b is a $\sim 5 M_{\text{Jup}}$ object at a distance of 41 au from a $25 M_{\text{Jup}}$ brown dwarf (Chauvin et al., 2004). While the lower mass companion certainly falls below the deuterium burning mass limit, the two bodies are similar enough in mass that they are likely to have formed like a binary star system via cloud fragmentation. Hence, a more robust division between planets and brown dwarfs may be their formation mechanisms – if a body formed from the circumstellar disk of its host

star, than perhaps it should be classified as a planet regardless of its fusion history.

The dotted pink and purple lines in Figure 1.6 represent two such models of planet formation. The pink lines represent the “hot start” model of planet formation, in which a gravitational instability in the disk leads to a rapid collapse to form a high-entropy gas giant planet (Stevenson, 1982; Burrows et al., 1997). The dotted purple lines indicate the “cold start” model, in which the comparatively slow accretion of solid materials leads to a lower-entropy rocky planet or gas giant planet with a rocky core (Pollack et al., 1996; Bodenheimer, Hubickyj, and Lissauer, 2000). Measuring the occurrence rates, metallicities, and luminosities of directly imaged planets at different ages can begin to distinguish between and refine the details of these formation paradigms.

Unfortunately, young, massive, widely-separated exoplanets are extremely rare: $< 4.1\%$ of FGK stars host a $5 - 13 M_{\text{Jup}}$ planet at $30 - 3000$ au (B. P. Bowler, 2016). This paucity of planets within the purview of current direct imaging instruments has hampered efforts to test planet formation scenarios.

The ~ 20 planetary mass companions that *have* been directly imaged, however, provide their own mysteries. Figure 1.7 shows a color-magnitude sequence of stars and brown dwarfs with directly imaged exoplanets shown in bold circles. It is clear that the planets are generally redder than the brown dwarf color-magnitude sequence, a fact first noted in 2008 with the discovery of the first directly imaged $M < 13 M_{\text{Jup}}$ planets orbiting a main sequence star (C. Marois, B. Macintosh, et al., 2008). This color difference is likely due to the planets’ retention of clouds at lower temperatures than brown dwarfs, as planets’ lower surface gravities affect their photospheric pressure. Chapter 3 discusses the use of polarimetry as a tool for studying clouds in the atmospheres of these directly imaged gas giant exoplanets.

1.2 Technology for Exoplanet Imaging

Exoplanet imaging relies on four key pieces of technology and methodology: adaptive optics, coronagraphy, observing strategies for differential imaging, and image post-processing. Starting with a discussion of the affect of atmospheric turbulence on telescope image quality, these four pieces are introduced below.

The Point Spread Function and Atmospheric Turbulence

If we consider light emitted by a star at a large distance from a circular aperture of radius a , then the wavefront at the aperture can be assumed to be flat. Under the

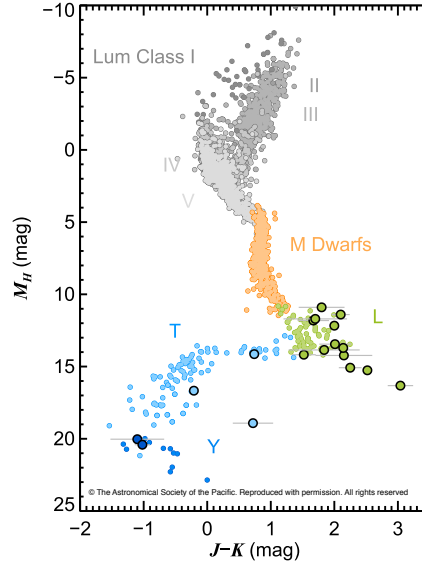


Figure 1.7: The absolute H -band magnitude is plotted as function of $J-K$ color for various stars and brown dwarfs. Several directly imaged exoplanets are overplotted, with their color indicating their spectral type. This figure is adapted from B. P. Bowler (2016).

Huygens-Fresnel principle, the wavefront at each area element dS in the circular aperture generates spherical wavelets propagating outwards. The electric field at point P , located at a distance $R \gg a$ from the center of the circular aperture, is then the sum of the spherical wavelets originating at all area elements on the circular aperture. A diagram of this setup is shown in Figure 1.8. Following Hardy (1998), the expression for this electric field at point P is given by Fraunhofer diffraction:

$$E(P) = \frac{E_A e^{i(\omega t - kR)}}{R} \iint_{\text{Aperture}} e^{ik(Yy - Xx)/R} dS, \quad (1.7)$$

where ω is the time frequency and $k = 2\pi/\lambda$ is the wavenumber of the radiation. The planewave also has a constant amplitude E_A at the aperture. Substituting for polar coordinates (ρ, θ) in the aperture plane and (r, Φ) in the plane of point P , Equation 1.7 can be re-written as

$$E(P) = \frac{E_A e^{i(\omega t - kR)}}{R} \int_0^a \rho \int_0^{2\pi} e^{i(k\rho r/R) \cos(\theta - \Phi)} d\rho d\theta. \quad (1.8)$$

We can simplify this expression using Bessel functions to give

$$E(P) = \frac{E_A e^{i(\omega t - kR)}}{R} 2\pi a^2 \left(\frac{R}{kar} \right) J_1 \left(\frac{kar}{R} \right), \quad (1.9)$$

where J_1 is a Bessel function of the first kind of order one. Finally, the intensity at point P is given by the time-averaged modulus square of the electric field. Substituting $r/R = \sin \beta$, this intensity is

$$I = \left(\frac{E_A^2 A^2}{2R^2} \right) \left(\frac{2J_1(ka \sin \beta)}{ka \sin \beta} \right)^2, \quad (1.10)$$

where A is the area of the aperture. This is the Airy function describing the diffraction pattern far from a circular aperture.

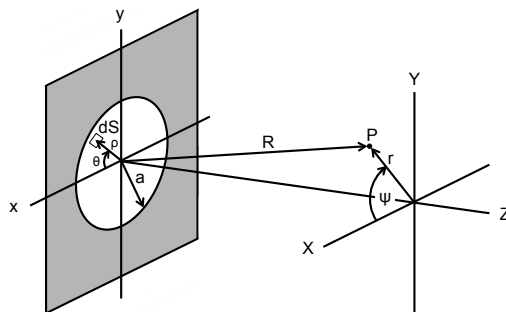


Figure 1.8: A circular aperture whose center is located at a distance R from a point of observation P (not to scale). This figure is inspired by Figure 4.2 in Hardy 1998.

If a focusing element (e.g. a lens or parabolic mirror) is co-located with the circular aperture, the flat wavefront entering the aperture will be made spherical by the focusing element and will converge to a focus while leaving the Airy diffraction pattern unchanged.

Unfortunately, a flat wavefront entering the Earth's atmosphere is no longer flat by the time it reaches a telescope aperture on the ground. This is primarily due to variations in the index of refraction of turbulent air pockets encountered by the wavefront as it propagates through the atmosphere. These different indices of refraction induce optical path length differences which distort the shape of the wavefront, imparting a random phase error on the light reaching the telescope:

$$\phi = \frac{2\pi}{\lambda} \int n ds, \quad (1.11)$$

where $n = N - \langle N \rangle$ represents the variations in the index of refraction N of the atmosphere and ds represents a unit of length through the atmosphere. Here, ϕ varies spatially across the wavefront. We can now define the mean square phase difference between two points on the wavefront separated by a distance r as

$$D_\phi(r) \equiv \langle [\phi(0) - \phi(r)]^2 \rangle, \quad (1.12)$$

where $D_\phi(r)$ is the phase structure function. Adopting a Kolmogorov model of atmospheric turbulence, the phase structure function can be more simply expressed as

$$D_\phi(r) = 6.88 \left(\frac{r}{r_0} \right)^{5/3}, \quad (1.13)$$

where r_0 , the Fried parameter, is the characteristic length scale of the turbulence (Fried, 1966). A telescope with an aperture diameter of r_0 would encounter a mean square wavefront error of 1 radian.

Due to interference between different parts of the wave, a short exposure point spread function will be composed of $\sim (D/r_0)^2$ “speckles,” each with a diameter of $\sim 1 \lambda/D$, occupying a circular region with a diameter of λ/r_0 . In a long exposure image, changes in the atmospheric turbulence will lead to a washed-out, roughly Gaussian-shaped disk with a full width at half maximum (FWHM) of $0.98\lambda/r_0$. The goal of an adaptive optics system is to flatten the distorted wavefront in order to bring the PSF back to its diffraction-limited Airy pattern.

Adaptive Optics

An adaptive optics (AO) system brings the point spread function closer to its diffraction limited shape by sensing and correcting wavefront distortions. A schematic of an AO system is shown in Figure 1.9.

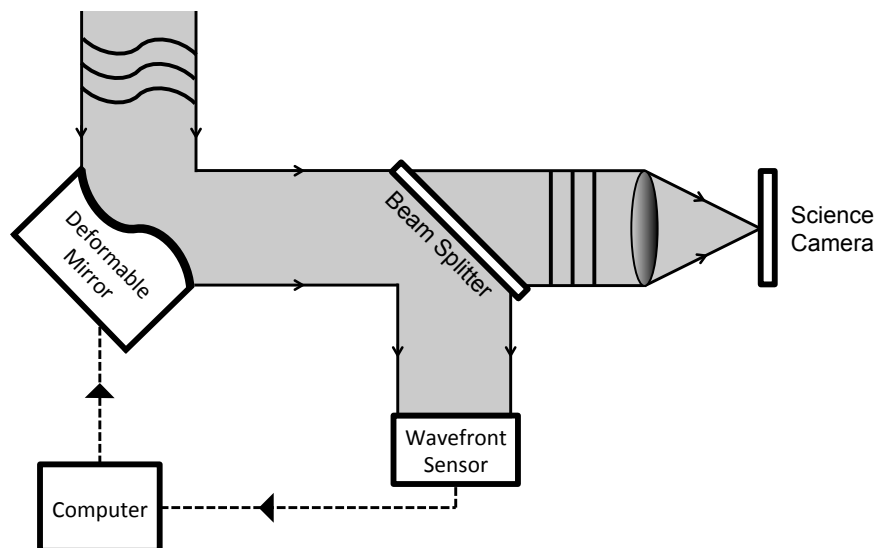


Figure 1.9: A schematic of an adaptive optics system.

The optical path length differences induced by the atmosphere can be mitigated by a deformable mirror (DM): if the shape of the aberrated wavefront is imposed on a

flexible mirror surface, the wavefront of the light bouncing off of that mirror will flat.

A common DM design consists of a continuous mirror surface with a number of piezoelectric actuators attached to the back side of the mirror. When voltage is applied to the actuators, they bend the surface of the mirror by an amount that is linearly proportional to the applied voltage. The advantages of this piezoelectric face-sheet DM class include a wide range of physical sizes and actuator densities, high amplitudes of mirror surface deformation (“stroke”), and high speeds of operation. Their disadvantages include temperature sensitivity and hysteresis. Adaptive optics systems such as PALM-3000 and Spectro-Polarimetric High-contrast Exoplanet Research (SPHERE) use this class of DMs (Beuzit et al., 2008; Dekany et al., 2013).

Other AO systems, such as Robo-AO and the Gemini Planet Imager (GPI) use micro electro-mechanical systems (MEMS) mirrors (B. A. Macintosh et al., 2008; Christoph Baranec, R. Riddle, A. Ramaprakash, et al., 2011). These mirrors are made using micro-lithography, and their surfaces are deformed using electrostatic forces rather than piezoelectric actuators. The relative ease and efficiency of MEMS DM manufacturing processes promise ever lower cost devices with higher actuator counts.

In practice, the post-DM beam is not perfectly corrected due to errors such as the DM’s finite number of deformable elements, the delay between the measurement and correction of the wavefront aberrations, and our knowledge of the shape of the wavefront. The fitting error, $\sigma_{\text{fitting}}^2$, refers to the limited ability of a deformable mirror with N actuators to correct for atmospheric turbulence with a scale parameter r_0 over a telescope diameter D :

$$\sigma_{\text{fitting}}^2 = k \left(\frac{D}{r_0} \right)^{5/3} N^{-5/6} \quad (1.14)$$

where the scaling value k depends on the details of the DM.

Wavefront sensing is accomplished by splitting off a portion of the light (often in a different wavelength than the intended science observations), and using specialized optics to transform the offending phase variations into intensity variations that can be recorded by a detector. A common wavefront sensor design is the Shack-Hartmann: a would-be flat wavefront is passed through a grid of small lenses to form a grid of points on a detector located the lenses’ focal length (J. Hartmann, 1900; Shack and

Platt, 1971). The displacement of the points gives a measure of the local slope of the wavefront.

While the Shack-Hartmann wavefront sensor is widespread among both general-purpose and exoplanet-centric AO systems (e.g. Robo-AO, PALM-3000, and the Gemini Planet Imager), it is not the ideal wavefront sensor for all situations. For example, the linear proportionality between the wavefront slope and the spot centroid breaks down for large-amplitude spot shifts. Other designs (e.g. the pyramid and Zernike wavefront sensors) have different sensitivity and linearity trade-offs. Guyon (2005) gives a comprehensive comparison of these different wavefront sensors.

For the case of a Shack-Hartmann wavefront sensor, the wavefront measurement error $\sigma_{\text{meas.}}^2$ is related to the signal-to-noise ratio (SNR) of the spots formed on the wavefront sensing detector behind the grid of lenses. Following Hardy (1998), if the diameter d of the individual lenses is roughly equal to r_0 and the spot size on the detector is λ/d , the measurement error can be approximated as

$$\sigma_{\text{meas.}}^2 = \frac{6.3}{\text{SNR}}. \quad (1.15)$$

The SNR must be carefully traded with the wavefront sensor integration time, which is linked to the total time lag τ_s between sensing and correcting the wavefront. For the simplified case of a single turbulent layer following Kolmogorov statistics, the temporal wavefront error is given by

$$\sigma_{\text{temporal}}^2 = 28.4 (\tau_s f_G)^{5/3}, \quad (1.16)$$

where $f_G = 0.427v/r_0$ is the Greenwood frequency for a turbulent atmospheric layer with wind velocity v (Greenwood, 1977).

The combination of Equations 1.15 and 1.16 demonstrate the importance of a bright wavefront reference source: a very dim source (e.g. a faint star) requires a longer integration time on the wavefront sensor detector to reduce the measurement error, but a longer integration time increases the temporal error term. In such cases where the science target star is too dim to meet the required wavefront error budget, a nearby brighter star can be used as the wavefront reference source. However, the angular separation between the science and reference stars means that they will experience slightly different wavefront aberrations as their light moves through the atmosphere, leading to an imperfectly corrected science star. The wavefront error due to this ‘‘angular anisoplanatism’’ effect is given by

$$\sigma_{\text{angular anisoplanatism}}^2 = \left(\frac{\theta}{\theta_0} \right), \quad (1.17)$$

where θ_0 depends on the details of the turbulence statistics, but is generally $15'' - 20''$ at $2 \mu\text{m}$ (Hardy, 1998).

If there is no astrophysical reference source that is bright enough and close enough to yield satisfactory values of $\sigma_{\text{meas.}}^2$ and $\sigma_{\text{angular anisoplanatism}}^2$, we must turn to artificial bright, locatable reference sources.

In the late 1970s and 1980s, the United States government sponsored the development of laser beacons to act as bright guide sources for AO systems built for satellite imaging and high altitude laser energy transfer (Hardy, 1998). Converging with the conclusions of parallel unclassified efforts, these early explorations led to the deployment of two classes of laser guide stars: Rayleigh beacons, in which laser light focused at 10 - 20 km is returned to the telescope by elastic scattering, and sodium beacons, which induce the fluorescence of sodium atoms at 90 km. In both cases, the laser light returning to the AO system travels through a subset of the atmosphere that has affected the astrophysical source originating from above the atmosphere. The wavefront error due to this ‘‘cone effect,’’ or focal anisoplanatism, is given by

$$\sigma_{\text{focal anisoplanatism}}^2 = \left(\frac{D}{d_0} \right), \quad (1.18)$$

where D is the diameter of the telescope and d_0 is the reference diameter over which the wavefront error from focal anisoplanatism is 1 radian² depending on the wavelength of measurement and the zenith angle. Equation 1.18 demonstrates that focal anisoplanatism plays a larger role for telescopes of larger diameters. Hence, most 8 – 10 m-class telescopes employ sodium beacons. Rayleigh beacons, which are lower cost and simpler to operate than sodium beacons, are better suited to AO systems on smaller telescopes.

The above discussion can thus be consolidated into a single wavefront error budget for adaptive optics systems:

$$\sigma_{\text{resid.}}^2 = \sigma_{\text{fitting}}^2 + \sigma_{\text{temporal}}^2 + \sigma_{\text{meas.}}^2 + \sigma_{\text{anisoplanatism}}^2 + \sigma_{\text{other}}^2. \quad (1.19)$$

Other sources of wavefront error contributing to Equation 1.19 might include residual tip and tilt, which reduce the peak intensity of the corrected PSF by smearing the core over an area wider than λ/D , and wavefront errors in the science focal plane due to unsensed aberrations introduced after the wavefront sensing beam has been split off from the science beam.

Coronagraphy

We now return to the topic of directly imaged planetary mass companions orbiting nearby stars. It is clear that adaptive optics improves our sensitivity to faint companions at small angular separations from a star because AO moves the starlight from the halo surrounding the star into its λ/D -sized core. However, the photon noise from the diffraction rings of a well-corrected stellar PSF also inhibit our sensitivity to faint companions near the star. To suppress the light from the diffraction rings before that light reaches the science detector, we employ a device called a coronagraph.

To explain the physics of coronagraphs, we must first return the description of Fraunhofer diffraction given by Equation 1.8. Continuing to follow Hardy (1998), we may re-express Equation 1.8 using the spatial frequencies $f_x = kX/R$ and $f_y = kY/R$ to give

$$E(f_y, f_x) = \int_{-\infty}^{+\infty} \int \mathcal{A}(y, x) e^{i(f_y y + f_x x)} dy dx, \quad (1.20)$$

where $\mathcal{A}(y, x)$ is a re-expression of the term outside of the parentheses in Equation 1.8 in terms of the amplitude variations A_0 and the phase variations $e^{i\phi(y,x)}$ at the telescope aperture:

$$\mathcal{A}(y, x) = A_0(y, x) e^{i\phi(y,x)}. \quad (1.21)$$

Equation 1.20 above demonstrates an important relationship: the electric field at the image plane is simply the Fourier transform of the electric field at the telescope aperture.

With this Fourier relationship in mind, we turn to the classic Lyot coronagraph design shown in Figure 1.10 (B. Lyot, 1939). This design consists of four “planes,” where each plane is the Fourier transform of the previous plane. The Fourier transform of the uniformly illuminated aperture is of course the Airy function. At this first focal plane, we place an opaque “occluding” mask. The Fourier transform of this masked Airy function is shown in the third plane, where the starlight is now mostly at the edges. We block out those edges using a circular ring called a Lyot stop. The Fourier transform of this plane is the final image, which contains less than a few percent of the star’s original power. An off-axis source such as a planet, however, will miss the occulting mask and will continue largely undisturbed to the final focal plane. Hence, the planet-to-star contrast ratio has been drastically increased.

In this example, we placed optical elements at a focal plane and in a plane conjugate to the telescope’s aperture. Our occulting mask and Lyot stop only affected the

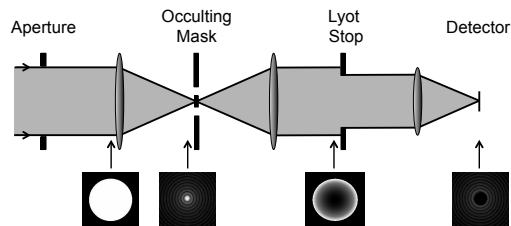


Figure 1.10: A schematic of a Lyot coronagraph optical setup. The lower part of the figure indicates the intensity patterns at the entrance pupil, first focal plane, second “Lyot” pupil plane, and second focal plane (Guyon, C. Roddier, et al. 1999, ©The Astronomical Society of the Pacific. Reproduced with permission. All rights reserved).

amplitude of the star’s electric field. Other coronagraph designs place different components at these key locations, some affecting the amplitude and others the phase of the starlight’s electric field. Figure 1.11 shows the planet-to-star contrast ratios achieved by current and planned high contrast imaging instruments, each of which includes a coronagraph. The currently available facilities shown in Figure 1.11 (the Hubble Space Telescope and the Gemini Planet Imager) do not achieve the contrasts required to image a solar system analog at 10 pc. Future space-based observatories (e.g. Wide Field Infrared Survey Telescope) as well as future large-aperture ground-based observatories (e.g. the European Extremely Large Telescope) may achieve this challenging goal (Gilmozzi and Spyromilio, 2007; Spergel et al., 2015).

To understand the limitations to these instruments’ contrast ratios, we must return to the concept of “speckles” introduced in the first part of this sub-section when discussing a short exposure image of a stellar PSF in the presence of turbulence. Unfortunately, wavefront aberrations introduced by the telescope and instrument’s optical aberrations (e.g. a ripple pattern on a mirror due to a polishing tool) also produce such speckles. Aberrations that occur after the AO system, such as imperfections on the lens that brings the science beam to a focus in Figure 1.9, are particularly problematic because they do not affect the wavefront sensor. Furthermore, a speckle’s intensity is related to the intensity of the residual post-coronagraphic stellar PSF at the speckle’s location in the focal plane, which increases the intensity of speckles falling on the peaks of the diffraction rings. While these instrument-induced speckles do evolve over time (e.g. due to thermal, gravity vector, and telescope pointing changes), their noise contribution does not scale with the square root of the exposure time, and they may persist for the duration of an

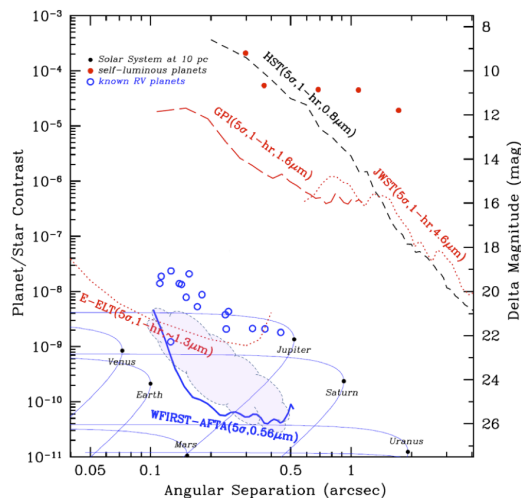


Figure 1.11: The planet-to-star contrast ratios achieved by current and future planet imaging instruments (black, red, and bold blue lines). Several young, massive planets that have already been detected in the near infrared are shown by the red dots. The open blue circles represent the visible-wavelength contrast ratios of planets that have been detected by the radial velocity method, but have not yet been directly imaged. The solar system planets at visible wavelengths are shown as black dots, with the thin blue curves representing different phase angles. This figure was adapted from Spergel et al. (2015).

observation.

Figure 1.12 shows an example of an image from an AO+coronagraph system on a real telescope. While one bright companion is visible, any fainter companions closer to the central star would be difficult to distinguish from speckles. This task – the differentiation of speckles from planets – is the subject of the next subsection.

Observing Strategies for Differential Imaging

There are several fortuitous differences between speckles and astrophysical signals that may be exploited to detect faint companions.

First, a telescope with an altitude-azimuth mount can be operated in such a way that the telescope+instrument orientation stays fixed relative to the image plane while the astrophysical scene rotates about the telescope’s optical axis. Hence, a planet will rotate about the central star over the course of an observation, but the speckles will not (although the speckles will evolve temporally and spatially due to variations in temperature, pointing, etc). If many short exposures are taken in this mode, the resulting image cube can be re-aligned based on the planet’s positions. Median-combining this re-aligned cube increases the SNR of the companion by

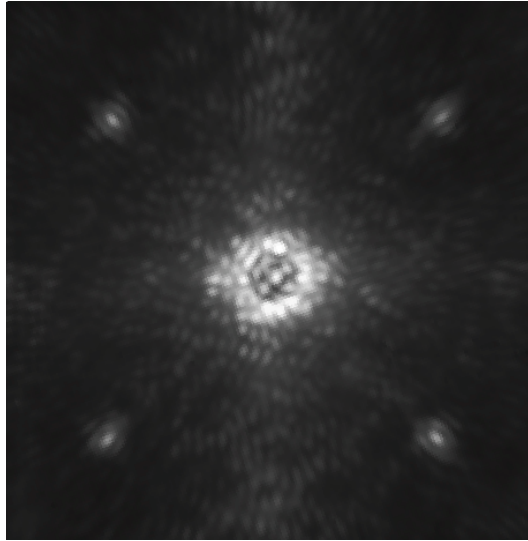


Figure 1.12: An example of a post-AO, post-coronagraphic stellar point spread function (P1640/Nilsson, private communication). Many bright “speckles” are visible around the attenuated star in the center of the image. The speckles are slightly elongated due to the wide bandpass of the image ($\lambda_0 = 1.3 \mu\text{m}$, $\Delta\lambda = 25 \text{ nm}$). The four bright speckles are intentionally created in order to provide astrometric and photometric calibration sources.

allowing the spatially-varying speckles to average down. This technique is called angular differential imaging, or ADI (C. Marois, D. Lafrenière, R. Doyon, et al., 2006). An important drawback of ADI is that regions closer to the star rotate over a smaller angular distance than regions farther away for a given exposure time. Hence, obtaining sufficient rotation for the innermost regions of the image can be prohibitively time consuming.

Another technique, which can be combined with ADI, is called spectral differential imaging, or SDI (Racine et al., 1999; Sparks and Ford, 2002; C. Marois, R. Doyon, et al., 2005; Biller et al., 2006). This technique takes advantage of the variation of the speckles’ angular separation from the central star with wavelength while the planet’s position remains fixed for all wavelengths. Many high contrast imaging systems (e.g. P1640 and GPI) are equipped with a post-coronagraph integral field unit (IFU), which allows SDI to be used routinely for exoplanet searches while also providing spectra for known exoplanets (B. A. Macintosh et al., 2008; S. Hinkley et al., 2011). The speckle subtraction provided by SDI is often limited by a combination of the contrast of a speckle’s peak intensity compared with the background and the stability of the speckles over the course of the observation.

Third, a polarized astrophysical signal such as a planet or a disk can be distinguished

from unpolarized starlight with a technique called dual-mode polarimetric image, or DPI (Kuhn, D. Potter, and Parise, 2001; M. D. Perrin, J. R. Graham, et al., 2004; B. R. Oppenheimer et al., 2008). To understand this method, we first consider a monochromatic plane wave at the arbitrary point $\mathbf{r} = 0$ in the axes x and y :

$$\vec{E} = (\hat{x}E_1 + \hat{y}E_2)e^{-i\omega t} = \vec{E}_0e^{-i\omega t}. \quad (1.22)$$

This is Rybicki and Lightman (1979) Equation 2.35. Following their discussion, the complex amplitudes in the \hat{x} and \hat{y} directions are

$$E_1 = \epsilon_1 e^{i\phi_1}, E_2 = \epsilon_2 e^{i\phi_2}. \quad (1.23)$$

The components of the electric field oscillating in the \hat{x} and \hat{y} directions are therefore the real parts of $E_1 e^{-i\omega t}$ and $E_2 e^{-i\omega t}$, respectively:

$$E_x = \epsilon_1 \cos(\phi_1 - \omega t), E_y = \epsilon_2 \cos(\phi_2 - \omega t). \quad (1.24)$$

If we were to plot (E_x, E_y) on the (x, y) plane for various values of t , we would trace out an ellipse for most values of ϵ_1 , ϵ_2 , ϕ_1 , and ϕ_2 . In such a situation, the wave is elliptically polarized. For special values of these parameters, however, (E_x, E_y) over time may trace out a circle (corresponding to circular polarization), or a straight line (corresponding to linear polarization). We can describe the polarization using the Stokes vectors:

$$\begin{aligned} I &\equiv \epsilon_1^2 + \epsilon_2^2, \\ Q &\equiv \epsilon_1^2 - \epsilon_2^2, \\ U &\equiv 2\epsilon_1^2 \epsilon_2^2 \cos(\phi_1 - \phi_2), \\ V &\equiv 2\epsilon_1^2 \epsilon_2^2 \sin(\phi_1 - \phi_2). \end{aligned} \quad (1.25)$$

We note that under real observing conditions, these quantities are time-averages. If the electric field of the planet is linearly polarized along the \hat{x} direction, we can choose $\epsilon_1 = 1$ and $\epsilon_2 = 0$. Hence, Stokes Q is equal to one while Stokes U and V are zero. If the star's electric field has no preferred plane of oscillation, the starlight's Stokes Q and U will average to zero.

A straightforward way to distinguish polarized planets or disks from unpolarized starlight is to insert a Wollaston polarizer between the coronagraph and the final image plane. This device is made of birefringent material – i.e. a material whose index of refraction differs for the two orthogonal linearly polarized components of an incoming beam. The Wollaston polarizer spatially separates the perpendicular polarization vectors to form two images. Unpolarized starlight will contribute equally

to these two images, while a polarized source will not. Hence, by subtracting the two perpendicularly polarized images, the star's PSF and speckles will be removed while a polarized source will remain. We will return to the topic of polarized emission from exoplanets in Chapter 3.

While DPI allows for precise subtraction of the stellar PSF and associated speckles, it is only useful when the planet or disk is itself polarized. Young, massive, widely separated planets are not universally highly polarized in the near-IR, and so ADI and SDI remain more popular as general purpose planet-hunting strategies.

Finally, an observation of a reference star with no astrophysical companion can be subtracted from the science star of interest to remove the stellar PSF (D. Lafrenière, C. Marois, René Doyon, et al., 2009). The difficulty with this reference star differential imaging (RDI) method is that the speckle pattern will inevitably evolve between the observations of the target and reference stars. However, RDI is a particularly promising method for subtracting the speckles closest to the star, where ADI exposure times are long. Given a very large library of reference star observations, a synthetic reference star can be constructed that resembles the science PSF more than any one reference observation. This post-processing concept is discussed in the following section.

Image Post-Processing Techniques

Each of the above observing strategies provides imperfect speckle subtraction. Here, we will describe two post-processing methods that have been developed to remove residual speckles and bring the noise statistics of the image to the photon noise limit.

C. Marois, D. Lafrenière, R. Doyon, et al. (2006) and D. Lafrenière, C. Marois, René Doyon, et al. (2007) first developed the locally optimized combination of images (LOCI) technique for speckle calibration. LOCI works by dividing the science image into sections and for each section finding the linear combination of reference image sections that, when subtracted, gives the least residual noise. The reference images can be obtained from any of the methods described in the previous section (for the example of ADI, the de-rotated frames in which the companion is sufficiently displaced can serve as the reference frames). The principle drawbacks of the LOCI algorithm are its speed and the biases that it introduces to the companion's photometry and astrometry.

R. Soummer, L. Pueyo, and Larkin (2012) proposed the Karhunen–Loève image projection (KLIP) algorithm to mitigate the problems with LOCI mentioned above.

Like LOCI, KLIP creates a linear combination of reference images originating from ADI, RDI, SDI, etc, but it processes the library of images differently: KLIP takes the Karhunen–Loève transform of the reference library, the output of which is the optimal set of orthogonal reference images. The science image is projected onto the first K_{klip} references to generate the synthetic PSF to be subtracted. The choice of K_{klip} depends on the exact observing objective, but is generally chosen to optimize the planet-to-star contrast ratio or planet SNR. KLIP can be performed on the full image or on difference pieces of the image separately.

*Chapter 2*ATTAINING DOPPLER PRECISION OF 10 CM S^{-1} WITH A
LOCK-IN AMPLIFIED SPECTROMETER

ABSTRACT

We explore the radial velocity performance benefits of coupling starlight to a fast-scanning interferometer and a fast-readout spectrometer with zero readout noise. By rapidly scanning an interferometer we can decouple wavelength calibration errors from precise radial velocity measurements, exploiting the advantages of lock-in amplification. In a Bayesian framework, we investigate the correlation between wavelength calibration errors and resulting radial velocity errors. We construct an end-to-end simulation of this approach to address the feasibility of achieving 10 cm s^{-1} radial velocity precision on a typical Sun-like star using existing, 5-meter-class telescopes. We find that such a precision can be reached in a single night, opening up possibilities for ground-based detections of Earth-Sun analog systems.

2.1 Introduction

Recent results from NASA's *Kepler* mission indicate that Sun-like stars are teeming with rocky exoplanets (D. G. Koch et al., 2010; Borucki, D. G. Koch, et al., 2011; A. W. Howard, G. W. Marcy, et al., 2012; Batalha et al., 2013; Petigura, A. W. Howard, and G. W. Marcy, 2013). According to statistics derived from *Kepler*'s discoveries, and consistent with prior exoplanet searches, ground-based radial velocity and transit surveys targeting nearby stars are approaching the performance edge of discovering hundreds of exoplanets suitable for detailed atmospheric studies (e.g. Deming, S. Seager, Winn, et al., 2009; A. W. Howard et al., 2010; Dressing and D. Charbonneau, 2013; Berta, Irwin, and D. Charbonneau, 2013). NASA's future Transiting Exoplanet Survey Satellite (TESS) will likely find those rocky planets that transit nearby stars in short-period orbits (Ricker, 2014). TESS will determine the radii of exoplanets transiting nearby stars. With precise radial velocity measurements of the TESS discoveries, the exoplanet masses, mean densities and surface gravities can be determined, thereby constraining their interior structures and atmospheric characteristics.

The future of exoplanet science is therefore promising; however, the precision needed to detect nearby rocky planets with radial velocities (RVs), and measure the masses of those found to transit with TESS, is daunting. For example, the Earth introduces an 8.9 cm s^{-1} semi-amplitude Doppler reflex motion on the Sun. To date, the smallest semi-amplitude radial velocity measured on a star is 51 cm s^{-1} on α Centauri Bb, indicating the presence of an exoplanet with a minimum mass of $1.13 M_{\oplus}$, and a semi-major axis of 0.04 AU (X. Dumusque et al., 2012). The planet's discovery has yet to be confirmed by independent instruments or techniques, so α Centauri Bb is widely regarded as an exoplanet candidate. Nevertheless, the measurement indicates the state-of-the-art in stellar radial velocity precision. The detection of α Centauri Bb requires both astrophysical and instrumental noise corrections. Known astrophysical noise sources such as stellar oscillation modes, granulation, and activity signals can be individually removed through careful choices of exposure times and observing cadence, as well as modeling each effect separately (X. Dumusque et al., 2011). Pepe et al. (2011) describe how instrumental noise sources in HARPS, such as changes to temperature, pressure, and illumination, are addressed through high cadence, long time baseline observations of nearby, slowly rotating stars with little known activity. To this end, HARPS observed HD 85512 for 7.5 years, obtaining 185 RV data points and discovering a $3.5 M_{\oplus}$ planet. The standard deviation of the data residuals after subtracting the model of the planet

was measured to be 0.75 m s^{-1} . While this value could encompass uncharacterized astrophysical noises, 0.75 m s^{-1} is taken to be representative of the instrumental noise in HARPS. In order to reduce the state-of-the-art RV semi-amplitude from 51 cm s^{-1} (α Centauri Bb) to 8.9 cm s^{-1} (Earth-Sun analog), these instrumental noise sources must be understood and eliminated.

Eliminating the effects of instrumental noise on radial velocity measurements requires ever more precise wavelength calibration techniques. Historically, iodine absorption cells and thorium-argon (ThAr) lamps have been the principal wavelength calibration tools. Starlight passing through an iodine gas cell results in a dense series of iodine absorption lines superimposed onto the stellar spectrum. This method has been implemented on HIRES, where planet semi-amplitudes as small as 1.89 m s^{-1} have been detected (HD 156668b, A. W. Howard, J. A. Johnson, et al., 2011). The small number of absorption lines at red and near-IR wavelengths, however, limits the use of iodine cell calibration for redder stars. Furthermore, the technique requires complex modeling of the combined iodine/stellar spectrum, which in turn requires high signal-to-noise data (Lovis and Pepe, 2007). As an alternative to the iodine cell approach, fiber-fed spectrographs have used ThAr lamps as a simultaneous wavelength reference (Baranne et al., 1996). Starlight and ThAr lamp light are fed into the spectrograph through separate fibers such that their spectra are simultaneously recorded onto the detector. While ThAr provides more lines in the near-IR than iodine, the non-uniformity in line spacing and long-term variability of ThAr sources limits the technique.

Recently, laser frequency combs (LFCs) have provided large numbers of equally spaced, stable lines over a wide range of wavelengths (e.g. Murphy et al., 2007; Steinmetz et al., 2008). LFCs fix the phase of standing waves inside a laser cavity such that the waves periodically interfere constructively, producing bursts of light. The time between bursts can be accurately controlled using an atomic clock. In the frequency domain, the laser therefore produces a series of equally spaced spectral lines.

An experimental LFC installed on HARPS in 2010 has yielded unprecedented RV stability over short timescales (Wilken et al., 2012). The HARPS spectrograph is fed by two multimode fibers, or channels; one channel is coupled to starlight, and the other to light from the LFC. In Wilken et al., 2012, the HARPS team fed LFC light through both fibers, and differenced the two channels to measure the instrumental drift. By optimally binning 20-30s exposures for 4 minutes, the

limiting RV precision due to instabilities between the two channels was found to be 2.5 cm s^{-1} . Between November of 2010 and January of 2011, however, synchronous drift in the channels induced a standard deviation of 34 cm s^{-1} between data taken in the two time periods. While planned changes to the environmental conditions surrounding HARPS made this 34 cm s^{-1} drift measurement a slight underestimate of the long term stability, the two channels nevertheless experienced long term drifts larger than the 2.5 cm s^{-1} short term limiting RV precision. These drifts are thought to be due to uncontrolled, long timescale instrumental changes.

An innovative approach to acquiring Doppler measurements of stars was proposed by Erskine (2003). By introducing a Michelson or Mach-Zender interferometer into the optical path before a traditional spectrometer, Erskine (2003) suggested high Doppler precision could be achieved with instrumental fluctuations minimized. The technique, called externally dispersed interferometry (EDI), requires that the optical path difference in the interferometer be modulated, either spatially or temporally. He suggested both a spatial modulation, by tilting one of the interferometer cavity mirrors, and a temporal modulation, by physically moving one of the cavity mirrors. The phases of the resulting fringe patterns, whether temporal or spatial, are highly sensitive to changes in the Doppler velocity of the target star. As noted by Erskine (2003), the modulation of a spectrum into a fringe pattern provides a robust way of eliminating systematic effects, such as fixed-pattern noise, in the resulting radial velocity measurements.

Since then, multiple groups have implemented EDI systems. Ge et al. (2006) and S. Mahadevan et al. (2008) describe an instrument called the Exoplanet Tracker (ET) which uses a tilted cavity mirror without temporal modulation. Van Eyken, Ge, and S. Mahadevan (2010) describe the theory and implementation of ET and a similar instrument called the Multi-object APO Radial Velocity Exoplanet Large-area Survey (MARVELS). Hajian et al. (2007) describe the dispersed Fourier Transform Spectrometer (dFTS), designed to acquire high-resolution spectra rather than measure precise radial velocities, also achieved by Erskine et al. (2003). And finally, Muirhead et al. (2011) describe the TripleSpec Exoplanet Discovery Instrument (TEDI), which used temporal rather than spatial modulation to map out the fringes.

A particularly interesting result from Muirhead et al. (2011) was the achievement of 30 m s^{-1} of RMS radial velocity performance without any calibration of the spectrometer point-spread function. Typically, precise radial velocity spectrometers involve a significant amount of effort to stabilize the spectrometer PSF because un-

calibrated asymmetries in the PSF are degenerate with wavelength calibration errors, and result in spurious radial velocity measurements on the target star. Muirhead et al. (2011) show that the reduced importance of wavelength calibration is a direct result of the radial velocity measurement being encoded in the phase of a sinusoid varying within each pixel, rather than the change in flux across several pixels, as is the case for traditional spectroscopy as well as for ET and MARVELS, which use spatial modulation across pixels rather than temporal modulation within a pixel.

However, a significant challenge to temporal modulation techniques involves effects from readout noise. The robustness against errors in wavelength calibration is due to modulation taking place on short timescales, and the PSF fluctuations taking place over longer timescales. PSF fluctuations or wavelength calibration errors that occur over the same timescale as the modulation are not removed. Fast scanning is therefore desired. Readout noise in large format detectors limits the speed at which one can scan and read out the detector in the spectrometer. In Muirhead et al. (2011), the authors took 30 second exposures to ensure that the dominant noise source was photon noise, rather than detector readout noise.

Recent developments in large format, high frame rate and low-readout noise detectors motivate studies of temporal modulation at very high frame rates. Electron multiplying charge-coupled devices (EMCCDs) and complementary metal-oxide-semiconductor (CMOS) detectors can be manufactured and operated to have inherently low readout noise (< 1 electron per pixel) and the ability to expose and read out at very high frame rates (100 megapixels per second). With a high enough gain enabled, EMCCDs have effectively zero readout noise. These detectors are becoming commonplace in astronomical instruments (e.g. Dhillon and Marsh, 2001; C. Baranec et al., 2013), motivating a study of the advantages of fast-modulation EDI for ultra-precise Doppler velocimetry.

In this chapter, we show that the act of modulating a spectrum in time effectively decouples wavelength calibration errors from radial velocity measurements. Therefore, the nature of the radial velocity measurement is fundamentally different from that obtained from conventional spectroscopy, where wavelength calibration completely determines the resulting radial velocity measurement. Instead, the radial velocity precision relies upon precise knowledge of the interferometer positions¹. We augment previous theoretical studies of the EDI technique (e.g. Erskine, 2003;

¹A possible implementation could involve a combination of fine pathlength control with precision PZTs and fine sensing using a co-propagating laser with exceptional wavelength stability.

van Eyken, Ge, and S. Mahadevan, 2010) by specifically introducing and recovering wavelength calibration errors into simulated data. We also investigate the effects of interferometer position errors on radial velocity precision. Finally, we simulate the performance of a time-varying interferometric system on a medium-sized telescope to determine the feasibility of an Earth-Sun analog detection.

2.2 Theory

Following the discussion in Erskine (2003) and also Muirhead et al. (2011), we derive the relationship between a temporally modulated spectrum and a radial velocity measurement. We use this relationship to demonstrate the decoupling of wavelength calibration errors and RV measurements.

The intensity of the stellar spectrum recorded by the detector depends on both the wavelength and the interferometer delay. The interferometer delay is assumed to vary sinusoidally with time, therefore acting as a sinusoidal transmission comb. For a wave number ν , and delay τ , the measured intensity is given by

$$I_{\nu,\tau} = [S_\nu(1 + \cos(2\pi\tau\nu))] * R_\nu, \quad (2.1)$$

where S_ν is the intrinsic stellar spectrum, $(1 + \cos(2\pi\tau\nu))$ represents the transmission comb, R_ν is the spectrograph line spread function, and $*$ represents the convolution. While most practical interferometer configurations will result in two output beams, we assume here that the beams have been combined (for example, by placing a spectrograph and detector at each output and combining the intensities in post-processing).

The interferometer delay τ can be expressed as the sum of a constant bulk delay, τ_0 , and a smaller time-varying phase shift $\Delta\tau$. Taking $\tau = \tau_0 + \Delta\tau$, and applying trigonometric identities, the measured intensity can be re-written as:

$$I_{\nu,\tau_0,\Delta\tau} = A_\nu + B_\nu \cos(2\pi\Delta\tau\nu) - C_\nu \sin(2\pi\Delta\tau\nu). \quad (2.2)$$

The coefficients A_ν , B_ν , and C_ν are defined as

$$A_\nu = S_\nu * R_\nu, \quad (2.3)$$

$$B_\nu = [S_\nu \cos(2\pi\tau_0\nu)] * R_\nu, \quad (2.4)$$

$$C_\nu = [S_\nu \sin(2\pi\tau_0\nu)] * R_\nu, \quad (2.5)$$

where A_ν is the non-modulated spectrum, while B_ν and C_ν describe the interference between the stellar spectrum and the transmission comb. These coefficients can

be determined by varying the interferometer delay $\Delta\tau$, and observing the intensity $I_{\nu, \tau_0, \Delta\tau}$. A data set, or “scan” is a list of intensities at a range of $\Delta\tau$ and ν values.

In order to compare the fitted coefficients between two scans, B_ν and C_ν are combined into a “complex visibility:”

$$B_\nu - iC_\nu = [S_\nu e^{-i2\pi\tau_0\nu}] * R_\nu. \quad (2.6)$$

The complex visibility is used to compare two scans, where one has been Doppler shifted by $\Delta\nu = (\Delta RV/c)\nu$. $\Delta\nu$ and $1/\tau_0$ are assumed to be small compared to a resolution element of the spectrograph. By applying the Fourier convolution and shift theorems, the Doppler shifted “epoch” complex visibility $B_\nu^1 - iC_\nu^1$ and the unshifted “template” visibility $B_\nu^0 - iC_\nu^0$ are related by an exponential phase:

$$\begin{aligned} B_\nu^1 - iC_\nu^1 &= [B_\nu^0 - iC_\nu^0] e^{-i2\pi\tau_0\Delta\nu} \\ &= [B_\nu^0 - iC_\nu^0] e^{-i2\pi\tau_0(\Delta RV)\nu/c}. \end{aligned} \quad (2.7)$$

For clarity, the discussion above applies to small radial velocity shifts only, due to the use of the Fourier shift theorem. On-sky observations, however, will be affected by the Earth’s motion relative to the barycenter of the solar system, producing RV shifts on the order of 10 km s^{-1} . Muirhead et al. (2011) describe the detailed derivation of the relationship between the epoch and template complex visibilities, arriving at the following generalization of Equation 2.7:

$$B_\nu^1 - iC_\nu^1 = e^{i2\pi\tau_0\Delta\nu} [(B_\nu^0 - iC_\nu^0) e^{-i2\pi\tau_0\Delta\nu}]_{\nu \rightarrow \nu + \Delta\nu}. \quad (2.8)$$

Therefore, a Doppler shift changes the phase of the complex visibility (for example, an Earth-Sun analog would result in a phase shift of 3.4×10^{-5} radians). A wavelength calibration error re-assigns the phase values to a different wavelength grid without changing the value of the phase itself. The radial velocity measurements are therefore decoupled from wavelength calibration changes; instead, the RV precision relies upon precise knowledge of the interferometer positions, described by $\Delta\tau$ and τ_0 . Section 2.4 describes the effects of wavelength calibration and interferometer position errors in detail.

2.3 Simulation Architecture

In order to quantify instrumental contributions to radial velocity precision, we construct an end-to-end simulation of the radial velocity reconstruction process

described in Section 2.2. The flux entering the instrument is modeled using a simulated solar spectrum (Coelho et al., 2007). We multiply the stellar spectrum by the interferometer comb, which is modeled as a sinusoidal transmission comb as a function of wavenumber ν and interferometer delay τ (see Equation 2.1). The result is therefore a series of spectra multiplied by transmission combs of different interferometer delays.

The product of the stellar spectrum and interferometer transmission comb is convolved with the spectrograph instrument profile (IP). The spectrograph IP is modeled as a normal distribution with a width corresponding to a spectrograph resolution of $R=10000$. The resolution was chosen to be low in order to avoid resolving the interferometer comb; in order for the phase of the interference fringes to correspond to a radial velocity change, the comb must remain unresolved. The sampling is assumed to be 4 pixels per resolution element. The result is a stellar spectrum recorded at each interferometer step (Figure 2.1). The final data product can be represented by a three dimensional map of interferometer delay, wavelength, and observed intensity (Figure 2.2).

It is clear from the axes of Figure 2.2 that wavelength calibration and radial velocity information are separated; the y-axis represents time (the time-varying position of the interferometer), while the x-axis represents detector pixels (the wavelength information introduced by the spectrograph). A radial velocity shift will therefore result in a vertical shift as the phase of the interference fringes changes, whereas a change in wavelength calibration will result in a global horizontal shift as the spectrum's wavelength is re-assigned.

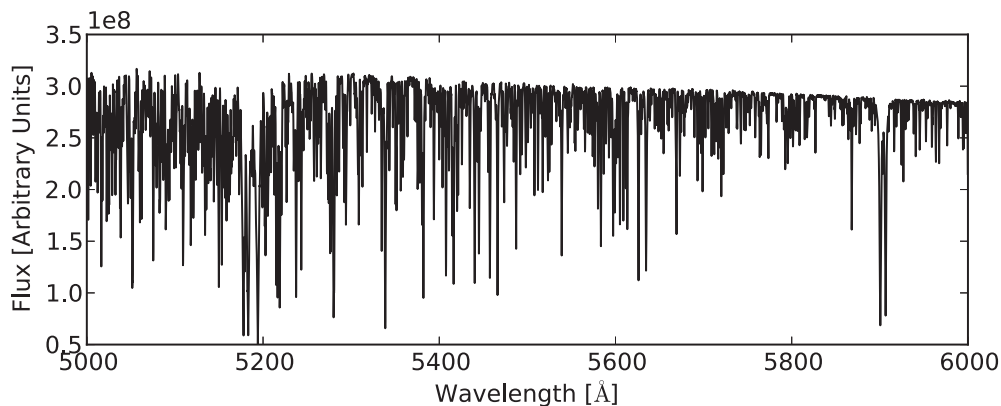


Figure 2.1: A horizontal cut through Figure 2.2 reveals the simulated stellar spectrum. Note that for ease of viewing, Figure 2.2 shows the mean subtracted fringes.

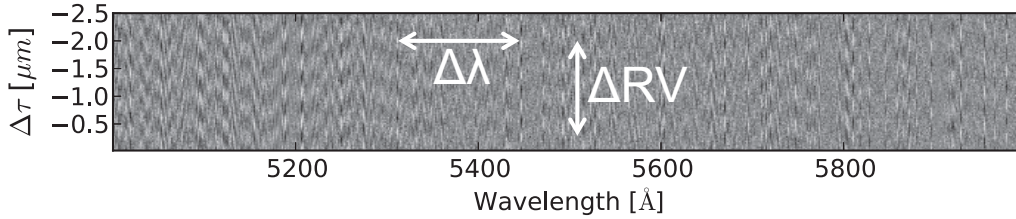


Figure 2.2: A simulated mean subtracted spectrum vs. wavelength and $\Delta\tau$ for $\text{SNR} = 500$. The x-axis corresponds to wavelength, or pixels on the spectrometer detector. The y-axis corresponds to changes in the optical path difference of the interferometer, and therefore represents time as the interferometer optical path difference is modulated temporally. The regions of high fringe contrast correspond to absorption lines in the stellar spectrum. An error in the wavelength calibration is fundamentally different from a change in the radial velocity of the target star, as long as the wavelength calibration error does not occur during an interferometer scan.

Each vertical cut through Figure 2.2 represents the intensity as a function of phase delay at a given wavenumber described by Equation 2.2. Noise is added to the intensity at each phase delay by adding values drawn from a Gaussian distribution with a mean of zero and a standard deviation given by the spectrum's mean divided by the desired signal-to-noise ratio. For clarity, we refer to this as Poisson noise, but our simplifications (Gaussian statistics with a constant standard deviation) should be noted. The A_ν , B_ν , and C_ν coefficients are then fit to each vertical cut, defining the complex visibilities (Equation 2.6).

In order to measure a radial velocity shift, two data sets, each represented by a figure like Figure 2.2, are produced: a template spectrum and an epoch spectrum with an RV shift and wavelength calibration error. The template spectrum is assumed to have infinite signal-to-noise, due to either a long on-sky integration or the use of a simulated spectrum. The template spectrum is multiplied by a complex phasor as in Equation 2.8, containing a test RV shift, and is interpolated onto a new wavelength grid to represent the effect of the wavelength calibration error. This modified template spectrum and the originally shifted epoch spectrum are then compared using a chi-squared test that treats the real and imaginary parts of the complex visibilities separately:

$$\frac{-\chi^2}{2} = \sum_{\nu} \left(B_{\nu}^s - B_{\nu}^1 \right)^2 + \left(C_{\nu}^s - C_{\nu}^1 \right)^2, \quad (2.9)$$

where B_{ν}^1 and C_{ν}^1 describe the epoch spectrum, and B_{ν}^s and C_{ν}^s describe the modified

Table 2.1: Simulation Parameters

Parameter	Value	Units	Description
Spectrograph resolution	10,000		This is chosen to be small to avoid resolving the interferometer comb
Pixels per res. elem.	4.0	pixels	Slightly exceeds Nyquist sampling
Bandpass	507-595	nm	V-band FWHM
Stellar model	Coelho	N/A	G star spectrum from Coelho et al 2007
Scan step size	0.012	μm	20 \times (Nyquist sampling)
Scan stroke	2.5	μm	5 fringe cycles
Bulk Delay	2.0	cm	

template spectrum. Because the likelihood function is defined as

$$L = e^{-\frac{\chi^2}{2}}, \quad (2.10)$$

Equation 2.9 is considered to be $\log(L)$. We compute $\log(L)$ on a grid of radial velocity and wavelength calibration error test points, and find the points that minimize Equation 2.9 by parabola fitting. By computing many such solutions for independent realizations of the noise, we construct histograms of radial velocity and wavelength calibration errors solutions that are well described by Gaussian statistics. We define the standard deviation of 100 radial velocity solutions to be the ‘‘radial velocity precision.’’ By fitting a 2D Gaussian distribution to a 2D histogram of several thousand radial velocity and wavelength calibration error solutions, we compute error ellipses demonstrating the relationship between the two parameters (Figure 2.3). In contrast to traditional RV reconstruction methods, the contours show an elliptical shape, demonstrating that the RV and wavelength calibration error measurements are not highly correlated.

2.4 Error Budget

The simulation described in Section 2.3 is used to analyze the effects of Poisson noise, wavelength calibration errors, and interferometer position errors. The assumptions used in the simulation are listed in Table 2.1. We also note that all radial velocity and wavelength calibration error solutions discussed in this section were generated using a spectral bandwidth of $\Delta\lambda = 88\text{\AA}$, while the FWHM of the

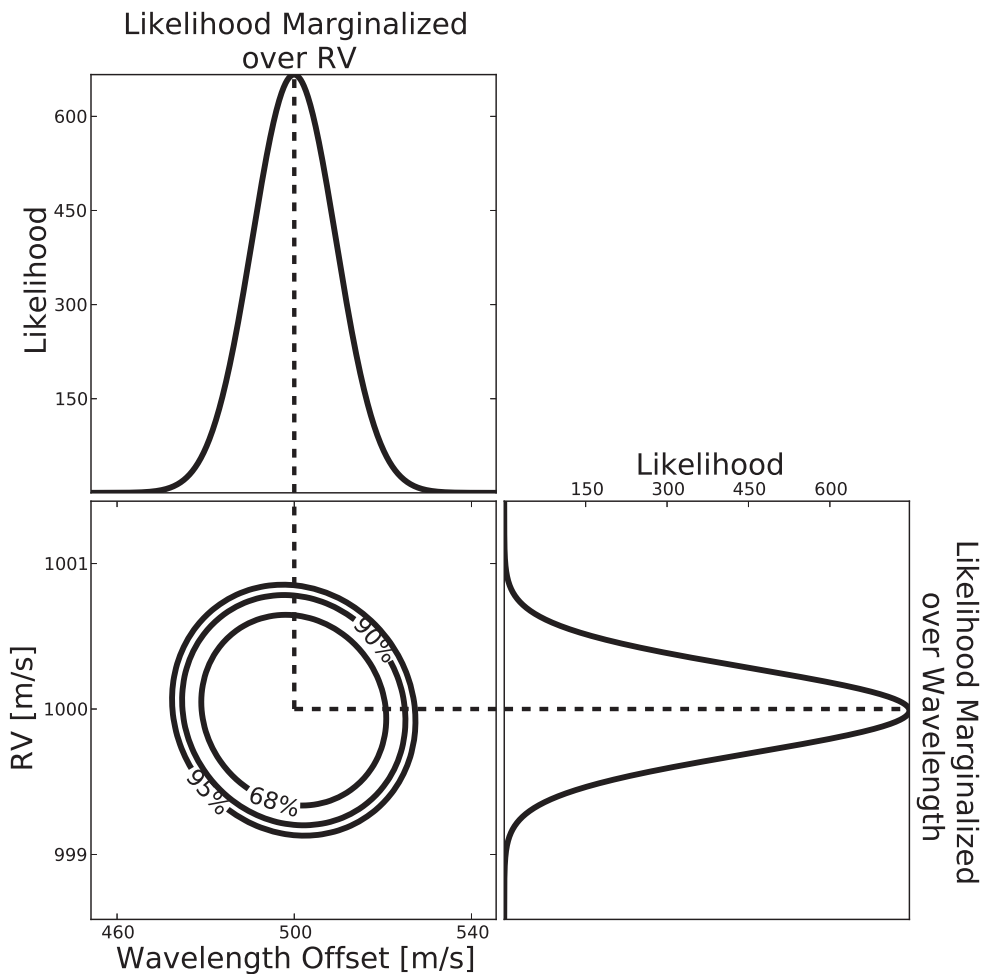


Figure 2.3: Simulated likelihood contours describing the radial velocity and wavelength calibration error reconstructions for injected values of 1000 m s^{-1} and 500 m s^{-1} respectively, for $\text{SNR}=100$ and a spectral bandwidth of $\Delta\lambda = 88\text{\AA}$. In contrast to traditional RV reconstruction methods, the contours show an elliptical shape, demonstrating that the RV and wavelength calibration error measurements are not highly correlated.

V -band filter is $\Delta\lambda = 880\text{\AA}$. We chose this smaller bandwidth to accommodate the available computing resources. Because the number of spectral lines increases with the square root of the bandwidth, however, we can represent the $\Delta\lambda = 880\text{\AA}$ radial velocity precision by dividing the $\Delta\lambda = 88\text{\AA}$ radial velocity precision by $\sqrt{10}$. The text and figures below refer to radial velocity precisions that have been modified by this factor.

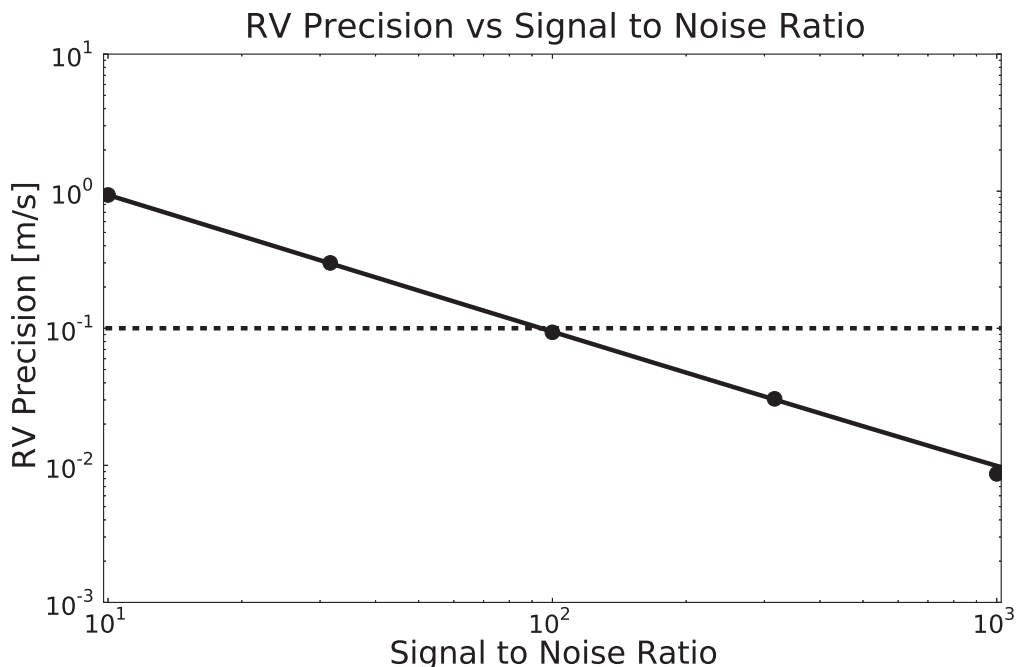


Figure 2.4: Radial velocity precision is plotted against the signal-to-noise ratio for Poisson noise limited measurements, (no instrumental or astrophysical noise sources). Under these conditions, an SNR of about 94 per phase step, for 200 phase steps, is required to reach a precision of 10 cm s^{-1} . The RV precisions shown in this plot were calculated using a spectral bandwidth of $\Delta\lambda = 88\text{\AA}$, and were divided by $\sqrt{10}$ to reflect the RV precisions associated with the full V -band bandwidth of 880\AA .

Poisson Noise

In the absence of all instrumental or astrophysical noise sources, the radial velocity precision decreases as $1/\text{SNR}$ (Figure 2.4). Under these conditions, a signal to noise ratio of about 94 per spectrograph resolution element is required to reach a radial velocity precision of 10 cm s^{-1} . Sections 2.4-2.4 below describe how instrumental noise sources cause the RV precision to deviate from this ideal case.

Wavelength Calibration Errors

Figure 2.5 shows that the radial velocity precision changes by mm/s per km/s of wavelength calibration error for high signal-to-noise ratios. The black line in Figure 2.5 represents the 1:1 correspondence between wavelength calibration and radial velocity using conventional RV reconstruction methods. We have therefore demonstrated that by temporally varying a stellar spectrum, the dependence of the

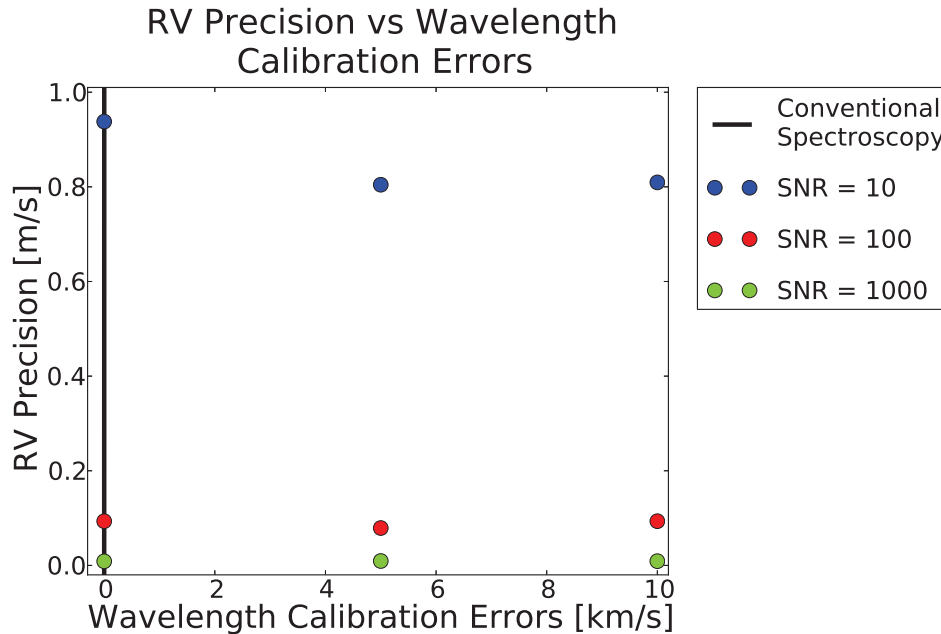


Figure 2.5: The radial velocity precision is shown to be approximately constant over 10 km s^{-1} ($\sim 0.2 \text{ \AA}$) wavelength calibration errors for SNR = 10, 100, and 1000. In contrast, the radial velocity precision is proportional to the wavelength calibration error in conventional spectroscopy. The RV precisions shown in this plot were calculated using a spectral bandwidth of $\Delta\lambda = 88 \text{ \AA}$, and were divided by $\sqrt{10}$ to reflect the RV precisions associated with the full V-band bandwidth of 880 \AA .

radial velocity precision on a consistent, correct wavelength solution is reduced.

Interferometer Position Errors

This robustness against wavelength calibration errors comes at the cost of precise knowledge of the interferometer position. The interferometer position is described by a constant “bulk” offset and a much smaller time varying phase shift (τ_0 and $\Delta\tau$, respectively, in Equation 2.2).

Equation 2.8 shows that errors in estimation of the bulk delay produce proportional errors in the RV precision. Therefore, the same error in a bulk delay measurement will result in poorer RV precision for stars with larger radial velocities. In order to calculate the smallest required bulk delay measurement error, we must consider the target stars with the largest radial velocities. Barycentric motion produces radial velocity differences of up to 60 km s^{-1} . In order to reach an RV precision of 10 cm s^{-1} with a typical bulk delay of 2 cm , the maximum bulk delay measurement error is $\left(\frac{10 \text{ cm}}{60 \text{ km}}\right) 2 \text{ cm} = 33 \text{ nm}$. State-of-the-art piezo electric stages are capable of sub-nm RMS measurement accuracy (e.g. Samuele et al. (2007)), so we conclude that the

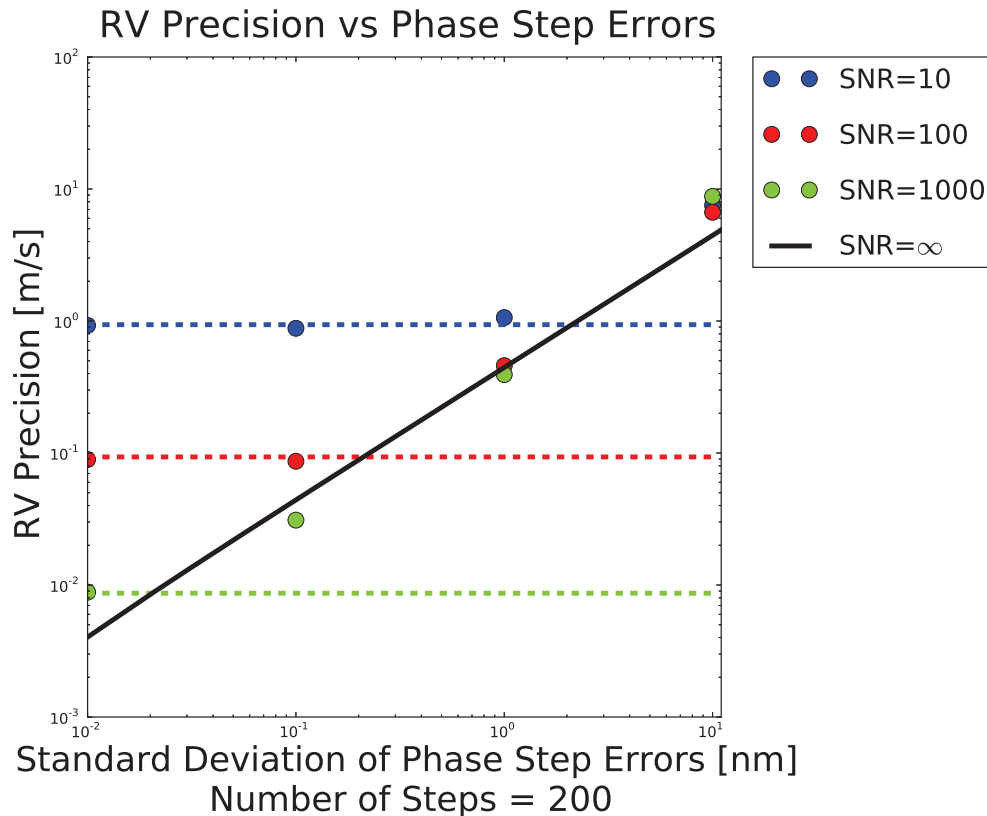


Figure 2.6: The RV precision is plotted against the standard deviation of the phase step error. The horizontal dotted lines represent the Poisson limited RV precision for each SNR. In the phase step error limited regions, the RV precisions approach the limiting $SNR = \infty$ condition, shown by the black line. For $SNR = 100$, $\Delta\tau$ must be measured to less than 1 nm to reach the Poisson limited regime. Because the phase step errors are assumed to be uncorrelated, the total number of phase steps affects the final RV precision. In this simulation, we chose 200 steps (Table 2.1). The RV precisions shown in this plot were calculated using a spectral bandwidth of $\Delta\lambda = 88\text{\AA}$, and were divided by $\sqrt{10}$ to reflect the RV precisions associated with the full V-band bandwidth of 880\AA .

bulk delay can be adequately measured to provide 10 cm s^{-1} precision on the stars with the largest radial velocities.

Errors in the phase step estimations, however, impose more strict metrology requirements. Figure 2.6 shows the radial velocity precision as a function of phase step error. Normally distributed errors with standard deviations represented by the values on the x-axis were added to the true phase delays. The horizontal regions of the $SNR = 10$, 100 , and 1000 plots show the Poisson limited regime, while the sloped regions represent the phase step error limited regime. The black line represents SNR

$= \infty$. For a single SNR = 100 scan, the phase steps must be known to sub-nanometer precision to remain in the Poisson limited regime. Because the phase step position errors are expected to be normally distributed, however, taking multiple scans will improve the RV precision by the square root of the number of scans. In this way, the SNR of the combined scan is increased while the errors due to interferometer position errors are reduced. Section 2.5 describes this approach in detail.

2.5 The Feasibility of an Earth-Sun Analog Measurement

We have shown that the modulation of a stellar spectrum in time decouples wavelength calibration errors from RV measurements, while coupling interferometer position errors to RV measurements. Given these new constraints, we now address the feasibility of reaching a radial velocity precision of 8.9 cm s^{-1} on a G-type star using an exiting telescope. Our assumed bandpass, throughput, interferometer control requirement, and target star magnitude are summarized in Table 2.2 and described in detail below.

Operating in the visible ($\approx 500 - 600 \text{ nm}$) while observing Sun-like stars has the dual advantage of covering the peak of the G star blackbody function while reducing contamination due to telluric lines compared to the infrared. A visible bandpass, however, may come at the cost of throughput. In order to minimize the effects

Table 2.2: Instrument-Specific Parameters

Parameter	Value	Units	Comments
Bandpass	507- 595	nm	V-band FWHM
Sky to detector throughput	7.4	%	Representative of a single mode fiber coupled to a 30% Strehl input beam and a spectrograph with 30% efficiency
Interferometer position control requirement	1	nm	Conservative requirement based on 0.4nm state-of-the-art piezoelectric parameters
Stellar visual magnitude	8.5	m_v	Representative of the mode of the visual magnitudes of the 100 brightest G stars
Minimum SNR per resolution element	8		Based on minimum SNR to avoid the read noise limited regime

of interferometer position errors, calibration and starlight should share a common path in the interferometer and spectrograph. One possible approach would be to feed the instrument with a single mode fiber, containing both starlight and light from a calibration source (for example, a frequency stabilized laser). In this way, modulation of the calibration light, imprinted on the science data itself, will measure the changes in the optical path difference of the interferometer.

The single-mode fiber coupling efficiency is determined primarily by the Strehl ratio of the associated adaptive optics system. Single-mode fibers are inherently diffraction limited, and require diffraction-limited beams delivered from a telescope in order to have any consequential coupling: seeing-limited telescopes will not couple nearly enough starlight for a Doppler survey of nearby stars (Shaklan and F. Roddier, 1988). Recently, however, advanced adaptive optics systems have reported significant Strehl ratios at visible wavelengths. For example, the Robo-AO system on the Palomar 60-inch telescope has achieved a Strehl ratio of 18% in i-band (C. Baranec et al., 2012). The PALM-3000 adaptive optics system on the Palomar 200-inch telescope is designed to achieve high Strehl ratios at visible wavelengths. PALM-3000 is predicted to achieve 30% Strehl in V-band, equivalent to a 95 nm RMS wavefront error (Dekany et al., 2013). Researchers at the University of Arizona recently commissioned a visible-light adaptive optics system (VisAO) on the 6.5-m Magellan Clay Telescope, demonstrating a 43% Strehl ratio, or 149 nm RMS wavefront error, in Y-band (Close et al., 2013). For the purposes of this study, we estimate the total sky-to-detector throughput to be 7.4% by multiplying the ideal fiber coupling efficiency of 82% by a Strehl ratio of 30%, based on the performance of PALM-3000 at visible wavelengths, and a spectrograph efficiency of 30%.

As described in Section 2.2, instrumental noise varying more slowly than the interferometer's phase steps is rejected. For maximum noise rejection, the interferometer should therefore scan as quickly as possible. The interferometer's speed is then limited by detector frame rates and read noise. The lowest noise detectors at optical wavelengths, CCDs, have significant readout times of seconds to minutes. This limits the rate at which we can modulate an optical signal to the point that lock-in amplification is effectively pointless with most CCD detectors. However, the development of high-frame rate, low read noise EMCCDs and sCMOS detectors opens up the possibility of using lock-in amplification at optical wavelengths. Assuming a detector read noise of $2e^-$ per pixel, gain = 1, and four pixels per resolution element, the detector must measure 64 photons per resolution element (SNR=8) to remain

well within the photon noise limited regime. The exposure time necessary to reach this minimum SNR will place an upper limit on the scanning speed.

Taking a series of scans can reduce normally distributed noise due to interferometer position errors. The number of scans is chosen such that the desired RV precision is achieved under realistic position error conditions. State-of-the-art piezoelectric stages can be controlled to less than 1 nm RMS (e.g. Samuele et al. (2007) controlled the Physik Instrumente P-752 flexure stage to 0.4 nm rms), so we choose a 1 nm control requirement. In order to reach 10 cm s^{-1} with phase step errors of 1 nm RMS and bulk delay errors of 10% τ_0 , we require 139 scans, each with SNR = 8.

We now choose a target star magnitude and telescope size to determine the observing time required to take 139 such scans. To choose a representative target star magnitude, we constructed a histogram of the 100 brightest G stars. We choose $m_v = 8.5$ as a representative magnitude from this sample.

The Palomar 200" telescope would take about 0.074 seconds to reach SNR=8 per resolution element, given the assumptions in Tables 2.1 and 2.2. For 139 scans, each with 200 0.074 s phase steps, the 200" telescope would require about 0.57 hours to reach a radial velocity precision of 10 cm s^{-1} . It is therefore possible to reach the radial velocity precision necessary to detect Earth-like planets around Sun-like stars using existing, 5-meter-class telescopes.

2.6 Conclusions

The current state-of-the-art radial velocity instruments are limited by their ability to maintain their system's wavelength solution in the presence of slowly varying instrumental noise. Lock-in amplification, however, can suppress such long timescale noise sources, while decoupling the effects of wavelength calibration errors from radial velocity precision. The simulations presented in this chapter indicate that lock-in amplified, externally-dispersed interferometry is a possible path forward to reach the radial velocity precision necessary to detect Earth-Sun analog systems on existing, medium-sized telescopes.

ACKNOWLEDGEMENTS

This material is based upon work supported by the National Science Foundation Graduate Research Fellowship under Grant No. DGE-1144469. P.S.M. acknowledges support for his work from the Hubble Fellowship Program, provided by NASA through Hubble Fellowship grant HST-HF-51326.01-A awarded by the STScI, which is operated by the AURA, Inc., for NASA, under contract NAS 5-26555. P.S.M, G.V., and J.K.W. were supported by the Directors Research and Development Fund and Caltech-JPL President and Director's fund at the California Institute of Technology/Jet Propulsion Laboratory. M.B. is supported by a National Space Technology Research Fellowship. J.A.J. is supported by generous grants from the David and Lucile Packard Foundation and the Alfred P. Sloan Foundation. J.K.W. and G.V. are supported by the Caltech-JPL President and Director's fund. We would like to thank Lynne Hillenbrand for useful discussions.

Chapter 3

POINT SOURCE POLARIMETRY WITH THE GEMINI PLANET
IMAGER: SENSITIVITY CHARACTERIZATION WITH T5.5
DWARF COMPANION HD 19467 B

ABSTRACT

Detecting polarized light from self-luminous exoplanets has the potential to provide key information about rotation, surface gravity, cloud grain size, and cloud coverage. While field brown dwarfs with detected polarized emission are common, no exoplanet or substellar companion has yet been detected in polarized light. With the advent of high contrast imaging spectro-polarimeters such as GPI and SPHERE, such a detection may now be possible with careful treatment of instrumental polarization. In this chapter, we present 28 minutes of *H*-band GPI polarimetric observations of the benchmark T5.5 companion HD 19467 B. We detect no polarization signal from the target, and place an upper limit on the degree of linear polarization of $p_{\text{CL}99.73\%} \leq 2.4\%$. We discuss our results in the context of T dwarf cloud models and photometric variability.

3.1 Introduction

Recent imaging spectroscopy of directly imaged planets such as β Pic b, HR 8799 bcd, and 51 Eri b (Chilcote et al., 2015; Ingraham et al., 2014; B. Macintosh et al., 2015) has demonstrated that this technique will soon become routine. At the same time, these early studies have underscored the challenges of fitting atmospheric models based on field brown dwarf spectra to exoplanets with comparatively low masses and surface gravities (Barman et al., 2011; M. S. Marley et al., 2012). For instance, the HR 8799 planets' red colors are consistent only with models that include dusty, patchy clouds and non-equilibrium chemistry, but these scenarios require radii that are inconsistent with the predictions of evolutionary models (C. Marois, B. Macintosh, et al., 2008; B. P. Bowler et al., 2010; Ingraham et al., 2014). The spectra of β Pic b gathered to date also require a cloudy atmosphere, but even the best fitting models contain large (5% – 10%) systematic offsets from the data (Chilcote et al., 2015). These and other studies indicate that clouds are common in planetary atmospheres, but current atmospheric models require a more detailed treatment of cloud physics (e.g. dust grain size distributions, grain chemistry, and large scale opacity holes, or "patchy" cloud regions).

Polarimetry is well-suited to the problem of analyzing planetary atmospheres. As early as 1929, Bernard Lyot published reflected light polarimetry of Venus as a means of probing the planet's cloud composition (B. Lyot, 1929). In the modern era of exoplanet astronomy, at least 10 years of theoretical work have been devoted to the polarization of *reflected starlight* by a close-in directly imaged exoplanet (Schmid et al., 2006; Stam, 2008; Buenzli and Schmid, 2009). In this chapter, we address a separate regime of exoplanet polarimetry: scattering by grains in the atmospheres of *cloudy, self-luminous* exoplanets, which induces polarization of *thermally emitted radiation* in the near infrared (Sengupta and M. S. Marley, 2009; M. S. Marley and Sengupta, 2011; Kok, Stam, and Karalidi, 2011). While Rayleigh scattering in the atmospheres of cloud-free exoplanets can polarize visible wavelength radiation, we concentrate on the case of \sim micron sized dust grains that polarize infrared radiation, where young, self-luminous exoplanets emit the bulk of their radiation.

A perfectly spherical, uniformly cloudy planet, however, would have zero disk-integrated polarization. In order to produce a non-zero polarization signature when the planet is viewed as a point source, the clouds must be nonuniformly distributed (e.g. patchy or banded) and/or the body must be oblate (Basri, 2000; Sengupta and Krishan, 2001). Both of these characteristics have been invoked to explain the ob-

served polarization of brown dwarfs in the field. Time-varying polarimetric signals indicate evolving or rotating nonuniform cloud distributions, while comparisons of fast and slow brown dwarf rotators show that oblate bodies are more likely to produce observable polarimetric signals than spherical bodies (Ménard, Delfosse, and Monin, 2002; Osorio, Caballero, and Bejar, 2005; Goldman et al., 2009; Tata et al., 2009; Zapatero Osorio et al., 2011; Miles-Páez et al., 2013). For example, Miles-Páez et al. (2013) found that $40 \pm 15\%$ of rapidly rotating ($v \sin i \geq 30 \text{ km s}^{-1}$) M7-T2 dwarfs are linearly polarized in the Z - and J -bands, with linear degrees of polarization of $0.4\% - 0.8\%$. The fastest rotators ($v \sin i > 60 \text{ km s}^{-1}$) were more frequently polarized, and had larger detected polarizations compared to moderate rotators ($v \sin i = 30 - 60 \text{ km s}^{-1}$). Furthermore, polarimetry in different broad wavelength bands has provided a diagnostic of grain sizes (Osorio, Caballero, and Bejar, 2005).

These field observations set the stage for exoplanet and brown dwarf companion polarimetry. Because models and field dwarf observations agree that the cloud-induced degree of linear polarization is generally $p \leq 1\%$, the observational challenge is to reach the companion-to-star contrast ratio and absolute polarimetric accuracy needed to detect such small signals. SPHERE (Beuzit et al., 2008) and GPI (B. A. Macintosh et al., 2008; B. Macintosh et al., 2014) are the first spectro-polarimeters capable of achieving contrasts $< 10^{-5}$ at separations $< 1''$ and an absolute accuracy in the degree of linear polarization of $p < 0.1\%$ in the near infrared (Wiktorowicz et al., 2014). These instruments are poised to make the first detections of polarized light from substellar companions, providing a powerful new tool for atmospheric characterization.

In order to assess GPI's accuracy in linear polarization for point sources, we observed the benchmark T dwarf HD 19467 B for 28 minutes of integration time on February 1st 2015. HD 19467 B is unique among substellar companions in that it is the only T dwarf with a solar-analog primary to be detected both as a long term trend in RV measurements and by direct imaging (J. R. Crepp, J. A. Johnson, A. W. Howard, G. W. Marcy, Fischer, et al., 2012). Recently, J. R. Crepp et al. (2015) determined a spectral type of $T5.5 \pm 1$ and an effective temperature of $T_{\text{eff}} = 978_{-43}^{+20} \text{ K}$ (see Table 3.1 below) using the Project 1640 integral field spectrograph at Palomar Observatory (S. Hinkley et al., 2011). While mid T dwarfs are generally thought to be cloudless, HD 19467 B was the only brown dwarf companion or exoplanet meeting GPI's observability requirements ($I < 9$ parent star and planet-star separation $< 2.0''$) at

the time of the pathfinder experiment.

We describe our observational methods and Stokes parameter extraction in Section 3.2. In Section 3.3 we measure the degree of linear polarization at the location of the companion and empirically estimate GPI’s polarimetric point source sensitivity. In Section 3.4, we place our results in the context of field T dwarf observations and discuss our upcoming GPI campaign for exoplanet polarimetry.

Table 3.1: HD 19467 System Properties, After J. R. Crepp, J. A. Johnson, A. W. Howard, G. W. Marcy, Brewer, et al. (2014) and J. R. Crepp et al. (2015)

HD 19467 A Properties	
J	5.801 ± 0.020
H	5.447 ± 0.036
K_s	5.401 ± 0.026
Mass [M_\odot]	0.95 ± 0.02
Radius [R_\odot]	1.15 ± 0.03
Luminosity [L_\odot]	1.34 ± 0.08
T_{eff} [K]	5680 ± 40
SpT	G3V
d [pc]	30.86 ± 0.60
Age, multiple techniques [Gyr]	4.6 - 10
[Fe/H]	-0.15 ± 0.04
HD 19467 B Properties	
J	17.61 ± 0.11
H	17.90 ± 0.11
K_s	17.97 ± 0.09
Mass [M_{Jup}]	$\geq 51.9^{+3.6}_{-4.3}$
T_{eff} [K]	978^{+20}_{-43}
SpT	T5.5 \pm 1
Separation [AU, as]	$51.1 \pm 1.0, 1.65''$

3.2 Observations and Data Reduction

We briefly summarize GPI’s polarimetric mode here; for details, see B. Macintosh et al. (2014), Wiktorowicz et al. (2014), and M. D. Perrin, Duchene, et al. (2015). In polarimetry mode, a Wollaston prism replaces the integral field spectrograph’s dispersing prism, and an achromatic half waveplate is inserted between the coronagraph’s focal plane and Lyot mask. In an observing sequence, the waveplate is rotated after each exposure in steps of 22.5° . GPI operates in angular differential imaging (ADI) mode, allowing the sky to rotate with respect to the telescope pupil. The Stokes datacube [$x, y, (I, Q, U, V)$] describing the astronomical polariza-

tion is extracted from the raw data by inverting the Mueller matrix whose elements represent the polarization induced by the instrument and sky rotation. A detailed description of the Stokes cube extraction can be found in M. D. Perrin, Duchene, et al. (2015).

The observing sequence consisted of twenty-eight 60s exposures in the H -band, where each sequence of four exposures cycled through the waveplate angles 0.0° , 22.5° , 45.0° , and 67.5° . The exposures were taken from Modified Julian Day 57054.0536728 to 57054.0773418 and the airmass ranged from 1.21 to 1.32. The total field rotation was 4° . The observations were taken under Gemini program number GS-2014B-Q-503.

In this study, the Stokes datacube was constructed from the raw data using a modified version of the publicly available GPI pipeline v1.2.1 (Maire et al., 2010; M. D. Perrin, Maire, et al., 2014). Modifications, which will be released in a future version of the pipeline, included improved flat fielding and instrumental polarization subtraction. The latter was achieved by measuring the fractional polarization inside the coronagraphic mask, which was assumed to contain only diffracted starlight affected by instrumental polarization, on each polarization difference cube. The instrumental polarization was then subtracted from the image as a whole, by multiplying the measured fractional polarization by the total intensity at each spatial location. This method was introduced by Millar-Blanchaer et al. (2015), who found similar instrumental polarization levels as those measured using the same dataset by Wiktorowicz et al. (2014). The method used in Wiktorowicz et al. (2014) to estimate the instrumental polarization measures the fractional polarization in each frame using aperture photometry on the occulted PSF, and fits an instrumental polarization model that leverages the field rotation within their dataset to distinguish between an astrophysical source and the instrumental polarization. The method used here and in Millar-Blanchaer et al. (2015) has the advantage of operating on each polarization datacube individually and therefore this method does not rely on sky rotation. While promising for point source polarimetry data, techniques such as LOCI or PCA that take greater advantage of the sky rotation to reduce instrumental polarization are beyond the scope of this chapter. Section 3.3 briefly describes how our results could be improved by these techniques.

Spurious pixels in the Stokes cube were replaced with values obtained by interpolation over pixels with counts greater than three standard deviations from the mean, and the detector's gain of $3.04e^-/\text{ADU}$ was applied to convert the raw counts to

electrons (this gain is reported in the FITS headers of all GPI data cubes). The final reduced Stokes I, Q, and U images are shown in Figure 1. The four bright areas in the corners of the Stokes I frame (Figure 1a) are satellite spots used for photometric and astrometric calibration in GPI’s imaging spectroscopy mode. HD 19467 B is readily visible on the righthand side of the Stokes I frame, but is not apparent in the Stokes Q or U frames. In the next section, we will calculate the companion’s signal-to-noise ratio in each Stokes frame, and comment on the degree of linear polarization at the companion’s location.

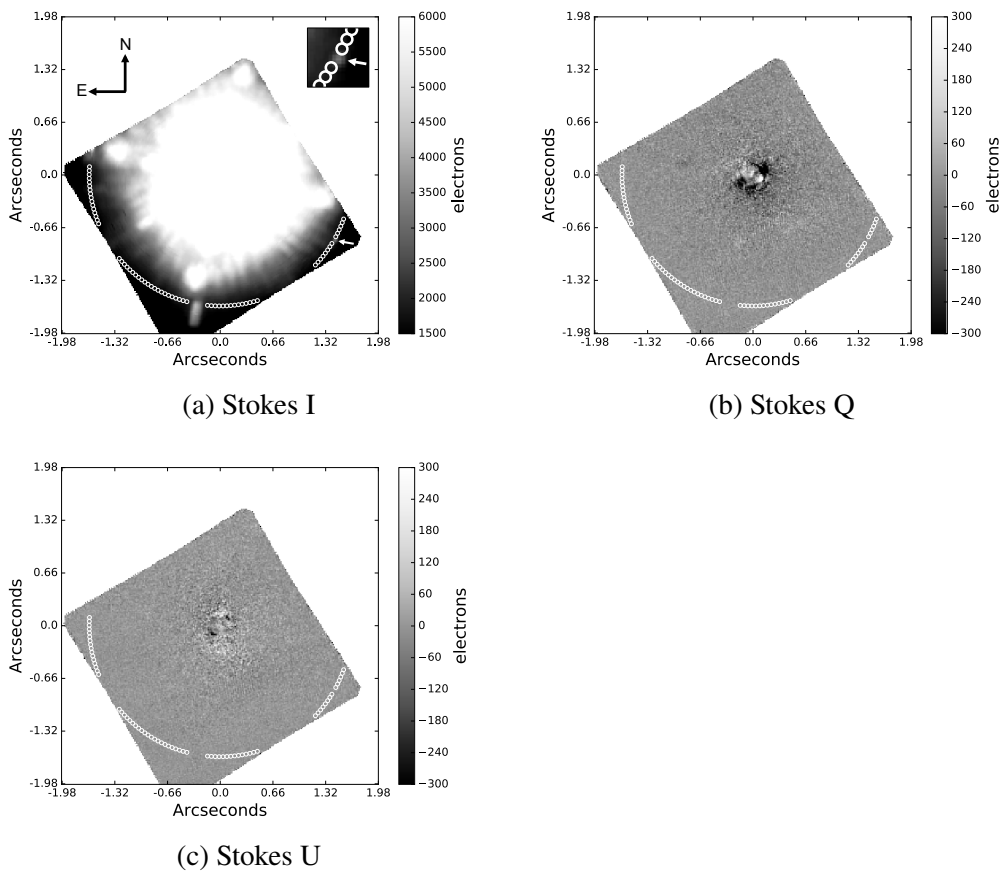


Figure 3.1: The reduced Stokes images with the ring of comparison apertures superimposed (the white arrow indicates the companion in Stokes I). The companion’s SNR (Equation 3.1) is 7.4 in Stokes I, but $\text{SNR} < 1.0$ in Stokes Q and U. Hence, no polarized radiation is detected from the companion.

3.3 Polarimetric Analysis

A linearly polarized companion would produce signal in the Stokes Q and/or U frames at the same location as the companion’s signal in the Stokes I frame. In order to determine whether we detect polarized radiation from HD 19467 B, we must

therefore calculate the signal-to-noise ratio (SNR) in an aperture at the companion's location in each of the Stokes frames.

In order to choose the optimal aperture size, we first estimate the companion's full width at half maximum (FWHM) in the Stokes I frame by fitting the sum of a 2D Gaussian distribution and a plane to an 11×11 pixel ($\approx 3 \times 3$ FWHM) window around the companion's PSF. The plane component was included to account for the shape of the parent star's halo at the companion's location. The FWHM is found to be 3.44 pixels, or 0.049", which is consistent with the diffraction limit of $\lambda/D=0.041''$ in the *J* band.

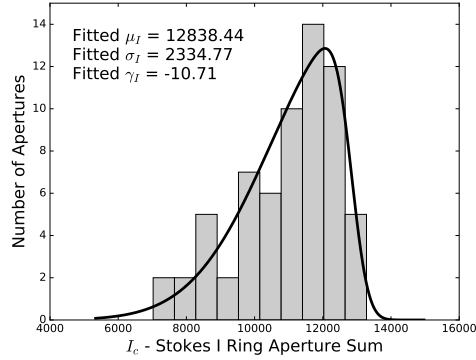
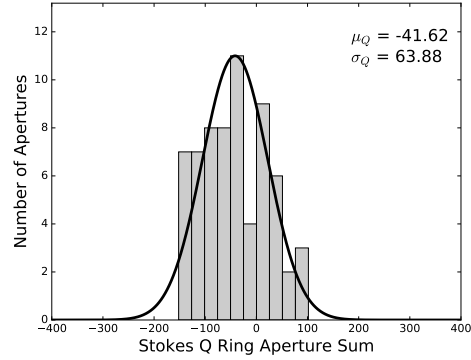
The optimal aperture size for photometry will maximize the companion's signal-to-noise ratio in the Stokes I frame. The "signal" is the difference of the sum of the counts inside the companion's aperture and the contribution from the parent star's residual halo at the companion's separation. This halo contribution is found by constructing a ring of apertures around the parent star at the same separation as the companion. These comparison apertures, shown in Figure 1, do not form a complete ring because the parent star was offset from the detector's center to allow for more sky rotation of the companion. We also deleted those apertures that fall within a FWHM of the bright astrometric spots. Despite these removals, the effect of small sample statistics is negligible here (Mawet et al., 2014). For each aperture size, the total number of apertures is modified to prevent them from overlapping. We then sum the flux in each of these comparison apertures. A histogram of the Stokes I aperture sums is shown in Figure 2a. The histogram is asymmetric due to the competing effects of the modified Rician statistics governing speckle noise and the whitening of those statistics after ADI reduction. We take the parent star's halo contribution to the flux inside the companion's aperture to be the mean of the comparison apertures sums, μ_I , and the noise to be the standard deviation of the comparison aperture sums, σ_I . The signal to noise ratio is therefore

$$\text{SNR} = \frac{I_c - \mu_I}{\sigma_I}, \quad (3.1)$$

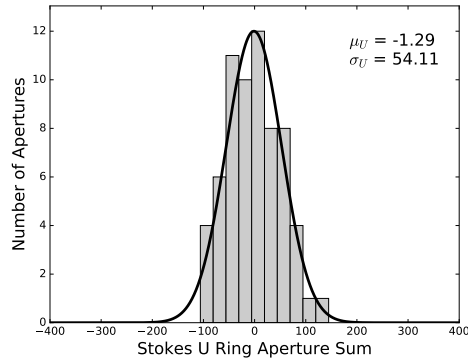
where the *c* subscript denotes the sum of the counts inside the companion's aperture ($I_c = 26127.4e^-$). The signal-to-noise reached a maximum of $\text{SNR}_I = 7.4$ for an aperture diameter of $1 \times \text{FWHM}$. The "aper" aperture photometry tool provided by the IDL Astronomy User's Library was used to compute all aperture sums.

To calculate the SNR in the Stokes Q and U frames, we use the same comparison aperture size and locations as in the Stokes I frames. The histograms of the aperture

sums in the Stokes Q and U frames are shown in Figure 2b,c. We take the parent star's halo contribution to the flux inside the companion's aperture in the Q and U frames to be the means of the aperture sums, μ_Q and μ_U , and the noise terms to be the standard deviations σ_Q and σ_U of the aperture sums. Following Equation 3.1, we find that $Q_c = -99.0$ and $U_c = 41.7$, while $\text{SNR}_Q = 0.90$ and $\text{SNR}_U = 0.79$. We therefore conclude that we do not detect any polarized radiation from HD 19467 B.

(a) I_c - Stokes I aperture sum histogram

(b) Stokes Q aperture sum histogram



(c) Stokes U aperture sum histogram

Figure 3.2: Histograms of the summed counts in the Stokes comparison apertures. The aperture size is equal to the full width at half maximum of the companion (3.44 pixels, or 0.049"). The Stokes I histogram (a) has an excess of higher values due to speckle noise. Because HD 19467 A is an unpolarized star, there is little flux at the companion's separation in the Q and U frames. The large spread in Q and U values is due in part to the small number of apertures used (66).

Our goal now is to place an upper limit on the companion's linear polarization fraction, p . In general, p is defined as

$$p = \frac{\sqrt{Q^2 + U^2}}{I}. \quad (3.2)$$

Our strategy will be to compute the probability density function (PDF) of p , and take the representative upper limits on p to be the upper bounds of the 68.27%, 99.73%, and 99.9999% confidence intervals.

We take the PDFs of Q and U to be Gaussian distributions with means and standard deviations matching those of the Q and U aperture sums via maximum likelihood estimation. We compute the PDF of $\sqrt{Q^2 + U^2}$ using the formalism of Aalo, Efthymoglou, and Chayawan (2007), which considers the most general case of the PDF of $R = \sqrt{X_c^2 + X_s^2}$ where X_c and X_s are correlated real Gaussian random variables with means μ_c , μ_s and standard deviations σ_c , σ_s . Aalo, Efthymoglou, and Chayawan, 2007 first rotate (X_c, X_s) through the angle ϕ , chosen such that the new coordinates (Y_1, Y_2) are uncorrelated:

$$Y_1 = X_c \cos \phi + X_s \sin \phi, \quad (3.3a)$$

$$Y_2 = -X_c \sin \phi + X_s \cos \phi, \quad (3.3b)$$

$$\phi = \frac{1}{2} \tan^{-1} \left(\frac{2\rho\sigma_c\sigma_s}{\sigma_c^2 - \sigma_s^2} \right), \quad (3.3c)$$

where ρ is the correlation coefficient between X_c and X_s . The full derivation of the PDF of R is beyond the scope of this chapter, but we quote the result here and refer to Aalo, Efthymoglou, and Chayawan (2007) for a more detailed treatment. The final PDF is given by

$$\begin{aligned} f_R(r) = & \frac{r}{2\sigma_1\sigma_2} \exp \left[-\frac{1}{2} \left(\frac{r^2}{2\sigma_1^2} + \frac{r^2}{2\sigma_2^2} + \frac{\mu_1^2}{\sigma_1^2} + \frac{\mu_2^2}{\sigma_2^2} \right) \right] \\ & \sum_{n=0}^{\infty} \frac{\varepsilon_n I_n \left(\frac{r^2}{4} \left(\frac{1}{\sigma_2^2} - \frac{1}{\sigma_1^2} \right) \right)} \left[\left(\frac{\mu_1 r}{\sigma_1^2} \right)^2 + \left(\frac{\mu_2 r}{\sigma_2^2} \right)^2 \right]^n \left\{ I_{2n} \left(\sqrt{\left(\frac{\mu_1 r}{\sigma_1^2} \right)^2 + \left(\frac{\mu_2 r}{\sigma_2^2} \right)^2} \right) \right. \\ & \left. \sum_{k=0}^n \delta_k C_k^n \left[\left(\frac{\mu_1 r}{\sigma_1^2} \right)^2 - \left(\frac{\mu_2 r}{\sigma_2^2} \right)^2 \right]^{n-k} \left(\frac{2(\mu_1 \mu_2 r^2)}{\sigma_1^2 \sigma_2^2} \right)^k \right\}, \end{aligned} \quad (3.4)$$

where μ_1 , μ_2 and σ_1 , σ_2 are the mean and standard deviations of Y_1 and Y_2 , $\varepsilon_{n=0} = 1$ and $\varepsilon_{n \neq 0} = 2$, $\delta_{k_{\text{odd}}} = 0$ and $\delta_{k_{\text{even}}} = 2(-1)^{k/2}$, C_k^n is the binomial coefficient, and I_n is the n -th order modified Bessel function of the first kind. We find that Equation 3.4 gives consistent results to within machine precision after five terms.

We find that the PDF of $\sqrt{Q^2 + U^2}$ is negligibly affected by the assumption that U and Q are uncorrelated. The PDF is fit by a Hoyt distribution, which is equivalent to Equation 3.4 for the special case of $\mu_Q = \mu_U = 0$.

To find the PDF of $p = \frac{\sqrt{Q^2+U^2}}{I}$, we first assume that $\sqrt{Q^2+U^2}$ and I are uncorrelated. The PDF of I represents the distribution of *companion* intensity values, and is therefore taken to be the counts in the companion's aperture, I_c , minus the distribution of counts in the comparison apertures. The comparison apertures' Stokes I distribution is influenced by both the modified Rician distribution governing speckle statistics and the whitening effects of angular differential imaging. Hence, we take $p_I(i)$ to be the skewed Gaussian distribution fit to the histogram of I_c - aperture I sums shown in Figure 2a. Because the width, σ_I , of Figure 2a is $> 10\times$ larger than $\sqrt{I_c}$, the contribution of the companion's Poisson noise to $p_I(i)$ is neglected. For $R = \sqrt{Q^2+U^2}$, the CDF of $p = R/I$ is the probability that R/I is less than a given value of p , or

$$F_p(p) = P(R/I \leq p), \quad (3.5a)$$

$$F_p(p) = \int_{i=0}^{+\infty} \int_{r=-\infty}^{ip} f_{RI}(r, i) dr di + \int_{i=-\infty}^0 \int_{r=ip}^{\infty} f_{RI}(r, i) dr di. \quad (3.5b)$$

Differentiating with respect to p gives the final PDF of the linear polarization fraction:

$$f_p(p) = \int_{-\infty}^{\infty} |I| f_R(Ip) f_I(i) di. \quad (3.6)$$

The calculated values of $f_p(p)$ and several fitted distributions are shown Figure 3.3. We find that $f_p(p)$ is best fit by a Hoyt distribution. Table 3.2 lists the upper limits to the linear polarization fraction corresponding to three representative confidence intervals calculated using the fitted Hoyt distribution. We emphasize that our analysis described in this section is distinct from that of disk polarimetry, which benefits from the assumption that light scattered by a disk is polarized in the direction perpendicular to the direction towards the central star. To our knowledge, this work presents the first analysis of point source polarimetric precision using a high contrast, integral field polarimeter.

We now return to the question of how our limiting polarization fraction would be affected by greater sky rotation and algorithms such as PCA (R. Soummer, L. Pueyo, and Larkin, 2012) and LOCI (D. Lafrenière, C. Marois, Renè Doyon, et al., 2007) that help attenuate quasi-static speckles caused by instrumental effects. The shape of the polarization fraction's PDF is governed by the PDFs of the Stokes I, Q, and U histograms shown in Figure 2. The width of the Stokes I PDF is larger than expected based on photon noise alone – the standard deviation of the aperture values is $1479.6e^-$, while the square root of the mean is $104.7e^-$. This

extra width is primarily due to speckle noise, which increases the distribution’s standard deviation and skewness (C. Marois, D. Lafrenière, B. Macintosh, et al., 2008). Because speckles are mostly unpolarized, however, their flux is attenuated in the Stokes Q and U frames. Visual inspection of the polarized channels in Figure 1 confirm that speckles, and hence speckle noise, are not present at the companion’s separation. Indeed, M. D. Perrin, Duchene, et al. (2015) demonstrate that in GPI’s polarimetric mode the polarized intensity, $\sqrt{Q^2 + U^2}$, at HD19467 B’s separation of 1.65" is dominated by photon noise (see also B. R. Oppenheimer et al. (2008) and S. Hinkley, B. R. Oppenheimer, R emi Soummer, et al. (2009)). Hence, greater sky rotation and PSF subtraction techniques would reduce the contribution of speckle noise to the PDF of Stokes I, but would not significantly affect the PDFs of Stokes Q and U. To assess the contribution of non-photon noise to our p upper limits, we replace the PDF of Stokes I values shown in Figure 2a with a poisson distribution of $\mu = \mu_I$. The resulting p upper limits are 0.9%, 1.8%, and 2.7%, for the confidence intervals of 68.27%, 99.73%, and 99.9999%, respectively. Speckle reduction techniques would therefore provide some improvement to our limiting polarization fraction, but our assessment is dominated by the noise in the polarized channels.

Table 3.2: Degree of Linear Polarization Upper Limits

Confidence Interval	p upper limit
68.27%	1.2%
99.73%	2.4%
99.9999%	3.8%

3.4 Discussion

Recent observations of photometric variability outside the L/T transition hint at the presence of cloud variability that might lead to a non-zero polarization signatures in a T5.5 dwarfs such as HD 19467 B. J. Radigan et al. (2014) detected J -band 1.6% peak-to-peak variability in a red T6.5 dwarf, and 0.6% – 0.9% variability in three additional T dwarfs later than T3.5 without remarkably red colors. Photometric monitoring at 3 – 5 μ m with Spitzer revealed that 19 – 62% of T0-T8 dwarfs vary with peak-to-peak amplitudes $> 0.4\%$, with T0-T-3.5 objects in the L/T transition showing no higher incidence of variability than later type T dwarfs (Metchev et al., 2015). The source of this variability may be due to variations in cloud coverage and thicknesses, or “patchy” clouds. While it has been recently suggested that temperature variations driven by atmospheric changes below the cloud layer may also

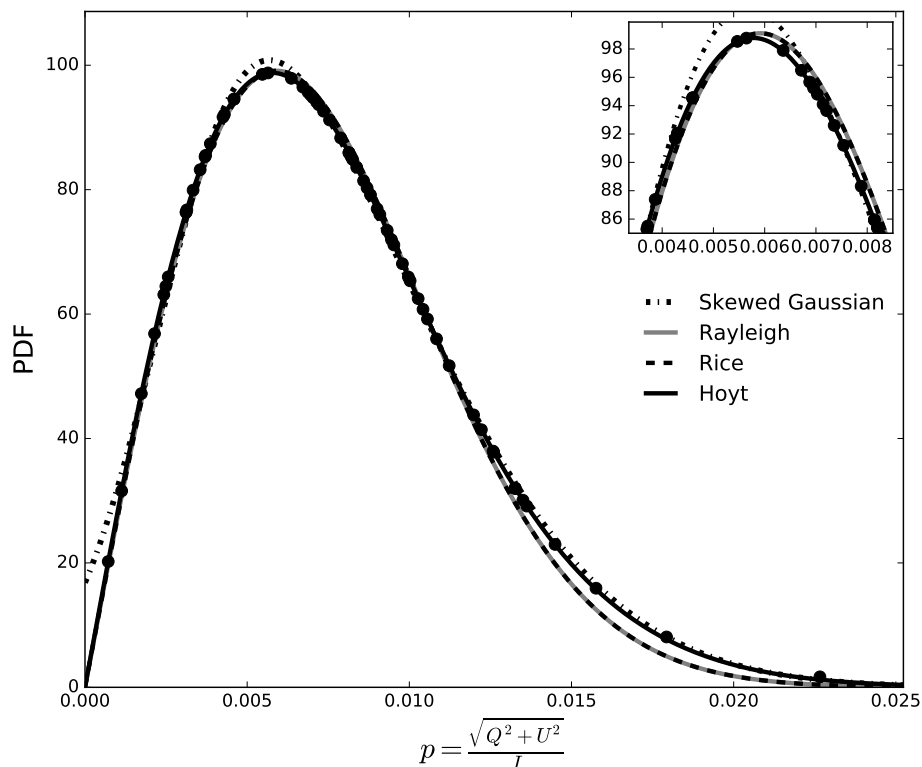


Figure 3.3: The probability density function of $p = \frac{\sqrt{Q^2+U^2}}{I}$, via Equation 3.6. The four fits are to skewed Gaussian, Rayleigh, Rice, and Hoyt distributions. All but the skewed Gaussian are special cases of Equation 3.4 for different values of the means and standard deviations of Q and U . The best fit is the Hoyt distribution.

contribute to photometric variability (e.g. Robinson and M. S. Marley (2014)), Apai, J. Radigan, et al. (2013) and J. Radigan et al. (2012) have shown that temperature fluctuations alone cannot reproduce the observed amplitudes of variability.

The results of these photometric surveys suggest that even outside the L/T transition, T dwarfs commonly have time-varying cloud and spot weather patterns. These variations may produce polarized intensity: Kok, Stam, and Karalidi (2011) show that a fixed hotspot on the surface of an otherwise uniformly cloudy dwarf produces a higher amplitude of polarimetric variability as a function of time than flux variability. The difficulty of detecting a linear degree of polarization of less than 1.0%, however, has prevented observers from testing this theoretical link between photometric and polarimetric variability. For example, SIMP J013656.57+093347.3 is a T2.5 dwarf with periodic large amplitude (50 mmag) variability, which is explained by invoking cool dusty cloud patches against a warmer clear background (Artigau, R. Doyon,

et al., 2006; Artigau, Bouchard, et al., 2009). However, Zapatero Osorio et al. (2011) find no polarization, and place an upper limit of $p < 0.9\%$ on the J -band degree of linear polarization.

In fact, only two T-dwarfs have published near-infrared polarimetric observations: the aforementioned SIMP J013656.57+093347.3 T2.5 dwarf observed by Zapatero Osorio et al. (2011), and 2MASS J12545393-0122474, a T2 dwarf observed by Miles-Páez et al. (2013) with a linear degree of polarization of $p = 0.00\% \pm 0.34\%$. Our observations of HD 19467 B constitute the third polarimetric observation of a T dwarf, and the third null result. We also note that our upper limit of $p_{\text{CL}99.73\%} \leq 2.4\%$ is within a factor of a few of the previously mentioned T-dwarf upper limits, demonstrating that high contrast, integral field polarimeters are approaching the performance of direct polarimetric imaging modes.

While these null results could be due to unfavorable viewing angles or insufficient detection limits, it is also possible that these T-dwarfs are simply cloudless, and hence would not polarize infrared radiation. Multiple scattering polarization models for cloudless T dwarfs indicate negligible polarization signals at wavelengths longer than $0.6\mu\text{m}$ at a range of inclinations and rotational velocities (Sengupta and M. S. Marley, 2009). These results are consistent with non-detections of near infrared T dwarf polarization.

Clearly, more targets must be observed at higher polarimetric precisions in order to draw meaningful conclusions about the cloud properties of brown dwarfs and exoplanets. Our upper limit of $p_{\text{CL}99.73\%} \leq 2.4\%$ is within a factor of a few of the predicted $p \leq 1.0\%$ signature of a cloudy, oblate body (M. S. Marley and Sengupta, 2011), suggesting that GPI is capable of detecting polarized radiation from substellar companions given sufficient integration times to reduce photon noise in the polarized channels. To this end, our group is actively pursuing a GPI program to observe several exoplanet and brown dwarf companions at the predicted $p \leq 1.0\%$ level. Observing multiple targets will reduce the risk of non-detections resulting from unfavorable viewing angles, and may shed light on the diversity of low-mass polarimetric properties.

3.5 Conclusion

We observed the T5.5±1 dwarf HD 19467 B in the H band for 28 minutes on February 1st 2015 using the Gemini Planet Imager’s polarimetry mode. We detect no polarization signal from the target, and place an upper limit on the degree of linear

polarization of $p_{\text{CL99.73\%}} \leq 2.4\%$. Because this limit is larger than the predicted $p \leq 1.0\%$ signature of a cloudy, oblate body, we cannot constrain the atmospheric properties of HD 19467 B from this measurement. Our method for analyzing point source polarimetry data, however, will be applied to our upcoming GPI survey for which we expect to reach $p \leq 1.0\%$ for multiple exoplanet and brown dwarf companions.

The future of exoplanet polarimetry is promising: because the breakup of clouds usually associated with the L/T transition occurs at lower temperatures for lower surface gravity objects, exoplanet polarimetry signals will likely benefit from the surface asymmetries introduced by patchy clouds. Indeed, J. Radigan et al. (2014) show that HR8799 c falls near the highest amplitude photometric variables in NIR color magnitude diagrams, a region populated by L/T transition objects.

With the advent of modern high contrast spectro-polarimeters such as GPI and SPHERE, we are entering a new era of complementary photometric and polarimetric observations of exoplanets and brown dwarf companions. Future exoplanet polarimetric detections have the power to inform cloud particle size distributions at different pressures and corroborate the interpretations of L and T photometric survey results. Brown dwarf and exoplanet atmosphere models are currently limited by our understanding of cloud physics and its effects on observables; polarimetry is an as-yet unexploited tool to fill in these gaps.

ACKNOWLEDGEMENTS

This material is based upon work supported by the National Science Foundation Graduate Research Fellowship under Grant No. DGE-1144469. This work was performed in part under contract with the California Institute of Technology (Caltech) funded by NASA through the Sagan Fellowship Program executed by the NASA Exoplanet Science Institute, and under the auspices of the U.S. Department of Energy by Lawrence Livermore National Laboratory under Contract DE-AC52-07NA27344.

*Chapter 4***A NEW STANDARD FOR ASSESSING THE PERFORMANCE
OF HIGH CONTRAST IMAGING SYSTEMS**

ABSTRACT

As planning for the next generation of high contrast imaging instruments (e.g. WFIRST, HabEx, and LUVOIR, TMT-PFI, EELT-EPICS) matures, and second-generation ground-based extreme adaptive optics facilities (e.g. VLT-SPHERE, Gemini-GPI) are halfway through their principal surveys, it is imperative that the performance of different designs, post-processing routines, observing strategies, and survey results be compared in a consistent, statistically robust framework. In this chapter, we argue that the current industry standard for such comparisons – the contrast curve – falls short of this mandate. We propose a new figure of merit, the “performance map,” that incorporates three fundamental concepts in signal detection theory: the true positive fraction (TPF), false positive fraction (FPF), and detection threshold. By supplying a theoretical basis and recipe for generating the performance map, we hope to encourage the widespread adoption of this new metric across subfields in exoplanet imaging.

4.1 Introduction

The contrast curve describes an imaging system’s sensitivity for a given detection significance in terms of the planet/star flux ratio and angular separation. A consistent methodology for computing the contrast curve, however, is lacking: a variety of approaches to throughput, small sample-size, and non-Gaussian noise corrections are represented in the literature (e.g. C. Marois, D. Lafrenière, B. Macintosh, et al., 2008; Wahhaj et al., 2013; Mawet et al., 2014; L. Pueyo, 2016; Otten et al., 2017). As inner working angles are pushed below $5\lambda/D$, these details dominate the calculation of the contrast curve. Secondly, the contrast curve’s information content is limited: by fixing the detection significance for all separations, the contrast curve conceals important trade offs between the choice of detection criteria, false positive rates, and detection completeness statistics.

The purpose of this chapter is to critically examine the contrast curve and present alternative figures of merit for the ground and space-based exoplanet imaging missions of the coming decades. In Section 4.2, we summarize the key points of signal detection theory, which provide the basis for our discussion of performance metrics. Section 4.3 describes the strengths and weaknesses of the contrast curve as a general purpose performance metric. Finally, Section 4.4 gives our proposal for a new figure of merit based on signal detection theory.

4.2 Overview of Signal Detection Theory

Our task as planet hunters is to decide whether the data at each location in a “high contrast” image meets our criteria for a planet detection. Regardless of the details of the dataset (e.g. field rotation, spectral coverage, etc.), the presence of noise will interfere with the accuracy of our detection decisions. Signal detection theory provides a precise framework for describing the relationships between detections, non-detections, and detection criteria.

If we assume that a planet is present at a location of interest in our data (the H_1 , or “signal present” hypothesis), and we succeed in detecting that planet, our result is a true positive (TP). If we fail to detect the planet, our result is a false negative (FN). Clearly, we aim to maximize the number of true positives while minimizing the number of false negatives. Hence, we define a true positive fraction, or TPF:

$$\text{TPF} = \frac{\text{TP}}{\text{TP} + \text{FN}} = \int_{\tau}^{+\infty} pr(x|H_1)dx, \quad (4.1)$$

where τ is the threshold of the detection criterion and $pr(x|H_1)$ is the probability

density function (PDF) of the data x under the hypothesis H_1 . Our goal is to approach TPF= 1.

If we instead assume that no planet is present in the data (the H_0 , or “signal absent” hypothesis), and we fail to make a detection, our result is a true negative (TN). If we incorrectly claim to detect a planet, however, our result is a false positive (FP). We are then interested in achieving a false positive fraction (FPF) close to zero:

$$\text{FPF} = \frac{\text{FP}}{\text{TN} + \text{FP}} = \int_{\tau}^{+\infty} pr(x|H_0)dx. \quad (4.2)$$

These various hypotheses and outcomes are summarized in the “confusion matrix” (Figure 4.1). An early review of signal detection theory is given by J. Swets, Tanner, and Birdsall (1961).

	H_1 : Signal Present	H_0 : Signal Absent
Detection	True Positive	False Positive
Null Result	False Negative	True Negative
	True Positive Fraction = TP/(TP+FN)	False Positive Fraction = FP/(FP+TN)

Figure 4.1: The Confusion Matrix

To make these relationships concrete, consider a post-processed image in which the pixel intensities, x , in a certain annulus around the central star are drawn from a normal distribution ($\mu = 0$ and $\sigma = 1$, where the choice of an annular region is justified by the symmetry of the star’s point spread function). The PDF of the noise is shown in Figure 4.2a. Now let us assume that our goal is to detect a planet with a mean intensity of $x = 3$ inside the annulus of interest. Because the pixels at the planet’s location are also affected by the noise, they are described by a PDF identical to that of the noise, but with a mean of $x = 3$ (here, we ignore the contribution of the planet’s shot noise). The PDF of the signal is shown in Figure 4.2b.

Given our knowledge of the PDFs of the noise and the signal, we now wish to choose a detection criterion. Let us assume that because our detection follow-up resources (e.g. telescope time) are limited, we wish to achieve a false positive fraction of 0.001. We therefore choose a detection criterion of 3σ because a fraction 0.001 of the area of the noise PDF falls above this value (4.2a, dotted line). A second

consequence of this choice of detection criterion is that we will only detect half of all planets with a mean intensity of $x = 3$ (TPF= 0.5; 4.2b, dotted line). If we wish to increase the TPF, we must lower the detection criterion and hence unfavorably raise the FPF.

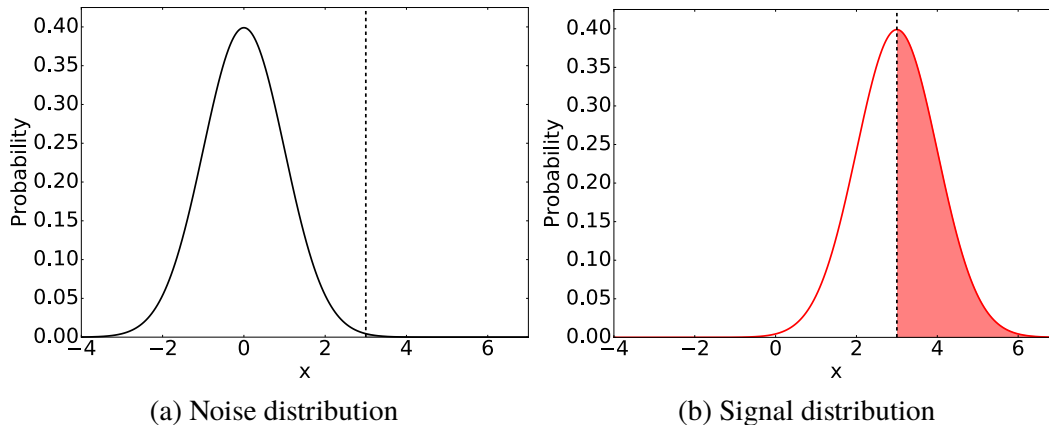


Figure 4.2: (a) The normally distributed PDF of a noise source with a mean of zero and standard deviation of one. Here, the detection criterion is arbitrarily set to 3σ (dashed line), which corresponds to $x = 3$ for this distribution. Because the noise PDF falls above the detection threshold a fraction 0.001 of the time, the false positive fraction in this example is 0.001. (b) The Gaussian PDF of a signal source with a mean of $x = 3$ and a standard deviation of one. Because half of the signal distribution's area falls above the detection criterion, the true positive fraction is 0.5.

The detection criterion therefore allows us to trade between the FPF and TPF, within the constraints imposed by the noise PDF and the signal mean. The receiver operator characteristic (ROC) curve allows us to visualize this trade by plotting the TPF as a function of the FPF, with each parameter varying between 0 and 1 as the detection criterion moves from large to small values (Tanner and J. A. Swets (1954) gives an early example of an ROC curve). The black line in Figure 4.3 shows the ROC curve associated with our example. The (TPF, FPF) pair corresponding to our example criterion of 3σ is labeled, along with a broader range of criteria choices.

The shape of the ROC curve is determined by the shape of the noise distribution as well as the signal mean. For example, if we change the mean of the signal distribution in Figure 4.2b from $x = 3$ to $x = 1$, we obtain the gray ROC curve shown in Figure 4.3. Alternatively, if we had chosen a positively skewed rather than a normal noise distribution, the nearly vertical part of the black ROC curve at small FPFs would tilt to the right.

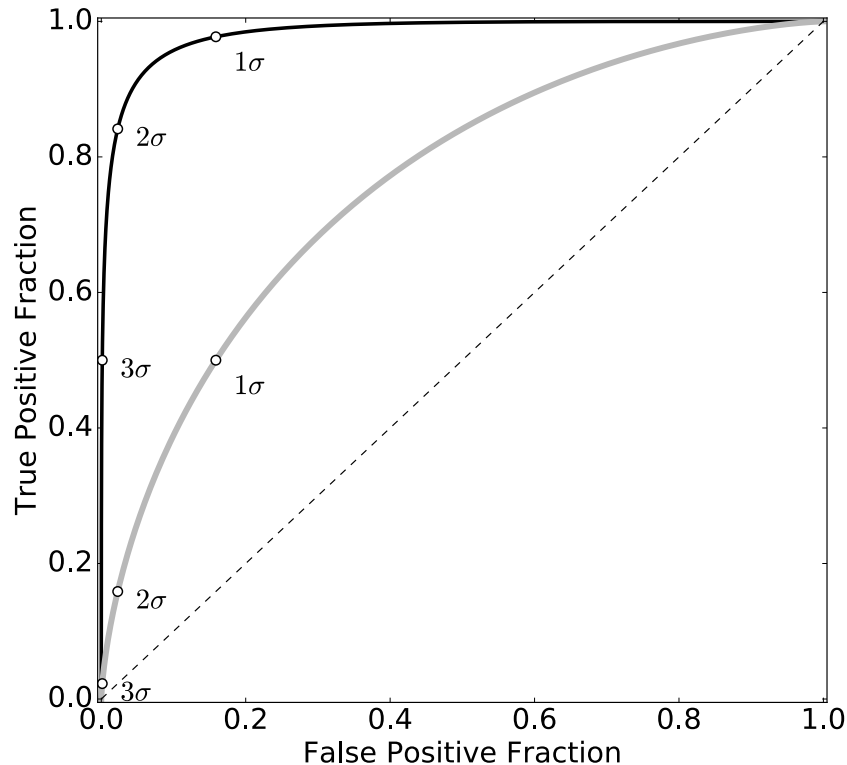


Figure 4.3: Black line: an ROC curve corresponding to a range of criteria applied to the noise and signal distributions in Figure 4.2. The (TPF, FPF) locations corresponding to criteria of $1\sigma - 3\sigma$ are labeled to demonstrate the trade-offs between these key parameters. We note that FPF values larger than 0.5 require a criterion that is less than the mean of the noise distribution. Because the noise is normally distributed in this example, such criteria are negative. Grey line: the equivalent ROC curve for a signal distribution centered at $x = 1$. Because the noise distribution was unchanged, the $1\sigma - 3\sigma$ criterion points are located directly under their equivalent on the black curve.

We may now describe our task as exoplanet imagers in the vocabulary of signal detection theory: we wish to determine the maximum FPF and minimum TPF that satisfy our resource limitations and science goals – in other words, we must choose a target location in (TPF, FPF) space. Our goal in designing an instrument, observing strategy, or post-processing routine is to produce a noise distribution whose ROC curve will reach that location for a signal of interest.

An ROC curve, however, only represents a single noise distribution (i.e. image location) and signal level. In the sections that follow, we will discuss methods for representing the performance of a full image.

4.3 Contrast Curves as Performance Metrics

The Definition of the Contrast Curve

The contrast curve is a means of representing the true and false positive fractions associated with a range of signals and positions in a final image. Schematically, we can define the contrast as:

$$\text{contrast} = \left(\frac{\text{factor} \times \text{noise}}{\text{star photometry}} \right) \left(\frac{1}{\text{throughput}} \right), \quad (4.3)$$

where the numerator is the detection criterion, expressed as a multiple of the noise distribution's width. Typically, we choose the "noise" to be the standard deviation of the counts in a given annulus (e.g. $1 \lambda/D$ thick) centered on the star, and the "factor" to be three or five to produce a 3σ or 5σ contrast curve. In Figure 4.2, factor = 3 and noise = $\sigma = 1$. The detection criterion is then converted from the units of counts to a fraction of the parent star's brightness via the "Star Photometry" term. Finally, the "throughput" term corrects this brightness ratio for any attenuation of the off-axis signal relative to the star's (e.g. due to field-dependent flux losses imposed by the coronagraphic system and post-processing routine). The final contrast is therefore the planet-to-star flux ratio of a planet whose brightness is equal to the detection criterion. Figure 4.2 illustrates that the TPF associated with such a signal is 0.5. Hence, the contrast curve can be interpreted as the signal for which we achieve 50% completeness given our choice of detection criterion in the numerator. The numerator also fixes the false positive fraction – for example, choosing factor= 3 for a white noise distribution gives FPF = 0.001.

Where the Contrast Curve Falls Short

Both practical and fundamental shortcomings, however, undermine the utility of the contrast curve as a general purpose performance metric. First, the contrast is inflexible: by fixing the true positive fraction to 0.5 and the false positive fraction to a value set by the numerator, we cannot explore the (TPF, FPF, detection criterion) trade space. Even if we were to plot multiple contrast curves on the same figure to show different detection criteria, we could not escape the arbitrary choice of TPF= 0.5. Similarly, if we were to plot a 90% detection completeness curve as a function of separation, we could not access a range of false positives fractions.

More problematic, however, is the calculation of the terms in Equation 4.3. As mentioned above, the "noise" term is typically chosen to be the standard deviation of counts in a region of the image, whose shape and size widely varies in the literature. This approach is valid if two conditions are met: 1) if the region includes enough

statistically independent realizations of the noise to allow for an accurate measure of the distribution's standard deviation, and 2) if the underlying noise distribution is Gaussian. While there is no hard and fast rule for deciding whether the first condition is met, statisticians generally consider 30 independent samples to be the boundary between large and small sample statistics (Wilcox, 2009). For the case of $1 \lambda/D$ -wide annular regions, 30 samples corresponds to a separation of $\sim 5\lambda/D$. Below this threshold, the number of independent elements is small enough that a naive computation of their standard deviation leads to extreme underestimates of the false positive fraction (Student, 1908; Mawet et al., 2014). The mitigating strategy proposed by Mawet et al. (2014), however, also requires that condition #2 (Gaussian noise) is met. Aime and R. Soummer (2004) and many others have shown that uncorrected low-order wavefront aberrations cause the noise at small separations to follow a positively skewed modified Rician distribution rather than a normal distribution (M. D. Perrin, Sivaramakrishnan, et al., 2003; Bloemhof, 2004; Fitzgerald and J. R. Graham, 2006; R. Soummer et al., 2007; S. Hinkley, B. R. Oppenheimer, R. Soummer, et al., 2007; C. Marois, D. Lafrenière, B. Macintosh, et al., 2008). While numerous observing and post-processing strategies have been employed to whiten this skewed distribution (e.g. Liu, 2004; C. Marois, D. Lafrenière, R. Doyon, et al., 2006; D. Lafrenière, C. Marois, René Doyon, et al., 2007; Amara and Quanz, 2012; R. Soummer, L. Pueyo, and Larkin, 2012), their success at small separations is limited by the temporal and spectral variability of the noise (Appendix 4.7 discusses the difficulty of testing for normality using methods such as the Shapiro-Wilk test). The result is that the noise distribution at small angles retains an unknown skewness at small separations that increases the false positive fraction compared to a Gaussian distribution. Hence, neither condition for the use of the standard deviation as a proxy for the FPF is met at small separations¹. In Section 4.4 we will address alternative methods for probing the distribution of the noise without the assumption of normality.

Inconsistencies in Contrast Curve Computations

We further note that the contrast and its constituent terms are inconsistently computed in the literature, in particular the noise and throughput terms. While many

¹It is worth noting that some authors interpret the numerator of Equation 4.3 as an empirical signal to noise threshold without reference to the distribution of the noise or a false positive fraction. This interpretation, however, robs the contrast curve of much of its practical use – the knowledge that we can achieve TPF= 0.5 for a given planet:star flux ratio does not guide our observing or science if the associated false positive fraction can fall anywhere from zero to one.

authors (e.g. Wahhaj et al., 2013) account for spatially correlated speckle statistics by defining the noise to be the standard deviation of pixel counts in an annulus, others do not. For example, Otten et al. (2017) define the noise in relation to the standard deviation of pixel counts inside of a $1 \lambda/D$ aperture of interest. The region within a few λ/D of the inner working angle, however, is fundamentally sensitive to azimuthally correlated speckle noise: effects such as pointing jitter, thermal variations, and non-common path aberrations induce low order wavefront aberrations, and hence close-in, variable speckles, on the timescale of an observation (Shi et al., 2016). Secondly, the definition of the term “throughput” is context dependent. Authors computing contrast curves for angular differential imaging (ADI) datasets typically define the throughput in terms of the flux losses imposed by signal self-subtraction (e.g. Wahhaj et al., 2013). However, in discussions of coronagraph design trades, throughput refers to the often field-dependent flux losses caused by the coronagraphic system itself (e.g. Guyon, Pluzhnik, et al., 2006; Krist, Nemati, and B. Mennesson, 2015). Finally, the small sample correction presented by Mawet et al. (2014) has been adopted by some authors (e.g. Wertz et al., 2017), but not others (e.g. Uyama et al., 2017). Such a variety of methodologies inhibit meaningful comparisons of instrument performance.

In this section, we have described three shortcomings of the contrast curve: 1) its inability to illustrate the (TPF, FPF, detection criterion) trade space, 2) its reliance on an estimate of the width of an unknown noise distribution, and 3) its inconsistent treatment in the literature. In the sections that follow, we will discuss strategies for computing the FPFs and TPFs associated with an unknown noise distribution and present a new figure of merit for the performance of high dynamic range imaging systems.

4.4 Estimating the False Positive Fraction at Small Separations

Given our inability to sample the unknown noise distribution at small separations, we choose to proceed by calculating the FPF empirically: for each annulus of interest, we will simply count the number of resolution elements that exceed our detection threshold. Following Mawet et al. (2014), we define a resolution element to be a circular aperture with a diameter of λ/D . The number of resolution elements, N_r , at a distance r from the central star is $2\pi r$, where r is also expressed in terms of λ/D (Figure 4.4). We consider only whole numbers of resolution elements (e.g. six resolution elements at $1\lambda/D$).

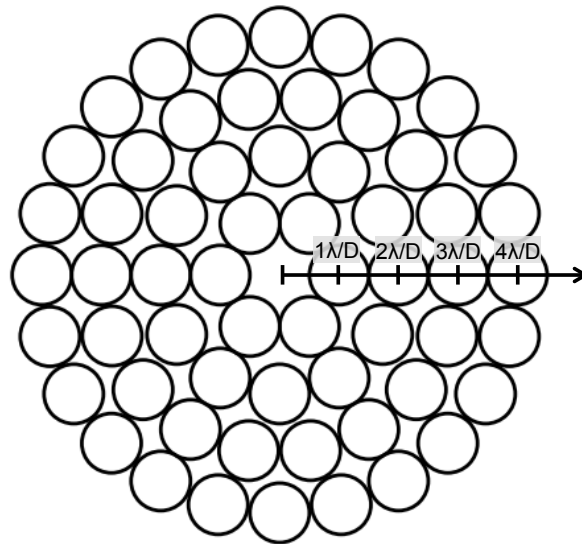


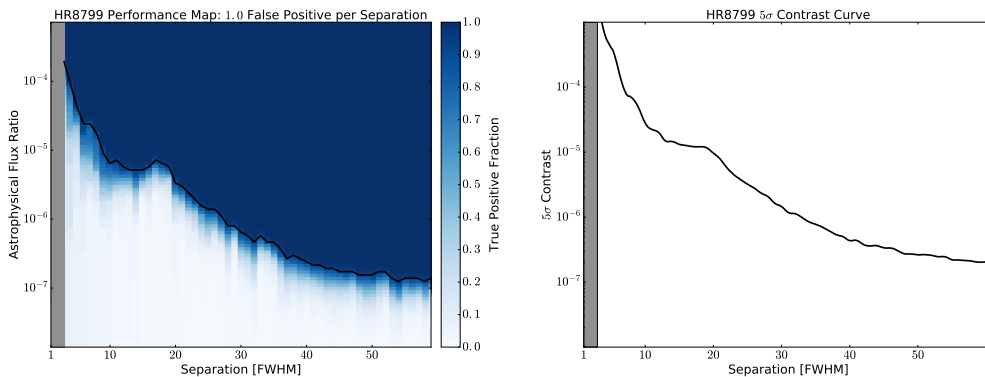
Figure 4.4: The number of resolution elements of width λ/D at a distance r from the central star is $2\pi r$, where here we consider only whole numbers of resolution elements.

For a single $1 \lambda/D$ -thick annulus in the final, post-processed image, the possible values of the empirical false positive fraction are now constrained to i/N_r , where i is an integer between zero and N_r (inclusive). We have two options for accessing FPFs between zero and $1/N_r$: assuming an underlying noise distribution, or obtaining additional realization of the noise. Given the unknown skewness of the data at small separations (Section 4.3), we address the latter choice.

One opportunity for obtaining further realization of the noise is to break up a dataset temporally (i.e. by parallactic angle in the case of ADI data) or by wavelength (in the case of spectral differential imaging data: C. Marois, René Doyon, et al., 2000; Sparks and Ford, 2002) to produce multiple “final” images. Assuming that these additional images give independent realizations of the same underlying noise distributions, we can concatenate the resolution elements at the same separations before calculating the empirical FPF. The least non-zero FPF per r is then $1/(N_r N_f)$, where N_f is the total number of independent final images.

We note that this approach may not be immediately appealing, as breaking up an observing sequence into multiple images necessarily degrades the planet’s SNR: if the original datacube is temporally divided into N_f final frames, the least non-zero FPF is given by $1/N_r N_f$, while the signals’ S/N_{shot} are reduced by $\sqrt{N_f}$ (see the “debinning factor” introduced by Mawet et al., 2014). However, we see only

two alternative approaches to this “break up” strategy. First, data from the same instrument can provide additional resolution elements if the distribution of the noise is assumed to be constant with time. Ruffio et al. 2017, in prep, describe the application of this technique to the Gemini Planet Imager Extra Solar Survey (GPIES) campaign. We view this as the most promising option, but note that it cannot be applied if the historical data has been used to reduce the target of interest via reference star differential imaging. Second, in the case of ADI data, an additional image can be obtained “for free” by reversing the order of the parallactic angle assignments (Wahhaj et al., 2013). This produces an image with similar azimuthal noise characteristics to the science image, giving $N_f = 2$ without dividing the original datacube into two pieces. Further angle randomization, however, will artificially whiten the speckle noise, as it will fail to capture the temporal speckle evolution that de-rotation translates into azimuthal variation.



(a) Performance Map: one false positive per separation

(b) Classic 5σ contrast curve

Figure 4.5: (a) The performance map shows the astrophysical flux ratio versus the separation, color-coded by the true positive fraction. The solid black line represents the approximate $TPF = 0.95$ contour. (b) The classic 5σ contrast curve. The regions interior to the inner working angle of $2\lambda/D$ are shaded in gray. The key difference between the performance map and the contrast curve is that the contrast curve fixes the detection criterion for all separations, while the performance map fixes the number of false positives for all separations. Because the false positive fractions are calculated empirically, we obtain a minimum of one false positive per separation for the case of a single image. In order to access smaller numbers of false positives per separation, we must either break the observation into several final images (Figure 4.6), which sacrifices the sensitivity, or make use of historical data from the same instrument.

Equipped with a strategy for determining an empirical FPF (and, after injecting

artificial companions, an empirical TPF), we return to the challenge of visualizing the five key parameters of exoplanet imaging: the separation from the central star, planet signal, detection criterion, true positive fraction, and false positive fraction.

We propose a new figure, the “performance map,” that represents the performance of an exoplanet imaging system without any assumptions about the distribution of the noise. The performance map plots the astrophysical flux ratios of injected signals as a function of separation, color-coded by the true positive fraction. While the traditional contrast curve keeps the detection criterion constant for all separations, we choose to vary the criterion in order to fix the number of false positives (N_{FP}) per separation, where $N_{\text{FP}}(r) = 2\pi r \times \text{FPF}(r)$. For example, in a performance map representing a single image, we might choose one false positive per separation. This choice sets the FPFs for all separations (FPF= 1/6 at $1\lambda/D$, FPF= 1/12 at $2\lambda/D$, etc), and hence the detection criteria that determine the TPFs. We may also overplot a TPF contour for clarity.

We summarize the key differences between the performance map and the contrast curve below:

1. The contrast curve fixes the detection criterion for all separations, while the performance map fixes the number of false positives for all separations.
2. The contrast curve’s detection criterion (e.g. 5σ or 3σ) refers to the signal-to-noise of a planet, assuming that the noise is Gaussian. In Section 4.3, we argued that such detection criteria choices are not well motivated unless the assumption of Gaussian noise can be rigorously justified. The detection criteria used to generate the performance map, however, have no intrinsic physical meaning – they are simply chosen to produce empirical FPFs and TPFs between zero and one.

The performance map brings our attention back to the scientifically and programmatically relevant quantities: the TPFs of the signals of interest for a given number of false positives. Of course, displaying more information in a single figure is simultaneously a disadvantage if that figure becomes too difficult to interpret at a glance. Including the TPF= 0.95 contour (or other desired TPF value), however, provides a simplified visual summary.

Practical Example: Single Frame

To illustrate the construction of a performance map in detail, we consider a set of HR8799 observations taken by the Spectro-Polarimetric High-contrast Exoplanet REsearch (SPHERE, Beuzit et al., 2008) at the Very Large Telescope (VLT). The data were acquired in December of 2014 during science verification of the Infra-Red Dual-band Imager and Spectrograph (IRDIS, Dohlen et al., 2008) instrument, and have been extensively described in the literature (Zurlo et al., 2016; Apai, Kasper, et al., 2016; Wertz et al., 2017). We adopt a 200 frame broadband H filter ($1.48 - 1.77 \mu\text{m}$) sequence from December 4th 2014, where the detector integration time was 8 s and the total amount of parallactic angle rotation was $8^\circ.7$. We choose to include only the data taken on the left-hand side of the IRDIS detector.

Following Wertz et al. (2017), we use an off-axis broadband H image of β Pictoris (January 30th 2015, PI: A.-M. Lagrange) as our PSF template due to the absence of an off-axis exposure in the original observing sequence. We fit a 2D Gaussian function to the β Pictoris template PSF to obtain $\text{FWHM} = 4.0 \text{ pixels} = 0''.049$ for a plate scale of 12.251 mas (Wertz et al., 2017). We take $\text{FWHM} = 4.0 \text{ pixels}$ as our resolution element diameter.

For the purposes of this demonstration, we are interested in estimating the FPFs and planet-injected TPFs. Hence, we begin our reduction by subtracting HR8799 bcde from the dataset. This is accomplished via the Vortex Image Processing (VIP, Gomez Gonzalez et al., 2016) package’s functions for injecting negative fake companions into the data and optimizing their flux and positions using a Nelder-Mead based minimization.

Next, we use VIP’s implementation of the PCA-ADI algorithm to subtract a reconstructed datacube from our set of 200 images. The reconstructed cube was generated using three principle components (chosen to maximize the SNR of HR8799 c in a full reduction of the dataset prior to planet subtraction). We median-combine the residual datacube to obtain our final reduced image. We compute the algorithmic throughput (signal self-subtraction) as a function of separation by injecting fake planets at separation intervals of 1 FWHM and azimuthal intervals of 120° . For each separation interval, the data is PCA-ADI reduced, and the signals’ flux attenuation in the three azimuthally separated apertures are averaged.

To generate a performance map from this single, “final” image, we first make a list of FPFs for a range of detection criteria and separations by the following recipe:

1. Draw rings of FWHM-diameter apertures around the central star and sum the fluxes inside of the apertures. The result is a list of $2\pi r$ aperture sums for each separation r .
2. Choose a detection criterion.
3. For each separation, find the fraction of resolution elements whose sum exceeds the criterion. These are the FPFs.
4. Vary the detection criterion and repeat Step 3 to produce all possible FPF values for all separations.

Using the same set of detection criteria and separations as the preceding recipe, we can find the associated TPFs for a range of planet signals of interest. This is accomplished by the following steps:

1. Sum the flux inside of a FWHM-diameter aperture around the unocculted stellar PSF².
2. Choose an astrophysical flux ratio and multiply by the star's aperture sum (previous step) to obtain the planet's signal.
3. For each separation, multiply the planet's signal by the algorithmic throughput (previous paragraph), and add the result to each resolution element.
4. Choose a detection criterion from the same list of criteria used to generate the FPFs above.
5. For each separation, find the fraction of resolution elements whose sum exceeds the criterion. These are the TPFs.
6. For the same range of detection criteria used to calculate the FPFs, repeat Step 5.
7. Repeat Steps 2-6 for different astrophysical flux ratios.

²As mentioned above, our example dataset lacks an unocculted image, but we fit the positions and fluxes of the HR8799 planets using a later off-axis observation of β Pictoris. For the purposes of this example, we estimate HR8799's unocculted aperture sum based on the fitted flux of HR8799 b and the H-band planet-to-star flux ratio given in C. Marois, B. Macintosh, et al. (2008).

To plot the performance map, we elect to consider the detection criteria associated with the least non-zero FPFs ($1/N_r$), giving 1.0 false positives per separation. For each injected signal flux at each separation, we then plot the TPFs corresponding to these detection criteria. Figure 4.5a shows the resulting performance map. For each separation, we also plot the signal with the TPF nearest to, but not exceeding, $\text{TPF} = 0.95$, for these detection criteria.

For comparison, we also plot a classic 5σ contrast curve in Figure 4.5b. For each λ/D -width annulus, comprising $2\pi r$ resolution elements, the contrast was calculated via Equation 4.3, where factor=5, σ has been adjusted to account for small sample statistics (Mawet et al., 2014), and the algorithmic throughput was calculated by fake planet injection (see preceding discussion).

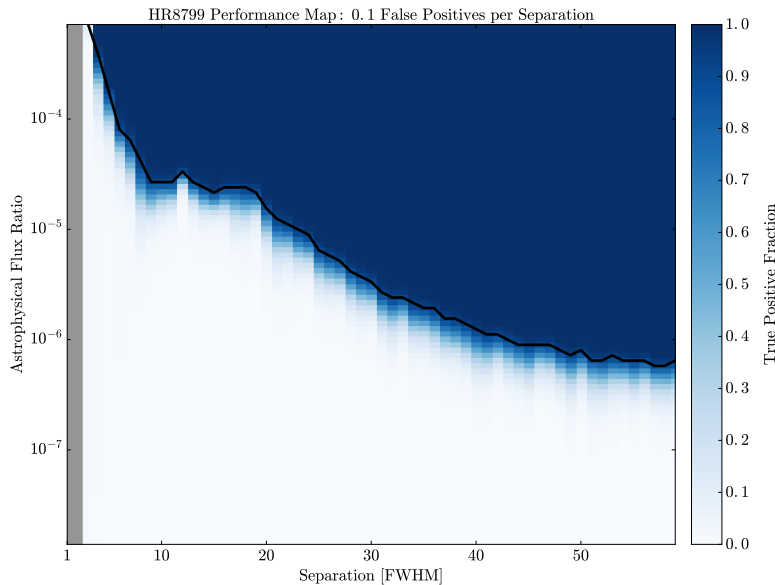


Figure 4.6: A performance map where the detection criteria have been chosen to produce 0.1 false positives per separation. This is achieved by breaking the original 200-frame observation into ten 20-frame observations and appending the resolution elements at each separation. Hence, the number of false positives is reduced at the expense of sensitivity.

Practical Example: Multiple Frames

As discussed in Section 4.4, plotting a performance map representative of fewer than one false positives per separation requires more than one final frame. To demonstrate the trade-offs between the sensitivity and FPF characterization, we divide the PCA-ADI reduced datacube into 10 de-rotated, median-combined final images, each

including 20 individual frames. Because we wish to capture the temporal evolution of the speckle noise over the course of the full observation in each final image, we do not divide the datacube into temporally sequential chunks. Rather, we choose the temporal distance between frames in a given sub-observation to be equal to the total number of sub-observations.

We compute the FPFs and TPFs as before, except that the number of aperture sums per r is $10 \times 2\pi r$ rather than $2\pi r$. The least non-zero FPF is now $(1/N_r N_f)$, giving 0.1 false positives per separation for $N_f = 10$. Figure 4.6 shows the resulting performance map. It is clear that the approximate TPF= 0.95 contour corresponds to brighter planets than was the case in 4.5a – hence, we have traded sensitivity for greater knowledge of the false positive fraction.

We conclude our discussion of the performance map by reiterating its purpose: to represent the performance of a high dynamic range exoplanet imaging system without any assumptions about the distribution of the noise. The examples given in Sections 4.4 - 4.4 are worst case scenarios, in the sense that they deal with only one dataset. Future publications will demonstrate the use of historical data from the same instrument to increase the number of resolution elements without breaking up the dataset of interest.

4.5 Hypothesis Testing

In the discussion above, our calculation of the true and false positive fractions required a choice of hypotheses: either H_1 (signal present; planet-injected data), or H_0 (signal absent; planet-free data). This approach allowed us to characterize the performance of the instrument by probing the range of possible TPFs and FPFs for various positions and signals.

We may also consider a different objective: deciding whether a particular bright spot in our final science image is a planet. In this scenario, we must decide which hypothesis, H_1 or H_0 , applies to our location of interest. While hypothesis testing is beyond the scope of this chapter, we refer to the detailed discussions in N. J. Kasdin and Braems (2006), Section 5, and Young, N. J. Kasdin, and Carlotti (2013).

4.6 Conclusion

As the cost and complexity of ground and space-based exoplanet imaging missions increase, so too must the fidelity and relevance of our diagnostic tools improve. We argue that the drawbacks of the contrast curve – its lack of transparency, flexibility,

and connection to the data – motivate a re-evaluation of its use as a general purpose performance metric. Our proposed “performance map” is one among many possible methods for visualizing the true and false positive fractions associated with a high dynamic range image. The performance map is an opportunity for displaying the results of planet search programs in a consistent and statistically correct way as well as comparing the performance of various post-processing algorithms within a well-defined statistical framework. By encouraging the scrutiny of this new metric, we hope to improve the prediction and evaluation of the performance of the next generation of high contrast imaging instruments.

ACKNOWLEDGMENTS

This work has been supported by the Keck Institute for Space Studies and the NASA Exoplanet Exploration Program Study Analysis Group #19: Exoplanet Imaging Signal Detection Theory and Rigorous Contrast Metrics. This material is based upon work supported by the National Science Foundation Graduate Research Fellowship under grant No. DGE-1144469. G. Ruane is supported by an NSF Astronomy and Astrophysics Postdoctoral Fellowship under award AST-1602444.

4.7 Appendix: The Shapiro-Wilk Test

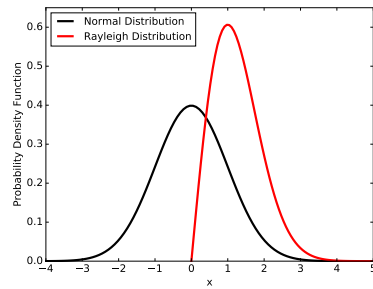
For a given post-processed dataset, we may be interested in testing whether our data has been successfully whitened at small separations. The Shapiro-Wilk test (Shapiro and Wilk, 1965) tests the null hypothesis that a dataset was drawn from a normal distribution; it returns a p -value that specifies that probability of obtaining the dataset given the null hypothesis. In order to test the utility of the Shapiro-Wilk test at small separations, we consider data drawn from two different distributions: a normal distribution (Figure 4.7a, black line), and a positively skewed Rayleigh distribution (Figure 4.7a, red line). At face value, we expect to easily reject the Shapiro-Wilk test's null hypothesis when testing data drawn from the dramatically non-white Rayleigh distribution.

We first compute the Shapiro-Wilk test p -value using a normally distributed dataset with $2\pi r$ elements. We then draw new sets of $2\pi r$ elements to repeat the test 10^4 times, giving 10^4 p -values per separation. We arbitrarily choose $p \leq 0.01$ as our criterion for rejecting the null hypothesis. As expected, we find that for all separations, the normally distributed test data gives $p \leq 0.01$ a fraction 0.01 of the time (Figure 4.7b, black points).

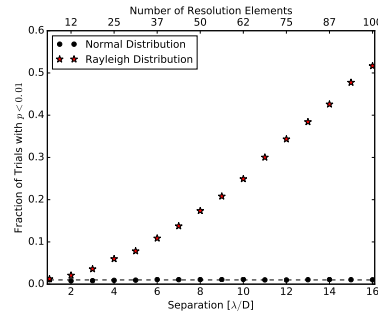
Next, we repeat this procedure for the Rayleigh distributed data. We find that these data reject the null hypothesis for a much larger fraction of trials than the normally distributed data (Figure 4.7b, red points). However, we quickly see a problem: at $15\lambda/D$, the Rayleigh distributed data only rejects the null hypothesis about half of the time. This means that in any one science image, the probability of erroneously accepting the null hypothesis that the data is normally distributed is also 50%. At smaller separations, we draw the wrong conclusion most of the time – hence, the Shapiro-Wilk test cannot be used to test for normality at small separations.

Some tests (e.g. the Kolmogorov-Smirnov test) perform better in these respects than

the Shapiro-Wilk test, while others (e.g. the Anderson-Darling test) are similarly problematic. The purpose of the example given here is to demonstrate that the outcomes of normality tests cannot be taken at face value, and must be rigorously validated in order to be applied to observational datasets.



(a) The PDF of a normal distribution (black line) and Rayleigh distribution (red line) with a scale parameter of two.



(b) The fraction of all trials that reject the null hypothesis ($p \leq 0.01$) for the normally distributed data (black circles) and Rayleigh distributed data (red stars). The black dotted line indicates the expected fraction of trials for which the normally distributed data is expected to reject the null hypothesis ($p = 0.01$).

Figure 4.7: Even though the Rayleigh distribution (scale parameter = 2) is highly skewed compared with the normal distribution, the Shapiro-Wilk test cannot reliably distinguish it from a normal distribution for the sample sizes shown here. For separations less than $15 \lambda/D$, the Shapiro-Wilk test gives the wrong outcome (fails to reject the null hypothesis) for more than half of all trials.

Chapter 5

THE PERFORMANCE OF THE ROBO-AO LASER GUIDE STAR
ADAPTIVE OPTICS SYSTEM AT THE KITT PEAK 2.1-M
TELESCOPE

ABSTRACT

Robo-AO is an autonomous laser guide star adaptive optics system recently commissioned at the Kitt Peak 2.1-m telescope. Now operating every clear night, Robo-AO at the 2.1-m telescope is the first dedicated adaptive optics observatory. This chapter presents the imaging performance of the adaptive optics system in its first eighteen months of operations. For a median seeing value of $1.31''$, the average Strehl ratio is 4% in the i' band. After post-processing, the contrast ratio under sub-arcsecond seeing for a $2 \leq i' \leq 16$ primary star is five and seven magnitudes at radial offsets of $0.5''$ and $1.0''$, respectively. The data processing and archiving pipelines run automatically at the end of each night. The first stage of the processing pipeline shifts and adds the data using techniques alternately optimized for stars with high and low SNRs. The second "high contrast" stage of the pipeline is eponymously well suited to finding faint stellar companions.

5.1 Introduction

Adaptive optics (AO) systems correct wavefront aberrations introduced by the atmosphere and instrumental optics, restoring the resolution of a telescope to the diffraction limit. Laser guide stars (LGS) were developed in the 1980s to provide AO systems with bright, locatable wavefront reference sources, bringing fainter astrophysical objects into the purview of adaptive optics. Over half of all >8-m aperture telescopes are now equipped with an LGS AO system. The primary application of these AO instruments is for high angular resolution studies of interesting astronomical objects. As such minimizing the overhead has not been a major consideration in the overall design of AO systems on large telescopes.

Robo-AO is a robotic LGS AO system designed for maximum target throughput. Unlike LGS systems on large telescopes, it is based on an artificial star produced by Rayleigh scattering of a near UV laser. Robo-AO achieves high target throughput by minimizing overhead times to less than one minute per target. This is accomplished by three key design elements: 1) each step of the observation sequence is automated, allowing tasks that would be performed sequentially by a human operator to be performed in parallel and with minimal delay by the robotic system; 2) the $\lambda = 355$ nm Rayleigh scattering laser guide star is invisible to the human eye. As a result, while coordination with the U.S. Air Force Joint Space Operations Center (JSpOC) is still required to prevent illumination of sensitive space assets, no control measures are required by the Federal Aviation Administration; 3) Robo-AO employs an automated queue scheduler which chooses each new science target based on telescope slew times and approved lasing windows provided in advance by JSpOC.

Robo-AO was first commissioned at the Palomar 1.5-m telescope in 2011, where it completed 19 science runs as a PI instrument from May 2012 through June 2015. Full details of the Robo-AO hardware and software can be found in Christoph Baranec, R. Riddle, N. M. Law, A.N. Ramaprakash, et al. (2013), Christoph Baranec, R. Riddle, N. M. Law, A. N. Ramaprakash, et al. (2014) and R. L. Riddle et al. (2014).

In 2012, the National Optical Astronomy Observatory (NOAO), following the recommendation of the Portfolio Committee which was chartered by the the National Science Foundation (NSF), decided to divest the Kitt Peak 2.1-m telescope. In 2015, the Robo-AO team made a bid for the telescope and was selected to operate the telescope for three years. Robo-AO was installed at the 2.1-m telescope in November, 2015; since then it has been operating nearly every clear night. As the first dedicated, automated adaptive optics facility, Robo-AO at Kitt Peak is well

Telescope	Kitt Peak 2.1-m telescope
Science camera	Andor iXon DU-888
EMCCD detector	E2V CCD201-20
Read-noise (without EM gain)	$47 e^-$
EM gain, selectable	300, 200, 100, 50, 25
Effective read-noise	0.16, 0.24, 0.48, 0.96, $1.9 e^-$
Full-frame-transfer readout	8.6 frames per second
Detector format	1024^2 13- μm pixels
Field of view	$36'' \times 36''$
Pixel scale	35.1 milli-arcsec per pixel
Observing filters	$g', r', i', z', \text{lp600}$

Table 5.1: The Specifications of the Robo-AO Optical Detector at Kitt Peak.

positioned to support the next generation of large-scale survey programs that are focused on stellar and exoplanet astronomy (e.g. K2, GAIA, CRTS, PTF, TESS and others), as well as AO follow up of interesting sources. Early science results including Robo-AO KP data can be found in Adams et al. (2017) and Vanderburg, Becker, et al. (2016) and Vanderburg, Bieryla, et al. (2016).

In this chapter, we describe the performance of Robo-AO since commissioning. The chapter is organized as follows: §5.2 introduces the Robo-AO imaging systems; §5.3 provides an overview of our automatic data reduction pipelines; §5.4 shows the relationships between the weather conditions and the measured seeing; §5.5 presents the Strehl ratio and contrast curve statistics as well as the point spread function (PSF) morphology; §5.6 describes our automated data archiving system; finally, §5.7 describes the newly installed near-IR camera.

5.2 Summary of the Robo-AO Imaging System

The Robo-AO imaging system includes two optical relays, each using a pair of off-axis parabolic mirrors. The first relay images the telescope pupil onto a 140-actuator Boston Micromachines micro-electro-mechanical-systems (MEMS) deformable mirror used for wavefront correction. A dichroic then reflects the UV light to an 11×11 Shack-Hartmann wavefront sensor. The second optical relay includes a fast tip-tilt correcting mirror and an atmospheric dispersion corrector (ADC; here, two rotating prisms¹) located at a reimaged pupil. The output of the

¹From the commissioning of Robo-AO at Kitt Peak in November of 2015 through February of 2017, the right ascension (RA) axis of the 2.1-m telescope suffered from a ~ 3.7 Hz jitter (see §5.5 and §5.9) that caused a slight elongation of the stellar PSFs. As a result, the ADCs were not correctly calibrated until an upgrade to the telescope control system removed the jitter.

second relay is an F/41 beam that is intercepted by a dichroic mirror, which reflects the $\lambda < 950$ nm portion of the converging beam to the visible wavelength filter wheel and EMCCD detector (see Table 5.1). The filter wheel includes g' , r' , i' , and z' filters, as well as a long-pass “lp600” filter cutting on at 600 nm and extending beyond the red limit of the EMCCD (see Figure 1 in Christoph Baranec, R. Riddle, N. M. Law, A. N. Ramaprakash, et al. 2014). The dichroic transmits the longer wavelength light to the near-infrared (NIR) instrument port (see §5.7).

Robo-AO was originally designed for simultaneous optical and NIR operations, such that deep science integrations could be obtained in one band while the image displacement could be measured in the other and corrected with the fast tip-tilt mirror. In February of 2017, we achieved first light with a science-grade novel infrared array, a brief summary of which appears in §5.7². In this chapter, we consider the imaging performance of Robo-AO using the optical imaging camera only. In lieu of an active tip-tilt correction, the EMCCD is run at a framerate of 8.6 Hz to allow for post-facto image registration followed by stacking (see §5.3).

5.3 Data Reduction Pipelines

Overview

Image registration and stacking (see §5.2) is accomplished automatically by the “bright star” and “faint star” pipelines, which are optimized for high and low signal-to-noise (SNR) targets, respectively. The data are then processed by the “high contrast” pipeline to maximize the sensitivity to faint companions. These pipelines are described in detail below.

Image Registration Pipelines

All observations are initially processed by the “bright star” pipeline. This pipeline generates a windowed datacube centered on an automatically selected guide star. The windowed region is bi-cubically up-sampled and cross correlated with the theoretical point spread function to give the center coordinates of the guide star’s PSF in each frame. The full-frame, unprocessed images are then calibrated using the nightly darks and dome flats. Finally, the calibrated full frames are aligned using the center coordinates identified by the up-sampled, windowed frames, and co-added via the Drizzle algorithm (Fruchter and Hook, 2002). These steps are described in detail in N. M. Law, C. Baranec, and R. L. Riddle (2014).

²A detailed analysis of the operation of this camera, its imaging performance, and its incorporation into an active tip-tilt control loop will be reported elsewhere.

After an observation has been processed by the “bright star” pipeline, the core of the brightest star in the frame is fit by a 2D Moffat function. If the full width at half maximum (FWHM) of the function fit to the core is $< \lambda/D$, indicating that the stellar centroiding step has failed, the observation is re-processed by the “faint star” pipeline to improve the SNR in the final science image.

The individual frames for a given observation are summed to create a master dark-and-flat-corrected reference image. This frame is then high pass filtered and windowed about the guide star. Each raw short exposure frame is then dark and flat corrected, filtered, and windowed. These individual frames are registered to the master reference frame using the `Image Registration for Astronomy` python package written by Adam Ginsburg³. The package finds the offset between the individual and reference frames using DFT up-sampling and registers the images with FFT-based sub-pixel image shifts. Figure 5.1 illustrates the strengths and weaknesses of the bright and faint star pipelines.

These automatic pipelines have reduced thousands of Robo-AO observations since the instrument was commissioned in November of 2015. Figure 5.2 shows a collage of representative observations.

High Contrast Pipeline

For science programs that aim to identify point sources at small angular separations from known stars further processing is needed. Our “high contrast imaging” pipeline generates a 3.5” frame windowed about the star of interest in the final science frame. A high pass filter is applied to the windowed frame to reduce the contribution of the stellar halo. To whiten correlated speckle noise at small angular separations from the target star we subtract a synthetic PSF generated by Karhunen-Loève Image Processing (KLIP). The KLIP algorithm is based on the method of Principal Component Analysis (R. Soummer, L. Pueyo, and Larkin, 2012). The PSF diversity needed to create this synthetic image is provided by a reference library of Robo-AO observations – a technique called Reference star Differential Imaging (RDI; D. Lafrenière, C. Marois, Rene Doyon, et al., 2009). We note that the angular differential imaging approach (C. Marois, D. Lafrenière, R. Doyon, et al., 2006) is not possible here because the 2.1-m telescope is an equatorial mount telescope. Our pipeline uses the `Vortex Image Processing (VIP)` package (Gomez Gonzalez et al., 2016).

³https://github.com/keflavich/image_registration

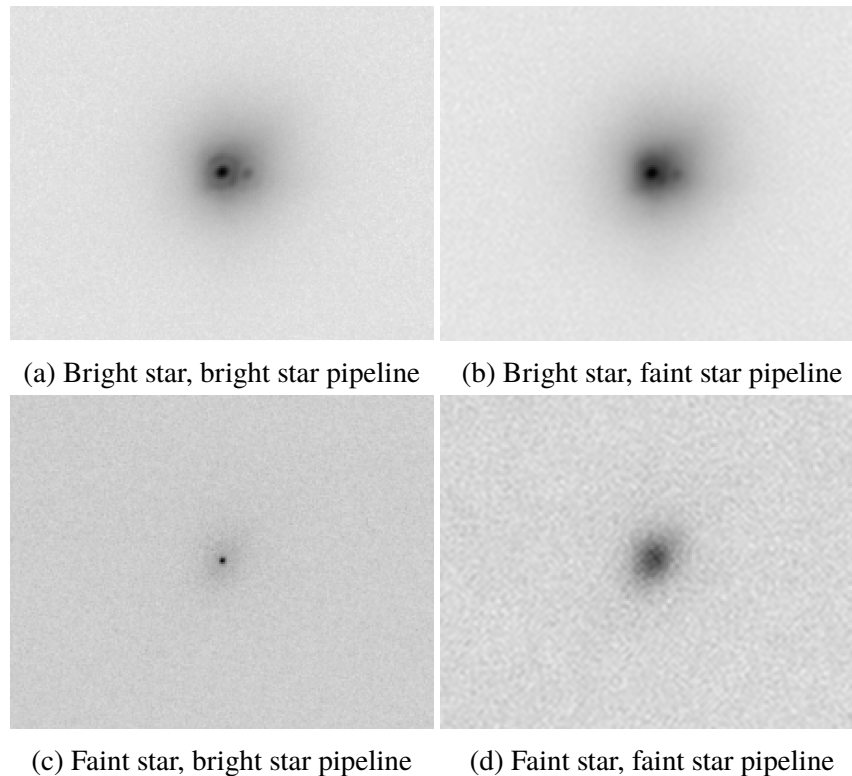


Figure 5.1: The bright star pipeline (a) produces a superior Strehl ratio for the $V= 8.84$ double star HIP55872 compared with (b) the faint star pipeline. For the $V= 15.9$ star 2MASSJ1701+2621, however, the bright star pipeline (c) fails to correctly center the PSF, leading to an erroneously bright pixel in the center. The faint pipeline (d) successfully shifts and adds this observation.

The full reference PSF library consists of several thousand $3.5''$ square high pass filtered frames that have been visually vetted to reject fields with more than one point source. The PSF library is updated on a nightly basis to ensure that each object's reduction has the opportunity to include frames from the same night. Each frame in the full library is cross correlated with the windowed and filtered science frame of interest. The five frames with the highest cross correlation form the sub-library provided to KLIP. We then adopt only the first principal component (PC) as our synthetic PSF, as including more PCs provides no additional noise reduction on average. A future version of the pipeline will choose the number of PCs automatically for each observation based on SNR maximization.

Figure 5.3 shows an example of a PSF reduced by the standard data pipeline (panel a), then high pass filtered (panel b), and finally processed with RDI-KLIP (panel c). After a science frame has been fully reduced we use VIP to produce a contrast curve that is properly corrected for small sample statistics and algorithmic throughput

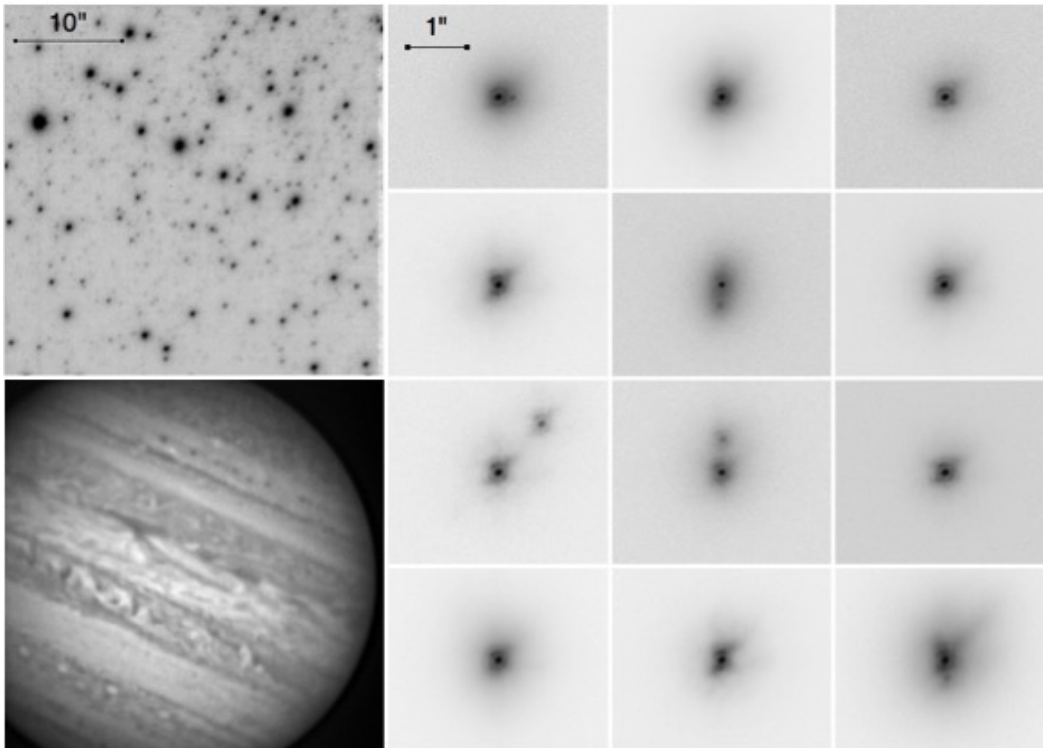


Figure 5.2: Examples of Robo-AO i' -band images at Kitt Peak (square root scaling). The full-frame ($36'' \times 36''$) images on the left are the globular cluster Messier 5 (top) and Jupiter (bottom). The images on the right are examples of bright single stars and stellar binaries with a range of separations and contrasts.

losses. The corresponding contrast curves for the three panels are shown in panel d.

Given that over two hundred new targets are observed during a clear night of Robo-AO observations the reference library is rapidly expanding and increasingly includes PSFs affected by a very wide range of environmental conditions. Hence, speckle noise in a past observation can be further reduced by a fresh RDI-KLIP reduction if the data is more correlated with later PSFs. Clearly a new reduction will benefit from the advantage of the larger reference library.

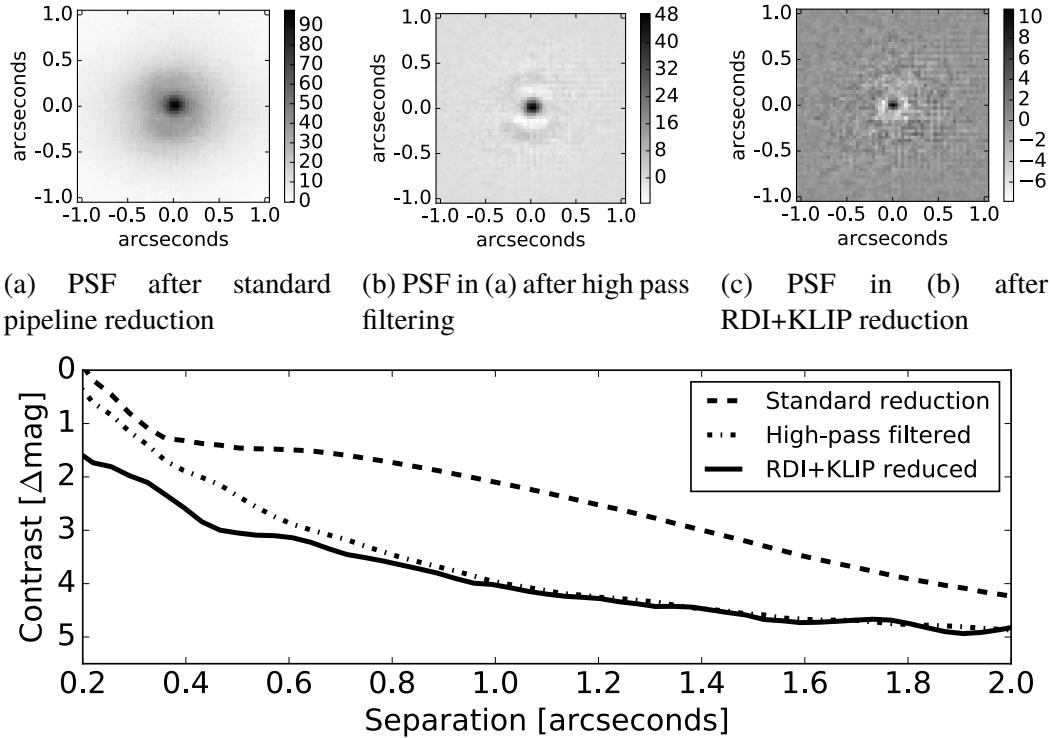


Figure 5.3: An example of the reduction steps in the “high contrast” pipeline for a z' observation of the star EPIC228859428.

5.4 Site Performance

Site Geography

Kitt Peak is located 56 miles southwest of Tucson, Arizona, at an elevation of 6800 feet. The 2.1-m telescope is situated 0.4 miles to the south of the peak’s highest point (the location of the Mayall 4-m telescope). The WIYN 3.5-m and 0.9-m telescopes are respectively 700 ft and 400 ft to the west of the 2.1-m telescope and at approximately the same elevation. There are no structures at equal or greater elevations to the east of the telescope, and the terrain is relatively flat beyond Kitt Peak in that direction. The 7730 ft Baboquivari Peak is 12 miles directly south of the telescope.

Seeing Measurement

Before the start of each science observation, a 10 s seeing observation is taken with the AO correction off. During this period the wavefront sensor camera acquires a background image. These seeing observations are dark and flat calibrated and

summed without any registration of the individual exposures. The seeing is defined as the FWHM of a two-dimensional Gaussian function fit to this summed frame. Starting in January of 2017, a 90 s seeing observation was obtained each hour. Specifically, the Robo-AO queue schedules an observation of a bright ($V < 8$) star within 10° of zenith to refocus the telescope and measure the seeing. As of this writing, there is no significant difference between these “long” and “short” seeing observations. Here on we proceed with the assumption that the 10 s seeing measurements are representative of the long-exposure seeing.

We display a histogram of these fiducial seeing values in Figure 6.2c. Figure 5.4 displays the seeing as a function of the seasons. The seeing values measured in a given wavelength are scaled to a fiduciary wavelength of 500 nm by the scaling law $\text{seeing}_{500\text{ nm}} = \text{seeing}_\lambda \times (\lambda/500\text{ nm})^{1/5}$.

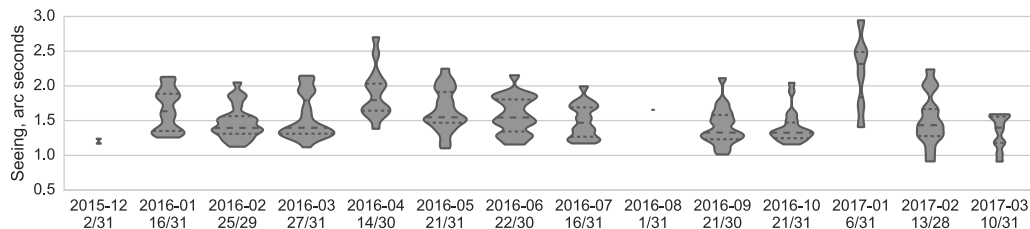


Figure 5.4: Seasonal fiducial ($\lambda = 500\text{ nm}$; see §5.4) seeing measurements. Nightly median values were used to fit a monthly distribution. The fraction of nights with seeing data for each month is shown. The quartile values and the actual measured range are shown.

Seeing Contributions

We note that our median seeing of $1.31''$ differs from the median seeing of $0.8''$ reported by the adjacent WIYN telescope⁴. One possible explanation for this discrepancy is that the WIYN was built in 1994 with careful attention paid to dome ventilation and telescope thermal inertia. In contrast, the 2.1-m telescope saw first light in 1964 before such considerations were fully appreciated. Figure 5.6 demonstrates the challenging thermal conditions at the 2.1-m telescope: during the majority of Robo-AO observations, the mirror is warmer than the ambient dome temperature which in turn is warmer than the outside air. The experience of other observatories indicates that improvements to dome thermalization can significantly improve the measured seeing (e.g. Bauman et al., 2014).

⁴<https://www.noao.edu/wiyn/aowiyn/>

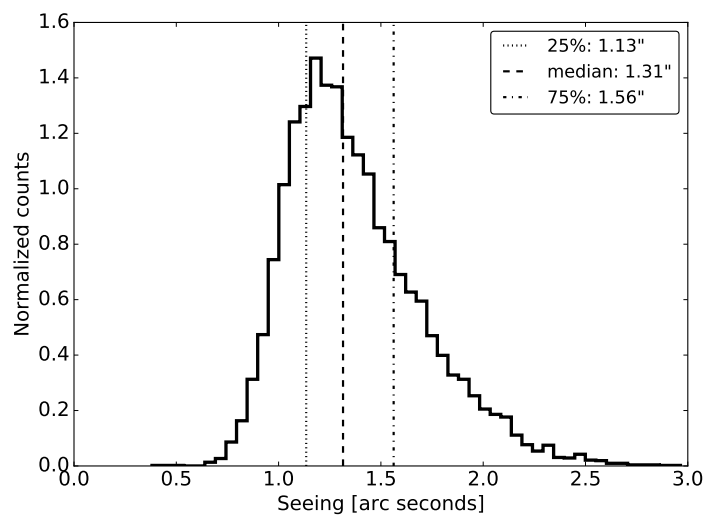


Figure 5.5: A histogram of the seeing measurements (all referenced to a wavelength $\lambda = 500$ nm) from December 2015 to March 2017. A zenith distance dependent correction has been applied. The 25th, 50th, and 75th percentile seeing values are indicated by the vertical lines.

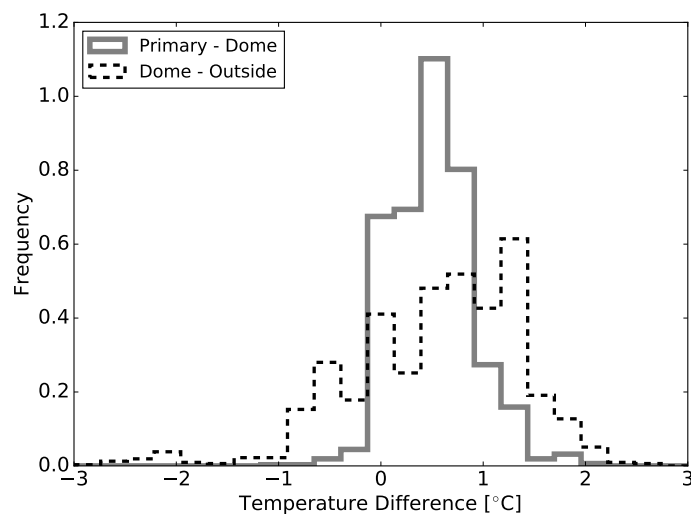


Figure 5.6: Histograms of the difference between the primary mirror and dome temperatures (solid) and the dome temperature minus the outside air temperature (dashed).

Another possible cause of the comparatively poor seeing at the 2.1-m telescope is perhaps a more turbulent ground layer. Figure 5.7 shows a “wind rose,” or the frequency of wind speeds originating from different directions, for December 2015 through June 2016. We find that during this period the wind most commonly

blows from the NNW, or the direction of the higher elevation Mayall 4-m telescope, and rarely from the SE where the terrain is less mountainous. The highest winds (> 40 mph) come from the north while the south has the largest fraction of low wind speeds (the wind speeds originating from within 20° of due south are under 10 mph 73% of the time).

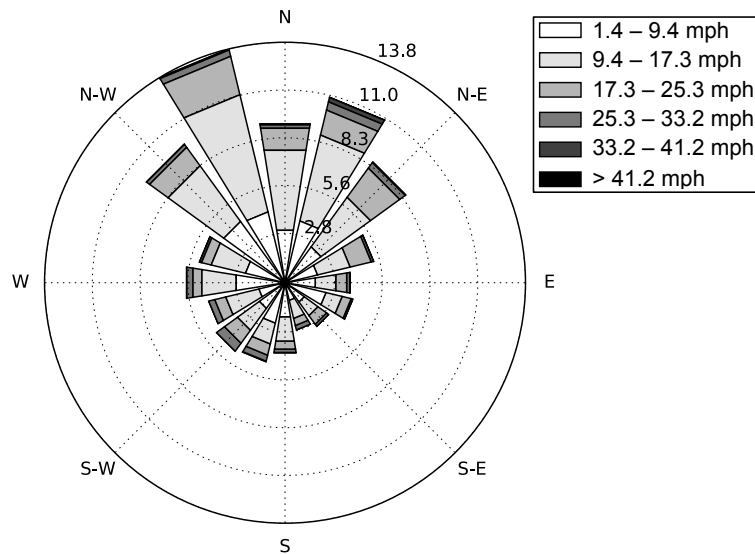


Figure 5.7: A “wind rose” showing a stacked polar histogram of wind speeds and directions from December 2015 through June 2016. The wind most frequently blows from the NW, N, and NE, which correspond to the more mountainous region towards the direction of the Mayall 4-m telescope. These also tend to be the direction of the high wind speeds while slower wind speeds most often come from the south, where the terrain is less mountainous.

Despite these terrain variations, the seeing is not significantly correlated with the wind direction. The wind speed, however, degrades the seeing by several tenths of an arcsecond for winds over 20 mph (the dome closes for winds over 40 mph).

Figure 5.8 plots the seeing versus the wind speed, demonstrating that poorer seeing is correlated with higher wind speeds⁵. We note that the wind monitor became nonfunctional after June of 2016, and hence further study of the relationship between the seeing and the wind speed will occur after a new wind monitor is in place.

⁵The mean binned seeing measurements in Figure 5.8 are larger than the median of all Robo-AO KP seeing measurements (Figure 6.2c) due to binning effects and the difference between the mean and median of the asymmetric distribution of seeing measurements.

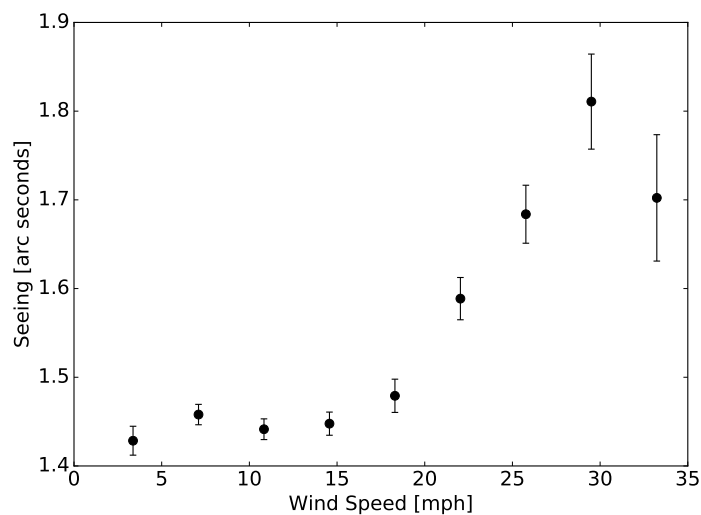


Figure 5.8: The mean binned seeing versus the wind speed for December 2015 through June 2016. The error bars are the standard deviation of the seeing values in a given wind speed bin divided by the square root of the number of seeing measurements in the bin. For wind speeds over 20 mph, the seeing is degraded by up to $0.3''$.

5.5 Adaptive Optics Performance

Strehl Ratio

The goal of an adaptive optics system is to bring the observed PSF closer to its theoretical diffraction-limited shape; hence, an important measure of the AO system's performance is the ratio between the peak intensity of an observed PSF and that of the telescope's theoretical PSF – the Strehl ratio. As the AO performance improves, the Strehl ratio increases.

We calculate the Strehl ratio by 1) generating a monochromatic diffraction-limited PSF by Fourier transforming an oversampled image of the pupil, 2) combining several monochromatic PSFs to create a PSF representative of the desired bandpass, 3) re-sampling the polychromatic PSF to match our $0.0175''/\text{pixel}$ platescale of the up-sampled “drizzled” frames, 4) obtaining the “Strehl factor,” or the ratio of the peak intensity to the sum of the intensity in a $3''$ square box, and 5) calculating the Strehl ratio by repeating step 4 for the observed image and dividing by the Strehl factor. These steps are described in detail in Salama et al. (2016).

Once Robo-AO began regular observations at the 2.1-m telescope, we noticed that the achieved Strehl ratios were noticeably smaller than those that were achieved (for similar seeing values) at the Palomar 1.5-m telescope. A number of exercises

were undertaken to determine possible causes for this degradation. Eventually, we determined that the Telescope Control System (TCS) was the main contributing factor. In Appendix 5.9 we discuss the problem in detail. The mitigation consisted of upgrading the TCS (completed February 2017). Below, and for the rest of the chapter, we discuss the instrument performance since the TCS upgrade.

Figure 5.9 plots the Strehl ratio versus the measured seeing for the i' and lp600 filters. It is clear that the delivered Strehl ratio drops off quickly as the seeing increases – while Robo-AO achieves $> 10\%$ Strehl ratio when the seeing is $< 1.0''$, a $0.25''$ seeing increase halves the Strehl ratio.

In Table 5.2 we present a detailed error budget under different seeing conditions. This error budget was originally developed by R. Dekany (private communication), and was validated against the on-sky performance of laser AO systems on the Keck telescope, the Hale telescope and the Palomar 1.5-m telescope (C. Baranec et al., 2012). Since we lacked turbulence profile(s) for the 2.1-m telescope site we adopt a mean $C_n^2(h)$ profile from a MASS-DIMM atmospheric turbulence monitor collected over a year's baseline at Palomar and scaled to the seeing at Kitt Peak.

High-order errors are added in quadrature and are dominated by focal anisoplanatism (which is an error arising from the finite altitude of the Rayleigh laser guide star resulting in imperfect atmospheric sampling). We estimate one-axis tip-tilt errors as being dominated by bandwidth error for magnitudes greater than 13. As noted in §5.2 we did not use the built-in tip-tilt facility but instead resorted to shift and add. We approximate the error resulting from this approach as follows. We assume a standard -3db rejection frequency matching the full-frame rate of the science camera to approximate bandwidth error. The tip-tilt errors are then converted to an equivalent wavefront error and summed in quadrature with the high-order errors. Other high-order and tip-tilt errors include chromatic, scintillation, aliasing, calibration and digitization errors.

Strehl ratios are calculated using the Maréchal approximation. The full-widths at half-maximum (FWHM) are calculated from PSF models assuming the residual diffraction-limited, concentrated light, residual seeing, and scattered light halos are proportional to the phase variance of the residual errors. These models have shown accuracy of a few percent for Strehl ratios as low as 4% (Sheehy, McCrady, and J. R. Graham, 2006). Figure 5.9 demonstrates Robo-AO's ability to approach the predicted Strehl ratio of 14% in sub-arcsecond seeing conditions.

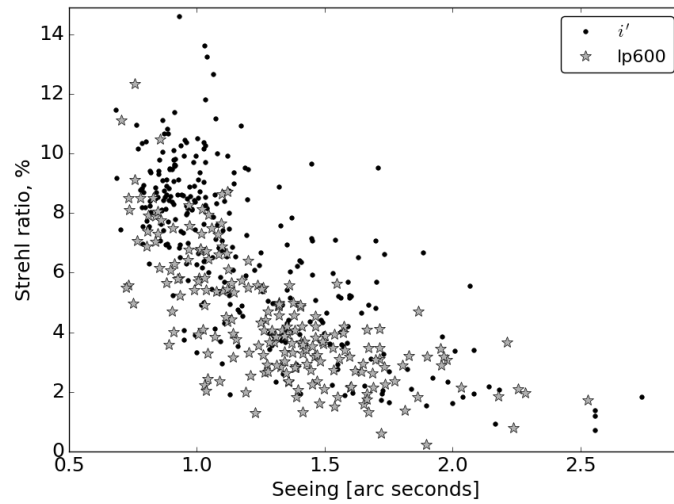


Figure 5.9: The Strehl ratio versus the measured seeing values for 21 February 2017 through 10 March 2017 in the i' and lp600 filters.

PSF Morphology

Figure 5.10 shows a representative Robo-AO point spread function (PSF) corresponding to the $V=10$ star HIP56051. The observation was taken in the i' band with a total exposure time of 90 s. The seeing at the time of the observation was $0.94''$, and the Strehl ratio of the final PSF is 10.17%.

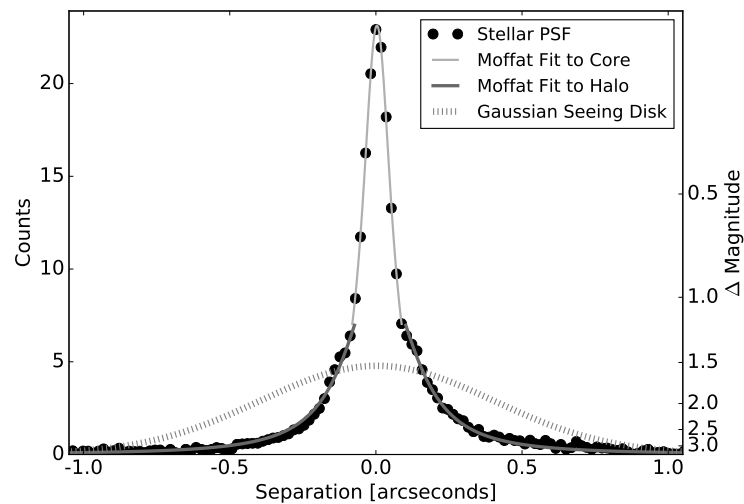


Figure 5.10: A 1D cut through the PSF of HIP56051 is plotted with two Moffat functions fit to the PSF core and halo, respectively. The dashed curve is a Gaussian distribution with a FWHM corresponding to the seeing measurement and an area equal to the observed PSF's area.

Table 5.2: The Robo-AO Error Budget

Percentile Seeing		25%	50%	75%						
Seeing at Zenith	1.00''	1.13''	1.31''	1.56''						
Zenith Angle	20	20	20	20						
Effective Seeing	1.04''	1.17''	1.36''	1.62''						
High-order Errors										
Atmospheric Fitting Error	65	72	82	95						
Bandwidth Error	54	60	67	78						
High-order Meas. Error	35	38	44	52						
LGS Focal Anisop. Error	99	109	124	143						
Other High Order Errors	64	65	68	72						
Total High Order Wavefront Error	149 nm	163 nm	182 nm	208 nm						
Tip-Tilt Errors										
Tilt Bandwidth Error	24 mas	26 mas	30 mas	34 mas						
Other Tip-Tilt Errors	7 mas	7 mas	7 mas	8 mas						
Total Tip/Tilt Error (one-axis)	25 mas	27 mas	31 mas	35 mas						
Total Effective Wavefront Error	165 nm	180 nm	200 nm	228 nm						
Spectral Band	λ	λ/D	Strehl	FWHM	Strehl	FWHM	Strehl	FWHM	Strehl	FWHM
<i>r'</i>	0.62 μ	0.07''	6%	0.10''	4%	0.11''	2%	0.14''	0%	0.34''
<i>i'</i>	0.75 μ	0.08''	14%	0.11''	10%	0.11''	6%	0.12''	2%	0.15''
<i>z'</i>	0.88 μ	0.10''	25%	0.12''	19%	0.12''	13%	0.13''	7%	0.14''
J	1.25 μ	0.14''	49%	0.15''	43%	0.16''	35%	0.16''	26%	0.17''
H	1.64 μ	0.18''	66%	0.19''	61%	0.20''	54%	0.20''	45%	0.20''

The effect of the AO system is to re-arrange the starlight from the equivalent area seeing-limited PSF (dashed curve) to the sharper, observed PSF plotted by the black points. The AO-corrected PSF includes two components: a sharp core and a broader halo, each separately fit by Moffat functions (the light and dark gray curves, respectively). The full width at half maximum (FWHM) of the Moffat function fit to the core is $0.1'' \pm 0.01''$. This value is consistent with the diffraction limit of $1.028 \lambda/D = 0.08''$.

Contrast Curves

Section §5.3 described the “high contrast pipeline,” which produces 5σ contrast curves from the high pass filtered, RDI-PCA reduced science frames. Figure 5.11 plots the median and best 10% contrast curves for *i'* and lp600 filter science frames. Under sub-arcsecond seeing (the best 10% of cases), the contrast ratios for a $2 \leq i' \leq 16$ primary star are five and seven magnitudes at $0.5''$ and $1.0''$, respectively.

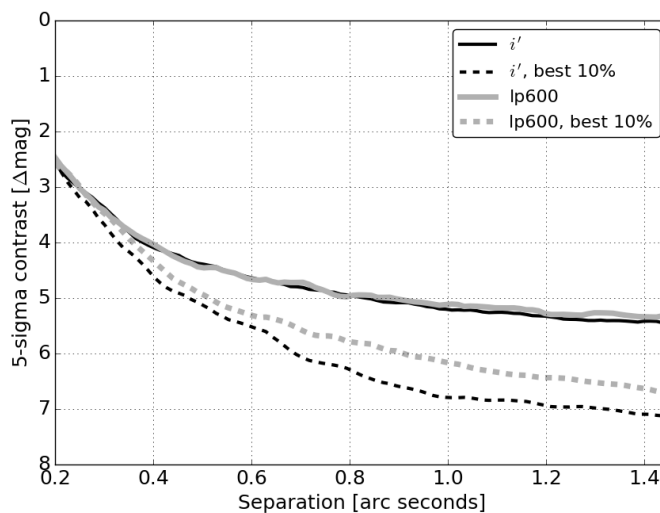


Figure 5.11: The contrast as a function of distance from the central star for the i' and lp600 filters. The dashed lines show the best 10% contrast curves for each filter.

5.6 Data Archive

We have developed a fully automated data processing and archiving system⁶. The data reduction chain for an observing night proceeds as follows. At the end of each night, the visual camera data are compressed and transferred to the network storage. Next, the darks and dome flats taken at the beginning of each night are combined into master calibration files and applied to the observations. The bright star pipeline is then run on each observation followed by the computation of the Strehl ratio of the resulting image. The high contrast pipeline also produces high pass filtered, PSF-subtracted images and contrast curves for each of these processed images (see Section 5.3). If the “drizzled” image produced by the bright star pipeline does not pass a quality check (i.e. if a 2-component Moffat fit to the PSF has an anomalously narrow core or wide halo) then the faint star pipeline re-reduces the rapid readout data. Additionally, the “archiver” processes the nightly seeing data, and generates summary plots of the seeing measurements, Strehl ratios, and contrast curves. Completing the full reduction chain for a typical night’s worth of data takes a few hours.

The “house-keeping” system uses a Redis⁷-based huey python package⁸ to manage the processing queue, which distributes the jobs to utilize all available computational

⁶<https://github.com/dmitrydjev/roboao-archive>

⁷An efficient in-memory key-value database.

⁸<https://github.com/coleifer/huey>

resources. The processing results together with ancillary information on individual observations and system performance are stored in a MongoDB⁹ NoSQL database. For interactive data access, we developed a web-based interface powered by the Flask¹⁰ back-end. It allows the user to access previews of the processing results together with auxiliary data (e.g. external VO images of a field), nightly summary and system performance information. The web application serves as the general interface to the database providing a sophisticated query interface and also has a number of analysis tools.

5.7 Near-infrared Camera

In November 2016, we installed a NIR camera for use with Robo-AO. While similar to the camera deployed in engineering tests at the Palomar 1.5-m telescope in 2014 (Christoph Baranec, D. Atkinson, et al., 2015), the new camera uses a science-grade detector and faster readout electronics. The detector is a Mark 13 Selex ES Advanced Photodiode for High-speed Infrared Array (SAPHIRA) with an ME-911 Readout Integrated Circuit (D. E. Atkinson et al., 2016; Baker et al., 2016). It has sub-electron readnoise and 320×256-pixel array with $\lambda = 2.5 \mu\text{m}$ cutoff. The single-board PB1 ‘PizzaBox’ readout electronics were developed at the Institute for Astronomy and we use 32 readout channels, each capable of a 2 Mpixel/sec sampling rate, for a maximum full-frame read rate of $\sim 800\text{Hz}$.

The NIR camera attaches to the Robo-AO $f/41$ infrared camera port that accesses $\lambda > 950\text{nm}$ after transmission through a dichroic. The camera has an internal cold $\lambda < 1.85 \mu\text{m}$ short-pass filter and an external warm filter wheel with J, H, clear, and blocking filters. The camera has a plate scale of $0.064''$ per pixel and field-of-view of $16.5'' \times 20.6''$.

We achieved first light on sky in February 2017 during final testing of the upgraded TCS. Initially we used a 1 Mpixel/sec sampling rate (a full frame read rate of 390 Hz) with detector resets every 300 reads. To create a reduced image, we first assembled difference frames between 39 consecutive reads, totaling ~ 0.1 s of integration time, short enough to effectively freeze stellar image displacement. We subtracted a frame median to approximate removing the background. We then synthesized a long exposure image by registering each corrected frame on the brightest target in the field. Figure 5.12 shows an example image of a binary star observed in H-band.

⁹<https://www.mongodb.com>

¹⁰<https://github.com/pallets/flask>

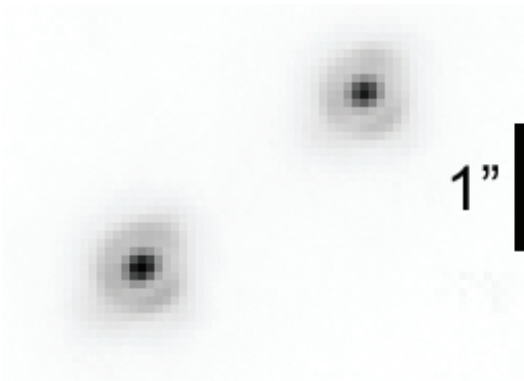


Figure 5.12: A 5.5 s image of GJ1116 taken in H-band with the near-infrared camera (linear stretch).

For the moment, data acquisition and reduction is performed manually. In the coming months, we will optimize the detector readout routines for maximum sensitivity to faint objects (including dithering for background removal), integrate the operation of the camera into the robotic queue and modify our existing data reduction pipeline to handle the NIR data. We will also investigate automating active tip-tilt correction by using either the visible or infrared camera as a tip-tilt camera, as previously demonstrated at Palomar.

5.8 Conclusion

Robo-AO at the Kitt Peak 2.1-m telescope is the first dedicated adaptive optics observatory. Observing every clear night, Robo-AO has the capacity to undertake LGS AO surveys of large samples. For instance, a 1000-star survey with exposure times of 60 s per target can be completed on the timescale of a week.

Science programs designed to exploit Robo-AO's unique capabilities are underway. These programs include stellar multiplicity in open clusters, minor planet binarity, major planet weather variability, extragalactic object morphology, sub-stellar companions to nearby young stars, M-star multiplicity, and the influence of stellar companions on asteroseismology. By the summer of 2017, Robo-AO will become the first LGS AO system to operate entirely autonomously, as on-going upgrades to the 2.1-m telescope will remove the need for a human observer.

ACKNOWLEDGMENTS

The Robo-AO team thanks NSF and NOAO for making the Kitt Peak 2.1-m telescope available. We thank the observatory staff at Kitt Peak for their efforts to assist Robo-AO KP operations. Robo-AO KP is a partnership between the California Institute of Technology, the University of Hawai‘i, the University of North Carolina at Chapel Hill, the Inter-University Centre for Astronomy and Astrophysics (IUCAA) at Pune, India, and the National Central University, Taiwan. The Murty family feels very happy to have added a small value to this important project. Robo-AO KP is also supported by grants from the John Templeton Foundation and the Mt. Cuba Astronomical Foundation. The Robo-AO instrument was developed with support from the National Science Foundation under grants AST-0906060, AST-0960343, and AST-1207891; IUCAA; the Mt. Cuba Astronomical Foundation; and a gift from Samuel Oschin. These data are based on observations at Kitt Peak National Observatory, National Optical Astronomy Observatory (NOAO Prop. ID: 15B-3001), which is operated by the Association of Universities for Research in Astronomy (AURA) under cooperative agreement with the National Science Foundation. C.B. acknowledges support from the Alfred P. Sloan Foundation.

5.9 Appendix: Telescope Jitter

After moving Robo-AO from the Palomar 1.5-m telescope to the Kitt Peak 2.1-m telescope, the median Strehl ratio across all wavelengths was initially reduced from 5.8% to 3.2%. The source of this degradation was a ~ 3.7 Hz vibration in the RA axis. Because Robo-AO mitigates tip/tilt by post facto shift and add rather than a real-time loop, and because its framerate is typically only 8.6 Hz, the targets were smeared in the RA direction. Figure 5.13 a and b show the power spectral densities of the mean subtracted RA centroid positions of targets observed at Kitt Peak and Palomar, respectively. The peak at ~ 3.7 Hz is clear in the Kitt Peak data, but is not present at Palomar. The RA-axis smearing for a single test observation is demonstrated in Figure 5.14.

The jitter was mitigated by two changes to the system. First, the KPNO staff noticed a ticking sound corresponding to each rotation of the telescope drive worm gear, which was solved by lubrication. This step reduced the height of, but did not eliminate, the PSD peak. Second, we took a test observation in which only sidereal tracking was enabled, and all fine computer guiding was turned off. The peak was absent in this

test observation, leading us to conclude that the telescope control system (TCS) was giving erroneous commands that “kicked” the telescope’s position. The TCS was replaced in the winter of 2017 to allow the Robo-AO robotic system to fully control the telescope’s motion, eliminating the remaining RA jitter (Figure 5.15). Figure 5.16 shows a comparison of the Strehl ratios versus the seeing before and after the TCS upgrade.

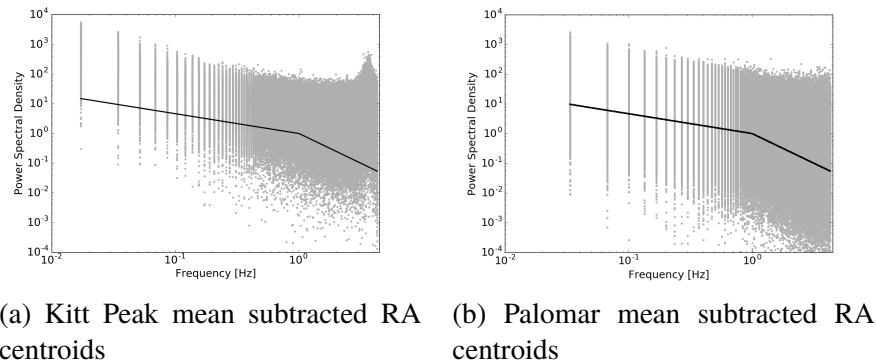


Figure 5.13: The power spectral densities of the mean subtracted RA target positions for each sub-exposure at Kitt Peak (a) and Palomar (b). The peak at ~ 3.7 Hz is present at Kitt Peak, but not at Palomar. The solid black lines show the theoretical power-law dependencies of the tilt: $f^{-2/3}$ at low frequencies, and f^{-2} for 1 – 10 Hz (Hardy, 1998).

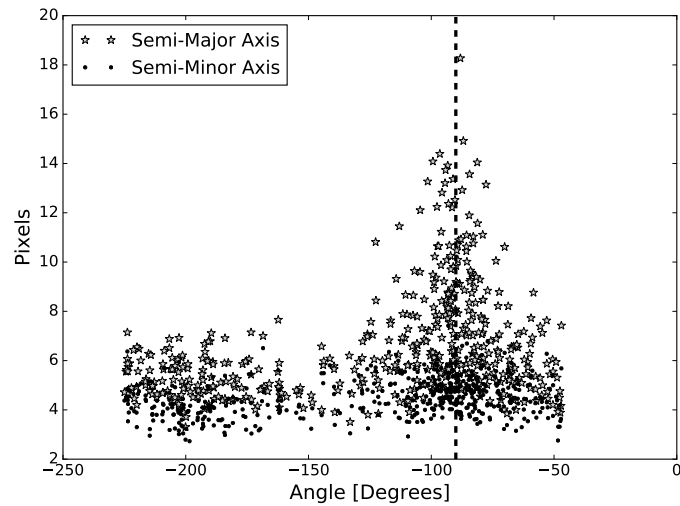


Figure 5.14: For a test observation, the standard deviation along the semi-major and semi-minor axes of 2D Gaussian fits to each 0.116s sub-exposure are plotted versus the rotation angle of the Gaussian. Here, -90° (dashed black line) indicates that the semi-major axis lies along the RA-axis. Clearly, the PSF is elongated along the RA-axis.

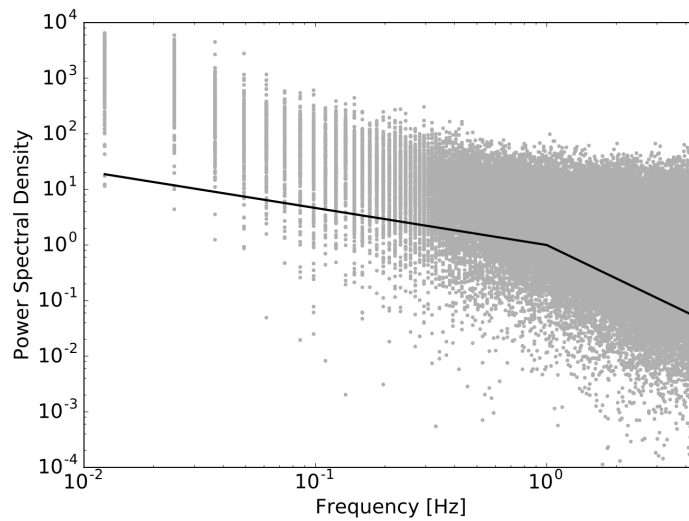


Figure 5.15: The power spectral densities of the mean subtracted RA target positions for the Kitt Peak sub-exposures since the telescope control upgrade (22 February 2017 through 8 March 2017). The peak that was present in Figure 5.13a is eliminated.

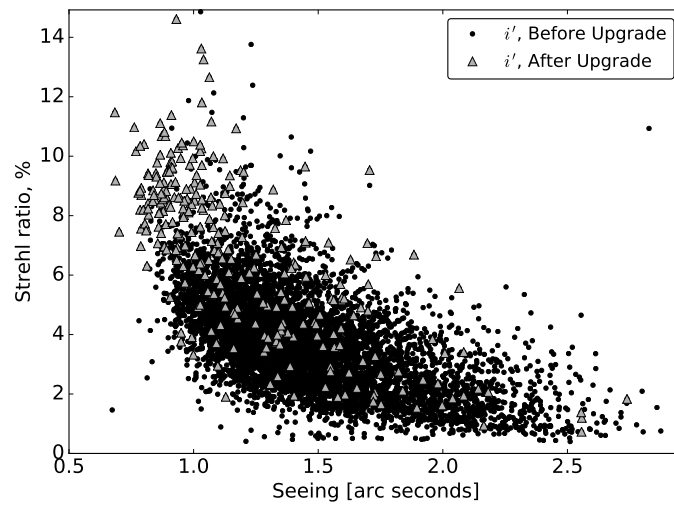


Figure 5.16: Strehl ratios of the observations taken in i' as a function of the seeing scaled to 500 nm before (December 2015 through 22 February 2017; black points) and after (22 February 2017 through 10 March 2017; gray stars) the enhancements. Note the significant improvement for seeing under ≈ 1.1 arcseconds.

*Chapter 6*THE EFFECT OF COMPANIONS ON STELLAR ANGULAR
MOMENTUM IN THE PLEIADES

ABSTRACT

We present laser guide star adaptive optics observations of 525 Pleiades members using Robo-AO at the Kitt Peak 2.1-m telescope and NIRC2 at the Keck II telescope. These targets are drawn from Pleiades members with rotational period measurements from *K2* light curves (Rebull et al., 2016). From our sample of Robo-AO observations, we identify 40 candidate binaries with projected separations ranging from 0.4'' to 7.5'' (54.3 – 1021.1 au). We further identify 19 candidate binary systems with Keck/NIRC2, with separations ranging from 0.08'' to 0.7'' (10.6 – 102.1 au). Given prior observational evidence that circumstellar disks brake the rotation of pre-main sequence stars and the prediction that close stellar companions disrupt the disk, we investigate the hypothesis that Pleiades members with close companions spin faster than single stars or those with distant companions. We do not find evidence of a relationship between the observed binaries' separations and rotational periods.

6.1 Introduction

Measurements of stellar angular velocities (Ω_*) in clusters of varying ages show an evolution that drastically differs from simple angular momentum conservation (Figure 6.1; Gallet and Bouvier, 2013; Bouvier, Matt, et al., 2014). The latter predicts that Ω_* should increase as the star contracts onto the zero age main sequence (ZAMS), and then remain constant during the main sequence phase. Observations show a much more complicated picture – a star’s angular velocity remains constant for the first few million years, then increases until the ZAMS, and decreases afterwards.

The duration of the early, constant Ω_* phase coincides with the lifetimes of accretion disks, suggesting that star-disk interactions regulate a star’s angular velocity. There are several possible mechanisms for this regulation, including disk-locking (Ghosh and Lamb, 1979), accretion-powered stellar winds (Shu et al., 1988; L. Hartmann and J. R. Stauffer, 1989), magnetospheric ejections (Hayashi, Shibata, and Matsumoto, 1996), and X-winds (Ostriker and Shu, 1995), but the detailed physics and applicability of these mechanisms to a wide range of stellar masses remains poorly understood.

However, even without a detailed picture of star-disk interactions, the data in Figure 6.1 suggest that the lifetime of the disk affects the star’s subsequent rotational evolution – the shorter the lifetime of the disk, the more time the star has to spin up before reaching the ZAMS.

Observations of stellar multiplicity in nearby star forming regions indicate that binary systems are the preferred output of star formation (e.g. Simon et al., 1995). Given that most solar-type stars form with one or more companions, the effect of stellar companions on disks and subsequent angular momentum evolution must be considered in order to gain a complete picture of star and planet formation.

For close stellar companions that each retain their own accretion disk, Papaloizou and Pringle (1977) suggest that the individual components’ disks are tidally truncated to about $0.3a - 0.5a$, or about ten times smaller than the typical ~ 100 au extent of an accretion disk around a single star (here, a is the distance between the two stars). Because the viscous timescale of the disk is proportional to its radius, the disk’s lifetime may also be shortened by about a factor of ten. On the other hand, if the disk material is being replenished by a circumbinary disk or envelope, the truncated disks’ lifetimes may ultimately match those of single star disks. Observations, however, generally support shorter lifetimes: for example, Cieza et al. (2009) observed 125

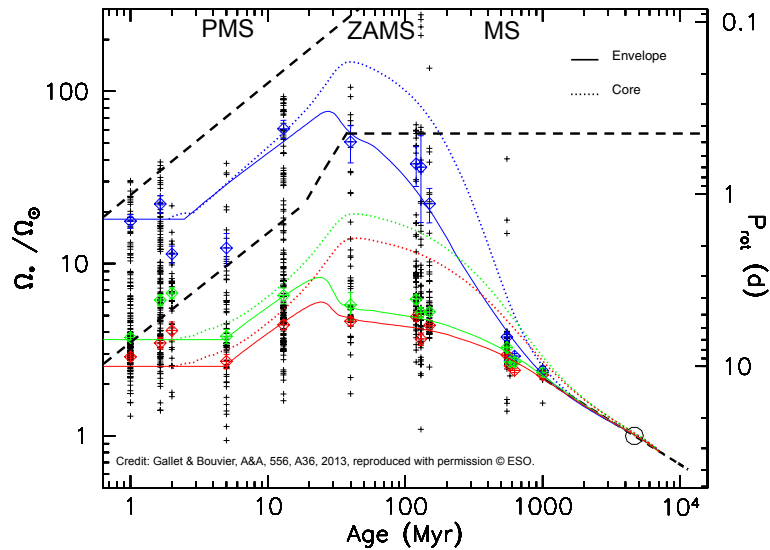


Figure 6.1: The observed angular velocities of solar-type pre-main sequence stars in clusters as a function of age. The circle indicates the Sun. The solid lines show a simulation of the angular velocity of the convective envelope, while the colored dotted lines represent the radiative core. The blue, green, and red colors indicate fast, medium, and slow rotator categories respectively. The black dashed lines show the rotational evolution assuming conservation of momentum starting with the same initial rotations as the blue and red lines. This figure is adapted from Gallet and Bouvier (2013).

binary pre-main sequence (PMS) stars with *Spitzer* and concluded that binaries with smaller separations are less likely to meet their disk-indicator color criterion. Furthermore, binaries with $a < 100$ au in Scorpius-Ophiuchus and Taurus-Auriga have decreased millimeter and submillimeter flux compared with wider binaries, supporting the hypothesis that closer binaries have shorter disk lifetimes (Beckwith et al., 1990; Jensen, Mathieu, and Fuller, 1996).

If this hypothesis is correct, then closer binaries would also be expected to rotate more quickly at a given age because they would have had more time to spin up between the dissipation of the disk and contraction onto the ZAMS. Open clusters are an ideal laboratory for studying this relationship because their members formed at the same time and in a similar environment – two important considerations given the variations observed in rotational periods as a function of time and between similarly aged clusters. The Pleiades is well-suited to these measurements because at 136.2 pc away it lends itself well to imaging surveys, and with an age of 125 Myrs, Figure 6.1 indicates that it should still show a diversity of rotational periods (Melis et al., 2014; J. R. Stauffer, Schultz, and Kirkpatrick, 1998). However, when Bouvier,

Rigaut, and Nadeau (1997) compared the separations of twelve $a < 100$ au binaries in the Pleiades with previous $v\text{sini}$ measurements, no correlation between separation and rotation was found. There could be many reasons for this finding – the sample size was small, $v\text{sini}$ is an imperfect proxy for Ω_* , and perhaps the complexity of the first 125 Myrs of angular momentum evolution in 10 – 100 au binaries is not yet appreciated. On the other hand, Patience et al. (2002) compared the $v\text{sini}$ and separations of 16 solar-type binaries in α Persei, and concluded that binaries with $a < 60$ AU are indeed rotating more quickly than binaries with larger separations.

A new dataset is now available to shed new light on the evolution of stellar angular momentum. For 72 days in 2015, the NASA *K2* space telescope continuously observed 1020 candidate Pleiades members with a 30 minute cadence. Rebull et al. (2016) analyzed the light curves from these data to obtain rotational period measurements of 759 high-confidence Pleiades members – the most complete census of its kind due to the sensitivity, photometric precision, and continuity of the *K2* data. However, *K2* is not well suited to resolving stellar binaries in part because its detector’s pixels are $3.98'' \times 3.98''$. In this chapter, we present laser guide star adaptive optics observations of 525 Pleiades targets from the periodic *K2* sample. These high-resolution images allow for the identification and characterization of 59 candidate binary systems.

6.2 Observations

In order to resolve binary star systems from among the Rebull et al. (2016) sample of 759 Pleiades members with periodic *K2* lightcurves, we observed the 465 $i' < 15$ targets with Robo-AO at the Kitt Peak 2.1-m telescope and 60 $10.9 < K_s < 13.7$ targets with Keck/NIRC2. These observations are described in detail below.

Robo-AO

Robo-AO is a robotic adaptive optics system newly commissioned at the Kitt Peak 2.1-m telescope (see Chapter 5). Because Robo-AO is capable of observing > 200 distinct targets per night, it is the ideal adaptive optics system for the large-scale survey described here.

The i' filter was used for all Robo-AO observations. Of the installed g' , r' , i' , and z' filters, the i' filter is an appropriate compromise between the rapidly decreasing quantum efficiency of the detector beyond 800 nm and the red colors of the low-mass Pleiades targets. Robo-AO also provides a clear window and a long-pass filter cutting on at 600 nm and extending to the red limit of the detector. Previous

binary searches with Robo-AO have chosen the long-pass filter for initial binary identification to maximize the flux contribution from a faint secondary. The newly discovered binaries were then followed up in multiple filters. However, because this survey was conducted during Robo-AO’s commissioning at Kitt Peak, the i' filter was chosen for all observations as a risk management strategy: while published evolutionary models can provide a mass estimate based on $M_{i'}$, no such models are available for the specialized long-pass filter. Hence, any binaries that could not be re-observed due to instrument down time or under-performance during commissioning would be missing a robust mass measurement. Hence, we decided to observe all targets in i' in order to guarantee a mass measurement for all binaries regardless of the availability of follow-up observations.

As the performance of Robo-AO improved between the instrument’s first light in November of 2015 and the conclusion of the telescope control system upgrade in March of 2017, observations of the Pleiades targets were attempted several times. Approximately 70% of the targets were successfully observed more than once, and in this sample the average number of observations was four. The remaining 30% of the sample tended to be faint stars whose observations failed in poor seeing conditions. For those targets with multiple observations, the “best” observation to be used for companion searches was chosen based on the nearest seeing measurements. The seeing was chosen as the selection metric rather than the Strehl ratio because many of the observations were only reduced with the faint pipeline where the Strehl measurement code has not yet been validated.

For the selected observations, Figure 6.2 shows histograms of the targets’ elevations at the time of the observation, estimated i' magnitudes, nearest seeing measurements, and Strehl measurements (for those targets that were processed with the bright star pipeline only). The i' magnitudes were calculated using a combination of the target K_s magnitudes reported by Rebull et al. (2016) and 120 Myr BT-Settl evolutionary models given by Allard, Homeier, and Freytag (2011).

The Robo-AO observations were carried out with an Andor iXon+ 888 electron multiplying CCD (EMCCD). Approximately 80% of the selected observations were taken with Robo-AO’s default framerate of 8.6 Hz. For the remaining 20% of the observations, the center 1/4 of the detector was read out at ~ 35 Hz to provide an improved tip/tilt correction in post-processing. The choice of the standard versus “high speed” mode is at the discretion of the observer, where the high speed mode is typically selected for stars brighter than 13th magnitude when the seeing is $\lesssim 1.5''$.

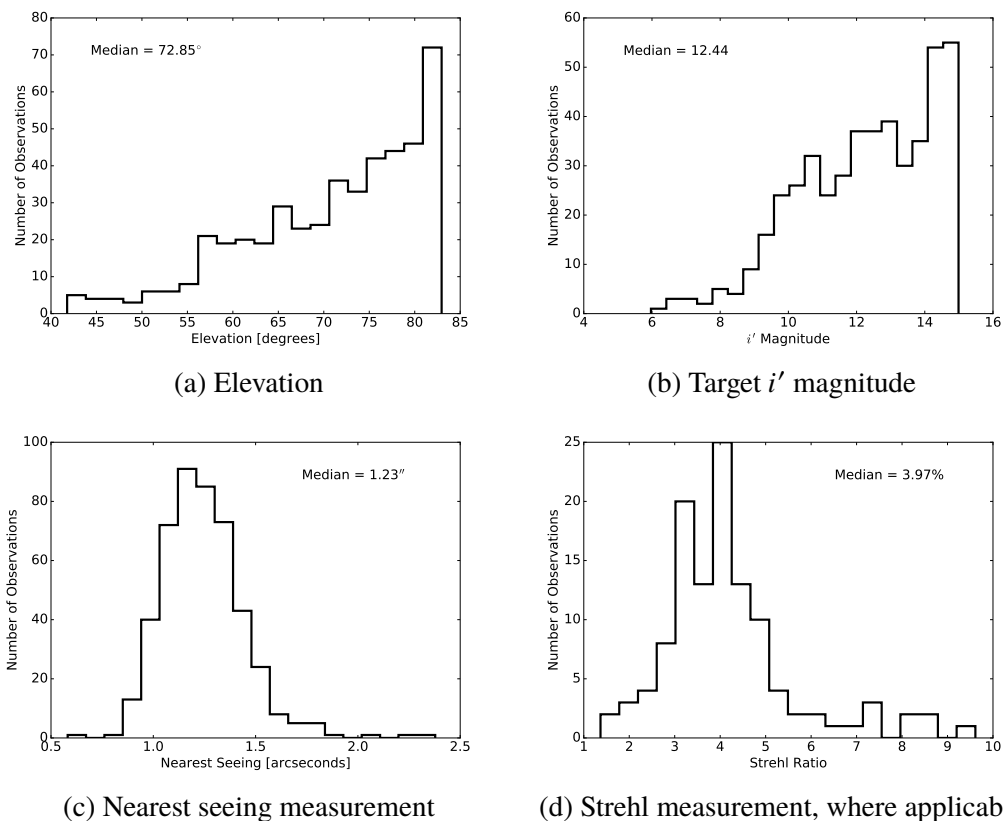


Figure 6.2: A summary of the Robo-AO Pleiades observations selected for companion searches.

Table 6.1: Robo-AO EMCCD Gain Values

Target Magnitude	EM Gain Value
< 8	5
8 – 10	50
10 – 12	100
12 – 13	200
> 13	300

For both the standard and high speed observing modes, the detector is read out with a 10 MHz 14 bit electron multiplying amplifier with a pre-amplifier sensitivity of $10.9 e^-/ADU$. The EM gain value is then chosen based on the target star's magnitude (Table 6.1), where fainter stars are multiplied by a higher gain value.

The data were processed by both the bright and faint star pipelines described in Chapter 5. The final shifted-and-added frames provided by each of these pipelines were multiplied by $10.9 e^-/ADU$ divided by the appropriate EM gain value.

Keck NIRC2

Because Robo-AO’s post-facto tip/tilt correction strategy requires guide stars brighter than about 15th magnitude in the filter of observation, the Robo-AO Pleiades sample is incomplete for masses less than about $0.4 M_{\odot}$. Hence, we observed 60 low mass Pleiades objects with the Keck/NIRC2 laser guide star adaptive optics system over two nights: UT 10 October 2016 and 6 November 2016. Due to a temporary problem with the laser guide star on the first night of observations, three bright ($K_s < 10$) Pleiades targets were also observed using natural guide star AO.

The DIMM seeing varied from $0.4''$ to $1.1''$, with some high cirrus clouds on the first night. The airmass ranged from 1.0 to 2.16, with some elongation of the PSF observed at larger airmasses.

For both nights of observation, we chose the K_s filter to maximize our sensitivity to red companions. We chose the narrow camera mode, giving a field of view of $10.2'' \times 10.2''$. We dark subtracted, flat fielded, cleaned, and combined the images for each target star using the Keck/NIRC2 data pipeline developed by Henry Ngo (Ngo et al., 2015). We then multiplied each reduced frame by the detector gain of $4e^-/\text{ADU}$.

6.3 Binary System Analysis

Identification of Candidate Binary Systems

The candidate binary systems were identified by visual inspection. For the Keck/NIRC2 data, this yielded unambiguous results: 19 stars had candidate binary companions. The calculation of the binary systems’ separations and mass ratios are discussed in the following subsection.

The Robo-AO data, however, included a wider variety of observing conditions and stars per frame. For each of the selected Robo-AO observations (see Section 6.2), we visually inspected three frames: the final frames produced by the faint and bright star pipelines, and the PSF-subtracted inner region of the frame produced by the combination of the bright star pipeline and the high contrast pipeline (see Chapter 5 for a description of these pipelines). Because we are interested in the gravitational interactions of binary pairs and their disks, we considered only candidate companions within 1000 au of the target star, as the typical extent of a G-star circumstellar disk is 100 au. We identified 40 such binary candidates. None of these candidate companions required PSF subtraction to be identified, so we simplified the subsequent analysis by considering only non-PSF subtracted frames. For subsequent

analysis steps, we then needed to choose between the frames generated by the bright and faint star pipelines. While this choice was not always straightforward, we found that the bright star pipeline’s PSF-subtracted frames showed a single bright pixel in the center of the residual PSF for very faint stars, indicating that the shift-and-add algorithm had given erroneous results (see Chapter 5). For stars with that residual pattern, we selected the faint star pipeline.

Separation and Flux Ratio Measurements

We now wish to measure the separations and flux ratios of each of the candidate binary systems. Our strategy for these measurements will be to fit model functions to the stellar PSFs. For “close” binary systems with significant flux overlap, we will simultaneously fit the PSFs, while for “wide” systems we will fit the two stars independently. We consider all of the binary systems identified with Keck/NIRC2 to be close; while the full width at half maxima of the Robo-AO binary sample vary, we find that a threshold separation of $3''$ is adequate in the sense that simultaneous and independent fits give similar results for test binaries larger than that separation.

For each of the stars in the widely separated binary systems, we fit the PSFs with the sum of a constant and the following 2D functions: a single Gaussian, the sum of two Gaussians, and the sum of three Gaussians (see B. P. Bowler and Hillenbrand (2015) for a discussion of a similar approach using Keck/NIRC2 data). We simultaneously fit combinations of this same set of functions to the close binary systems. The functions were fit using the `astropy` implementation of the Levenberg-Marquardt algorithm, and the best fitting function was chosen by the least squares statistic. The data that requires the faint pipeline is typically very low Strehl and hence each PSF is well-fit by a single Gaussian function. The PSFs in high Strehl data, however, include both a sharp $\sim \lambda/D$ -sized core and a broader halo. These PSFs are best fit by the sum of two or three Gaussian functions. We note that some of the stars were better fit by the sum of two Moffat functions than any of the aforementioned Gaussian distributions; however, the integral of the best fitting Moffat function was often divergent, giving unstable results for the binary pair’s flux ratio.

Each binary separation is then simply the distance between the means of the best fitting distributions. To calculate the flux ratio, a model image is created separately for each star in a system. For those binaries in which both stars are best fit by single Gaussians, we draw an aperture around the 2σ contour of each model (hence this aperture is allowed to be elliptical), and take the binary flux ratio to be the ratio of

these aperture sums. For binaries in which one or more component is best fit by the sum of multiple Gaussians, we generate a model image for each star that extends far enough for the model flux to go to zero in all directions to machine precision. The flux ratio is then the ratio of the sums of these large model images.

To estimate the uncertainties on the binary separations and flux ratios, we repeat the fitting and measurement steps described above 1000 times, each using a new “original” Robo-AO image, where each pixel in the new image is drawn from a Poisson distribution whose mean is the value of that pixel in the true original frame. The peak location of a histogram of the 1000 values of the parameter in question is taken to be the peak of that parameter’s probability density function. The 68% confidence interval is found by constructing an empirical cumulative distribution (ECDF) function of the 1000 values and finding the shortest interval that encompasses 68% of the values. An example of a histogram and ECDF generated by this process is shown in Figure 6.3. We note that the our confidence intervals do not account for the fact that the Gaussian models are imperfect fits to the data. To briefly address this point, we simulated three-component-Gaussian binary stars of various widths and separations and obtained their flux ratios and separations by fitting them to single-component Gaussians. For typical widths and separations represented by the “close” binary star data, we find that the errors due to a poor choice of model are likely on the order of 10%.

To translate our measured flux ratios into mass ratios, we first adopt the absolute K_s magnitudes obtained by J. Stauffer et al. (2016) for the Pleiades K2 sample. These values have been shifted based on the authors’ single-star K_s versus $(V - K_s)$ track; this approach accounts for the overbrightness of photometric binaries in such a way that the final K_s magnitudes represent the primary star’s magnitude only. We then use 120 Myr BT-Settl evolutionary models given by Allard, Homeier, and Freytag (2011) to obtain the primary stars’ masses based on their corrected K_s values assuming a Pleiades distance of 136.2 pc. Because the BT-Settl models provide masses based on both K_s and i' magnitudes, we can translate our 68% confidence interval flux ratios into upper and lower bounds on the secondary star’s mass.

Table 6.2 summaries the results of this analysis. Figure 6.4 plots the best fit mass ratios versus the best fit separations. Clearly, our observations are more sensitive to higher mass ratio companions when the projected separation is larger.

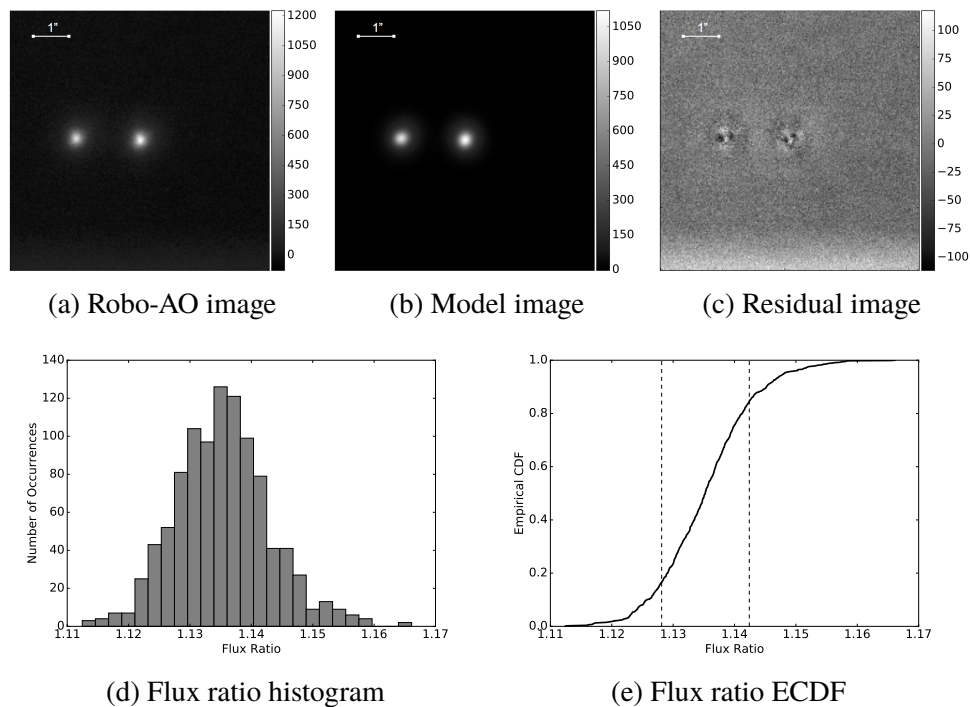


Figure 6.3: An example sequence of images showing the Robo-AO observation of EPIC 211078780 on 22 February 2017 in (a). The i' image was processed with the faint star pipeline. Panel (b) shows the simultaneously fit models to the primary and secondary stars, where each star was modeled as the sum of two Gaussian distributions. Panel (c) shows the difference between the observation and the model. Panel (d) plots the histogram of the primary-to-secondary flux ratio measurements generated by many realizations of Poisson noise in the original image. The corresponding empirical cumulative distribution function of the flux ratio measurements is shown in panel (e), where the dotted lines represent the 68% confidence interval.

6.4 Discussion

Figure 6.5 plots the rotational periods of all Pleiades members measured by Rebull et al. (2016) versus their $(V - K_s)_0$ color, where the stars observed with adaptive optics (this work) are shown in color. There are several distinct regimes in this period-color diagram: $1.1 < (V - K_s)_0 < 3.7$ represents F5 - K8 stars at or near the zero age main sequence whose magnetized stellar winds have started to break their rotation according to their mass. Redward of $(V - K_s)_0 = 3.7$ (M dwarfs), the sample follows a $P \propto M^{1.5}$ relation. It is clear that the sample presented here is less complete for $(V - K_s)_0 > 5$, where the stars are generally too faint in i' for Robo-AO observations. Figure 6.6 shows a histogram of the Pleiades observations by color.

We will now proceed by examine the “slowly rotating” sequence in the color range

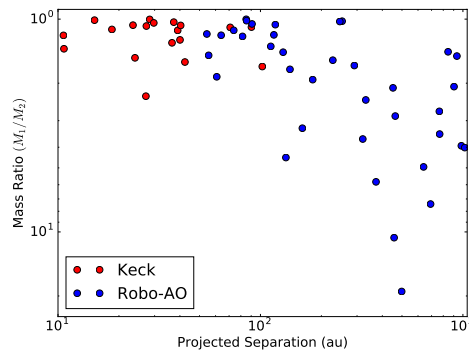


Figure 6.4: This figure shows the best fit mass versus the best fit separation for the binary candidates identified with Keck/NIRC2 (red points) and Robo-AO (blue points).

$1.1 < (V - K_s)_0 < 3.7$, and testing the hypothesis that stars with closer companions have shorter rotational periods than stars with more distant companions.

J. Stauffer et al. (2016) identify three distinct populations in the $1.1 < (V - K_s)_0 < 3.7$ color space: slow, intermediate, and fast rotators. They define the “slow” locus using a 2nd degree polynomial fit to the $1.1 < (V - K_s)_0 < 2.6$ and $2.6 < (V - K_s)_0 < 3.7$ regions in period logspace. Those stars within 30% of the fitted lines are labeled as “slow” rotators. Stars with $0.13 < P/P_{fit} < 0.7$ are “intermediate” rotators while stars with $P/P_{fit} < 0.13$ are “fast rotators” (P_{fit} being the fitted period at that color). These populations are indicated in Figure 6.7.

J. Stauffer et al. (2016) find that 62% of photometric binaries in their sample fall in the intermediate population compared with 22% of supposedly single stars. They suggest that this displacement is due to the deleterious effect of a stellar companion on disk-dependent angular momentum regulation. Similarly, we find that 52% of the binary candidates identified with Robo-AO fall in the intermediate population compared with 24% of stars for which Robo-AO revealed no companions. However, we find no difference between the mean projected separation of the binaries in the slow and intermediate populations. We might consider only those binaries with separations less than 100 au (the typical extent of the disk surrounding a single G-type star), but there are only five such candidate binaries in this color range. It may also be the case that comparatively low mass companions do not significantly affect the primary’s rotation. When we consider only those binaries with $M_1/M_2 < 2$, only three and six targets remain in the slow and intermediate populations, respectively; their mean projected separations are not significantly different.

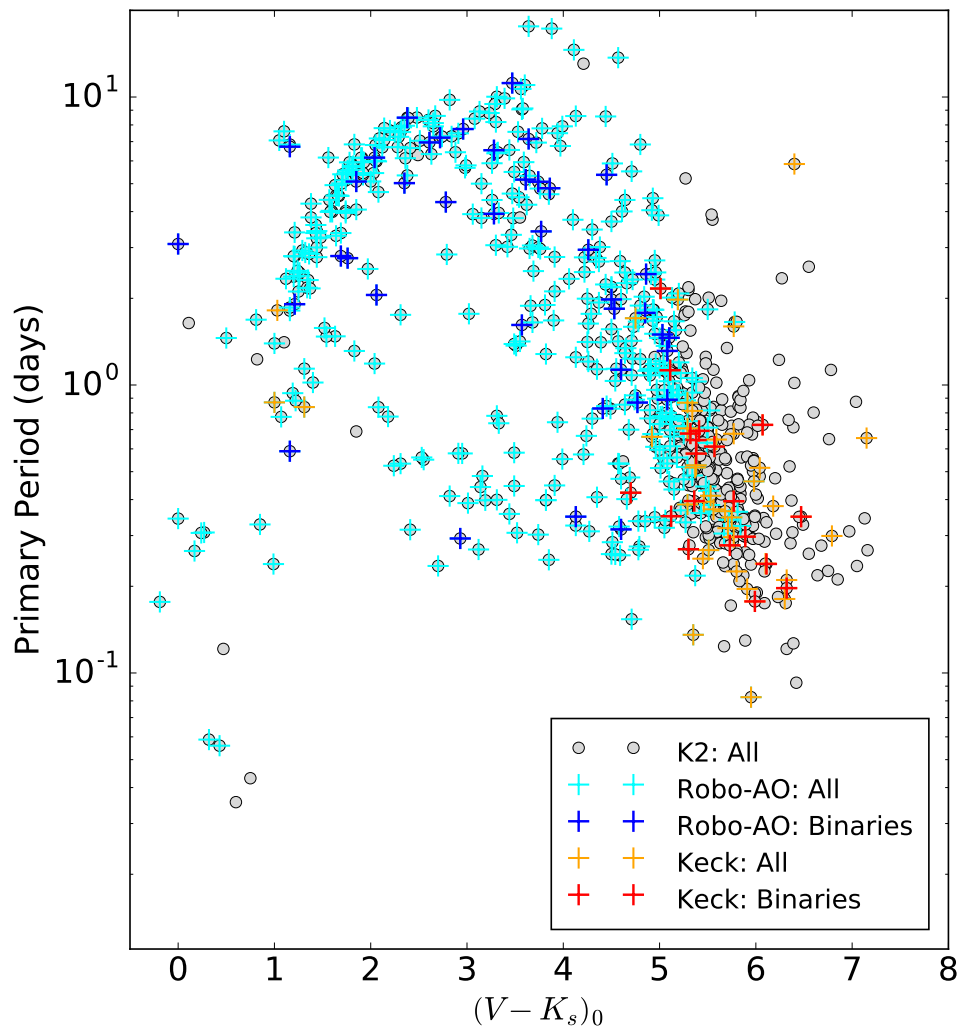


Figure 6.5: A period-color diagram where the periodic Pleiades members are shown in gray (Rebull et al., 2016), the subset observed with Robo-AO are shown in cyan (single stars) and blue (binary candidates), and the subset observed with Keck/NIRC2 are shown in orange (single stars) and red (binary candidates).

We now consider the color range $4.0 < (V - K_s)_0 < 7.0$ (M spectral types). This region does not include such distinct populations as the $1.1 < (V - K_s)_0 < 3.7$ slow, intermediate, and fast groups. However, we continue to follow J. Stauffer et al. (2016) by dividing this redder color region into six bins of width 0.4, and fitting the mean rotational periods in each bin with a function of the form $P \propto M^\alpha$, where the best fitting α is 1.5. This line is plotted in black in Figure 6.8. We note that for consistency with J. Stauffer et al. (2016), we have used Baraffe et al.

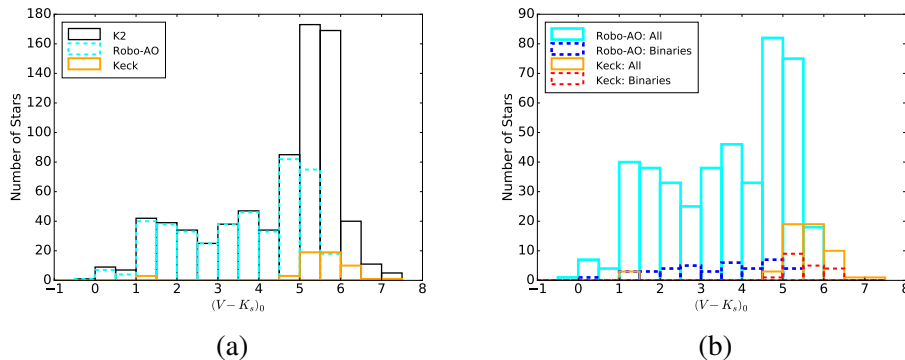


Figure 6.6: Left: A histogram of periodic Pleiades observations by K2 (gray), Robo-AO (cyan), and Keck/NIRC2 (orange). Right: A histogram of Robo-AO and Keck/NIRC2 observations with the binaries marked in dashed lines.

(2015) isochrones of the appropriate age and distance to construct this fit rather than the BT-Settl models used in Section 6.2 to compute the mass ratios of the binaries. While 15 binaries were identified with Robo-AO in the approximate range $4.0 < (V - K_s)_0 < 5.0$, here we only consider the Keck/NIRC2 observations where the companion sensitivity was the most uniform.

While J. Stauffer et al. (2016) find evidence that photometric binaries and targets with multi-periodic lightcurves (presumably due to multiple stars) are preferentially fast rotators, our binaries resolved with Keck are equally likely to fall above or below the best fit line in Figure 6.8. Furthermore, the mean projected separations of the binaries are indistinguishable above and below the best fit line. Because all but one of the binaries resolved with Keck/NIRC2 have mass ratios less than two, this result is probably not due to the varying effects of companions with different masses.

6.5 Conclusion and Future Work

We find no relationship between the rotational periods and the projected separations of the candidate binary systems identified with Robo-AO and Keck/NIRC2. If we accept the J. Stauffer et al. (2016) conclusion that binaries in the Pleiades have systematically shorter periods than single stars (due to the dynamical truncation and hence shorter lifetime of the primary star’s disk), then it is reasonable to expect that a larger sample of resolved binaries would reveal a systematic difference between the rotational periods of close and wide binary systems.

An important extension to the work presented here will be to understand the adaptive optics surveys’ sensitivities to companions of different mass ratios as a function of

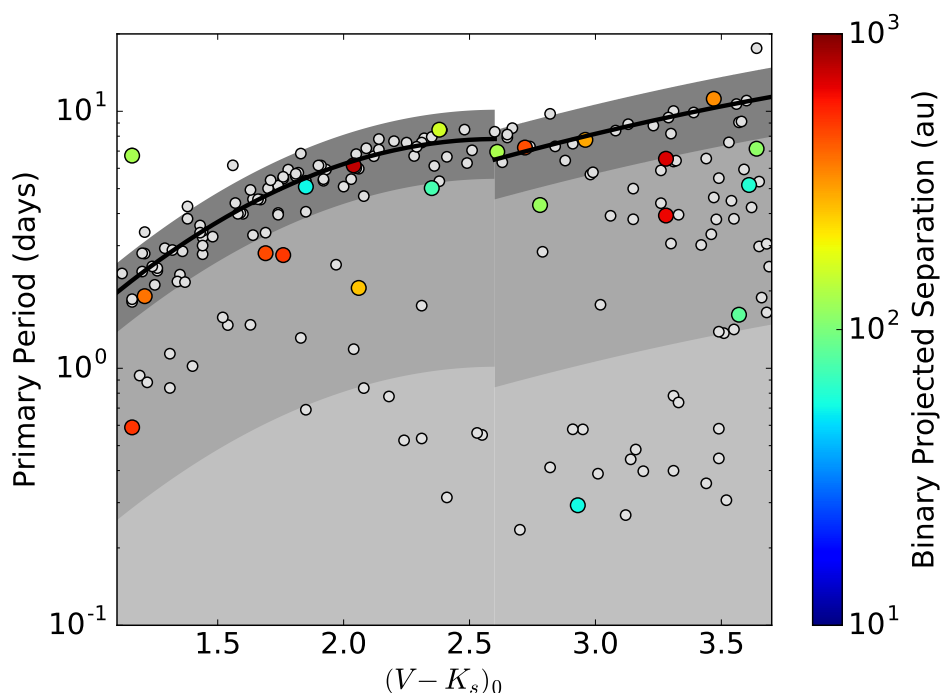


Figure 6.7: All periodic Pleiades members observed with K2 (gray circles) and Robo-AO binary candidates (circles colored by the projected separation of the binary) for the color range $1.1 < (V - K_s)_0 < 3.7$ (FGK stars). The “slow” sequence (dark gray shaded region) includes stars with periods falling within 30% of the best fit lines shown in black. The “intermediate” sequence (medium gray shaded region) includes star with periods 30% to 87% shorter than the best fit lines. Finally, the “fast” sequence (light gray shaded region) are stars with periods more than 87% shorter than the best fit lines.

separation from the primary star. This task will be more straightforward after re-observing the Pleiades in the fall of 2017 (much of dataset presented here was affected by telescope jitter and ADC calibration issues, which were mitigated in the spring of 2017 just as the Pleiades were setting). Re-observing the targets presented here will also allow us to determine whether the candidate binaries are truly bound. Finally, re-observing the sample with Robo-AO’s recently installed infrared camera will increase our sensitivity to lower mass stellar companions.

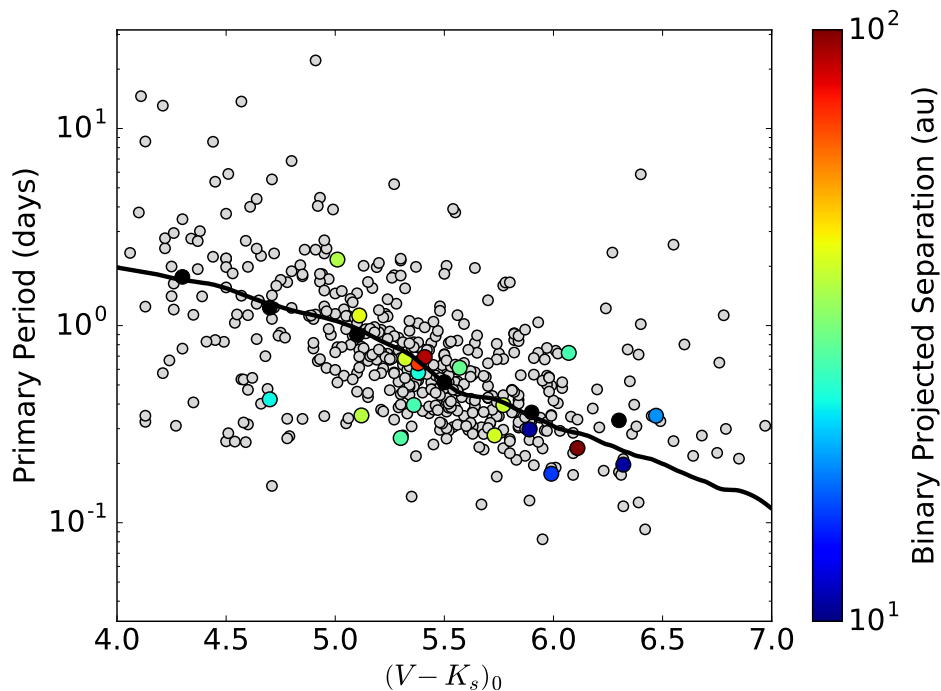


Figure 6.8: All periodic Pleiades members observed with K2 (gray circles) and Robo-AO binary candidates (circles colored by the projected separation of the binary) for the color range $4.0 < (V - K_s)_0 < 7.0$ (M stars). The black circles are the binned points to which the black line ($P \propto M^{1.5}$) is fit.

Table 6.2: Derived Parameters for Pleiades Binaries

EPIC Name	Pri. M_{\odot}	ΔM_{\odot}	Sep. (au)	Instrument
210833049	0.59	$1.19^{+0.05}_{-0.08}$	$116.49^{+5.82}_{-5.28}$	Robo-AO
211014883	1.2	$1.17^{+0.08}_{-0.04}$	$54.35^{+2.73}_{-0.37}$	Robo-AO
211046494	0.83	$3.26^{+0.37}_{-0.51}$	$161.11^{+7.23}_{-3.57}$	Robo-AO
211070599	1.29	$1.02^{+0.0}_{-0.0}$	$253.12^{+0.06}_{-0.1}$	Robo-AO
211115638	1.22	$5.82^{+0.21}_{-0.15}$	$372.21^{+0.17}_{-0.63}$	Robo-AO
211086025	0.96	$1.06^{+0.0}_{-0.0}$	$118.44^{+0.12}_{-0.11}$	Robo-AO
210966700	1.06	$1.13^{+0.03}_{-0.06}$	$73.79^{+0.81}_{-0.69}$	Robo-AO
211106344	1.05	$1.48^{+0.17}_{-0.16}$	$55.46^{+13.82}_{-4.01}$	Robo-AO
210977505	0.66	$2.4^{+0.01}_{-0.03}$	$331.34^{+0.38}_{-0.37}$	Robo-AO
211030680	0.72	$1.34^{+0.01}_{-0.05}$	$112.45^{+1.02}_{-2.64}$	Robo-AO
211046240	0.83	$1.0^{+0.01}_{-0.01}$	$85.04^{+0.24}_{-0.29}$	Robo-AO
211047980	0.61	$1.19^{+0.02}_{-0.02}$	$63.96^{+0.63}_{-0.44}$	Robo-AO
211059650	0.68	$1.05^{+0.06}_{-0.03}$	$90.85^{+0.42}_{-0.5}$	Robo-AO

211059979	0.55	$1.02^{+0.02}_{-0.0}$	$85.33^{+0.3}_{-0.56}$	Robo-AO
211064196	0.6	$1.21^{+0.02}_{-0.01}$	$81.54^{+0.91}_{-0.4}$	Robo-AO
211074858	0.44	$1.72^{+0.13}_{-0.15}$	$139.88^{+5.61}_{-4.38}$	Robo-AO
211076650	0.66	$1.56^{+0.02}_{-0.02}$	$227.73^{+1.51}_{-1.53}$	Robo-AO
211078780	0.75	$1.03^{+0.0}_{-0.0}$	$246.57^{+0.19}_{-0.1}$	Robo-AO
211087985	0.6	$4.47^{+0.98}_{-1.54}$	$133.56^{+16.37}_{-14.68}$	Robo-AO
211090866	0.43	$3.94^{+0.03}_{-0.18}$	$982.63^{+0.74}_{-0.67}$	Robo-AO
211099297	0.81	$2.1^{+0.02}_{-0.01}$	$451.57^{+0.22}_{-0.36}$	Robo-AO
211106969	0.65	$1.92^{+0.01}_{-0.13}$	$181.12^{+3.15}_{-1.01}$	Robo-AO
211118542	0.96	$1.43^{+0.02}_{-0.08}$	$129.4^{+2.32}_{-4.17}$	Robo-AO
211120664	0.43	$3.66^{+0.17}_{-0.08}$	$320.18^{+2.6}_{-1.16}$	Robo-AO
211122237	0.69	$1.87^{+0.08}_{-0.25}$	$60.82^{+4.58}_{-2.67}$	Robo-AO
211153286	0.84	$1.65^{+0.03}_{-0.03}$	$291.0^{+3.27}_{-0.65}$	Robo-AO
211066337	0.91	$3.47^{+-2.36}_{-2.37}$	$767.45^{+0.24}_{-0.48}$	Robo-AO
211015853	1.17	$19.05^{+-15.73}_{-15.77}$	$498.21^{+0.13}_{-0.23}$	Robo-AO
211028956	0.91	$10.64^{+-8.65}_{-8.67}$	$457.29^{+0.19}_{-0.15}$	Robo-AO
210927331	0.39	$1.49^{+0.02}_{-0.02}$	$933.79^{+0.65}_{-0.43}$	Robo-AO
210963935	0.62	$4.02^{+0.11}_{-0.04}$	$1021.09^{+0.71}_{-1.37}$	Robo-AO
210965155	0.65	$7.4^{+0.12}_{-0.24}$	$692.11^{+0.64}_{-1.9}$	Robo-AO
210996584	0.56	$2.08^{+0.05}_{-0.01}$	$903.88^{+0.49}_{-0.68}$	Robo-AO
211020371	0.45	$1.42^{+0.03}_{-0.02}$	$844.79^{+0.54}_{-0.94}$	Robo-AO
211023687	0.69	$4.95^{+0.13}_{-0.13}$	$639.17^{+1.72}_{-0.42}$	Robo-AO
211063935	0.41	$2.85^{+0.09}_{-0.01}$	$463.4^{+0.79}_{-0.62}$	Robo-AO
211103222	0.49	$2.71^{+0.03}_{-0.03}$	$765.15^{+0.64}_{-0.56}$	Robo-AO
210940129	0.24	$2.3^{+0.16}_{-0.26}$	$27.17^{+0.1}_{-0.07}$	Keck/NIRC2
211005163	0.2	$1.67^{+0.01}_{-0.01}$	$102.13^{+0.05}_{-0.02}$	Keck/NIRC2
211017407	0.21	$1.38^{+0.45}_{-0.12}$	$10.7^{+0.08}_{-0.07}$	Keck/NIRC2
211023167	0.5	$1.0^{+0.0}_{-0.0}$	$28.37^{+0.01}_{-0.01}$	Keck/NIRC2
211036881	0.44	$1.52^{+0.26}_{-0.15}$	$24.0^{+0.16}_{-0.18}$	Keck/NIRC2
211038622	0.28	$1.13^{+0.02}_{-0.01}$	$39.01^{+0.11}_{-0.17}$	Keck/NIRC2
211045153	0.58	$1.07^{+0.0}_{-0.0}$	$23.46^{+0.0}_{-0.0}$	Keck/NIRC2
211057712	0.36	$1.07^{+0.02}_{-0.02}$	$40.34^{+0.04}_{-0.05}$	Keck/NIRC2
211059981	0.41	$1.08^{+0.05}_{-0.03}$	$27.32^{+0.03}_{-0.03}$	Keck/NIRC2
211063361	0.42	$1.03^{+0.0}_{-0.01}$	$37.31^{+0.11}_{-0.36}$	Keck/NIRC2
211066062	0.26	$1.19^{+0.29}_{-0.3}$	$10.64^{+0.22}_{-0.65}$	Keck/NIRC2
211080177	0.21	$1.12^{+0.03}_{-0.08}$	$18.47^{+0.11}_{-0.06}$	Keck/NIRC2

211093040	0.49	$1.29^{+0.03}_{-0.02}$	$36.57^{+0.01}_{-0.19}$	Keck/NIRC2
211109330	0.26	$1.01^{+0.14}_{-0.04}$	$15.15^{+0.02}_{-0.15}$	Keck/NIRC2
211121361	0.46	$1.09^{+0.01}_{-0.01}$	$70.89^{+0.21}_{-0.07}$	Keck/NIRC2
211125236	0.4	$1.25^{+0.04}_{-0.06}$	$40.05^{+0.02}_{-0.01}$	Keck/NIRC2
211132712	0.48	$1.59^{+0.03}_{-0.03}$	$42.36^{+0.05}_{-0.02}$	Keck/NIRC2
211138781	0.38	$1.04^{+0.01}_{-0.01}$	$29.72^{+0.2}_{-0.01}$	Keck/NIRC2
211138883	0.38	$1.09^{+0.0}_{-0.01}$	$90.29^{+0.04}_{-0.09}$	Keck/NIRC2

Chapter 7

FUTURE OUTLOOK

We now return to the tasks posed in Chapter 1: 1) to develop the technology to detect the full range of exoplanet masses and orbital parameters, and 2) to understand the formation, dynamics, and physical properties of the planets that are already known. These tasks can be re-stated more specifically as detecting an Earth-mass planet in the habitable zone of a solar-type star and probing its atmosphere for signs of life. This latter task requires spectroscopy, and hence the planet must either transit or be accessible to direct imaging.

Detecting the ~ 80 ppm signal of an Earth-analog transit with $\text{SNR} > 3$ requires more precise photometry than has ever been achieved on the ground (e.g. D. E. Potter, 2006; Zhao et al., 2014); none of the current or near-term space-based missions searching for transiting exoplanets (e.g. K2, TESS, and CHEOPS) will achieve this challenging precision. When such a transiting planet is eventually discovered (the probability of transit for an Earth-analog is a mere 0.47%), obtaining a high-SNR transmission spectrum will be challenging: Kaltenegger and Traub (2009) find that the SNR of the transmission spectral features of an Earth-analog at 10 pc will be less than two for a photon noise limited observation of a single transit by a 6.5-m telescope. A larger space telescope such as the 8 – 16 m Large UV/Optical/IR Surveyor (LUVOIR) concept may be better suited to these observations (Dalcanton et al., 2015).

The prospects for directly imaging Earth-analogs with near-term facilities are also sobering: for an idealized adaptive optics system on a ground-based 30-m telescope, Traub & Oppenheimer conclude that there are no stars bright enough to provide a Shack-Hartmann wavefront sensor with enough signal to deliver the 10^{-10} contrast required to directly image an Earth-analog (S. Seager, 2010). This limitation is ripe for creative solutions – investing in the development of novel schemes for wavefront sensing and control may be our most likely path towards making these challenging detections, given the maturity of 30-m class telescope projects.

Given the current limitations of ground-based adaptive optics, it is possible that Earth-analogs will first be detected with space-based telescopes. Near-term, multi-purpose space telescopes such as JWST and WFIRST, however, are not designed to

achieve the contrast ratios required for such detections. An exception is a possible rendezvous between WFIRST and a starshade – a free-flying “external coronagraph” that occults the starlight before it ever reaches the telescope, lessening the requirements on the telescope system’s wavefront quality (S. Seager, Turnbull, et al., 2015). The outcomes of the WFIRST and starshade efforts will become clear as planning progresses in the next several years.

Perhaps the most appealing avenue for imaging exo-Earths is a dedicated space mission. For example, HabEx is a candidate NASA mission that would be specifically designed to detect biosignatures in the atmospheres of Earth-analogs (B. Mennesson et al., 2016). If HabEx or a space telescope with similar capabilities is selected by the 2020 Decadal Survey in Astronomy and Astrophysics, it could be expected to see first light in the 2030s or beyond.

Detecting and probing the atmosphere of an Earth-analog by any of the above methods will require greater coordination and consensus amongst the exoplanet research community than any other task in the field’s short, eventful history. As the first cohort of astronomers with the tools to realize these goals, we have much to look forward to.

BIBLIOGRAPHY

- Aalo, V. A., G. P. Efthymoglou, and C. Chayawan (2007). “On the envelope and phase distributions for correlated gaussian quadratures”. In: *IEEE Communications Letters* 11.12, pp. 985–987. DOI: 10.1109/LCOMM.2007.071394.
- Adams, Elisabeth R. et al. (2017). “Ultra-short-period Planets in K2 with Companions: A Double Transiting System for EPIC 220674823”. In: *AJ* 153.2, p. 82. DOI: 10.3847/1538-3881/153/2/82.
- Aime, C. and R. Soummer (2004). “The Usefulness and Limits of Coronagraphy in the Presence of Pinned Speckles”. In: *ApJL* 612.1, p. L85. DOI: 10.1086/424381.
- Allard, F., D. Homeier, and B. Freytag (2011). “Model Atmospheres From Very Low Mass Stars to Brown Dwarfs”. In: *16th Cambridge Workshop on Cool Stars, Stellar Systems, and the Sun*. Ed. by C. Johns-Krull, M. K. Browning, and A. A. West. Vol. 448. Astronomical Society of the Pacific Conference Series, p. 91. arXiv: 1011.5405 [astro-ph.SR].
- Amara, Adam and Sascha P. Quanz (2012). “PYNPOINT: An image processing package for finding exoplanets”. In: *MNRAS* 427.2, pp. 948–955. DOI: 10.1111/j.1365-2966.2012.21918.x.
- Apai, Daniel, Markus Kasper, et al. (2016). “High-cadence, High-contrast Imaging for Exoplanet Mapping: Observations of the HR 8799 Planets with VLT/SPHERE Satellite-spot-corrected Relative Photometry”. In: *ApJ* 820.1, p. 40. DOI: 10.3847/0004-637X/820/1/40.
- Apai, Daniel, Jacqueline Radigan, et al. (2013). “HST Spectral Mapping of L/T Transition Brown Dwarfs Reveals Cloud Thickness Variations”. In: *ApJ* 768.2, p. 121. DOI: 10.1088/0004-637X/768/2/121.
- Artigau, É., S. Bouchard, et al. (2009). “Photometric Variability of the T2.5 Brown Dwarf SIMP J013656.5+093347: Evidence for Evolving Weather Patterns”. In: *ApJ* 701, pp. 1534–1539. DOI: 10.1088/0004-637X/701/2/1534. arXiv: 0906.3514 [astro-ph.SR].
- Artigau, É., R. Doyon, et al. (2006). “Discovery of the Brightest T Dwarf in the Northern Hemisphere”. In: *ApJL* 651, pp. L57–L60. DOI: 10.1086/509146. eprint: astro-ph/0609419.
- Atkinson, D. E. et al. (2016). “Next-generation performance of SAPHIRA HgCdTe APDs”. In: *Society of Photo-Optical Instrumentation Engineers (SPIE) Conference Series*. Vol. 9915. Proc. SPIE, 99150N. DOI: 10.1117/12.2234314.
- Baker, I. et al. (2016). “Leonardo (formerly Selex ES) infrared sensors for astronomy: present and future”. In: *Society of Photo-Optical Instrumentation Engineers (SPIE) Conference Series*. Vol. 9915. Proc. SPIE, p. 991505. DOI: 10.1117/12.2231079.

- Baraffe, I. et al. (2015). “New evolutionary models for pre-main sequence and main sequence low-mass stars down to the hydrogen-burning limit”. In: *A&A* 577, A42, A42. DOI: 10.1051/0004-6361/201425481. arXiv: 1503.04107 [astro-ph.SR].
- Baranec, Christoph, Dani Atkinson, et al. (2015). “High-speed Imaging and Wavefront Sensing with an Infrared Avalanche Photodiode Array”. In: *ApJ* 809.1, p. 70. DOI: 10.1088/0004-637X/809/1/70.
- Baranec, Christoph, Reed Riddle, Nicholas M. Law, A. N. Ramaprakash, et al. (2014). “High-efficiency Autonomous Laser Adaptive Optics”. In: *ApJL* 790.1, p. L8. DOI: 10.1088/2041-8205/790/1/L8.
- Baranec, Christoph, Reed Riddle, Nicholas M. Law, A.N. Ramaprakash, et al. (2013). “Bringing the Visible Universe into Focus with Robo-AO”. In: *Journal of Visualized Experiments* 72. DOI: 10.3791/50021.
- Baranec, Christoph, Reed Riddle, A. Ramaprakash, et al. (2011). “Robo-AO: An Autonomous Laser Adaptive Optics and Science System”. In: OSA, AWA2. ISBN: 9781557529145. DOI: 10.1364/AOPT.2011.AWA2.
- Baranec, C. et al. (2012). “Robo-AO: autonomous and replicable laser-adaptive-optics and science system”. In: *Adaptive Optics Systems III*. Vol. 8447. Proc. SPIE, p. 844704. DOI: 10.1117/12.924867. arXiv: 1210.0532 [astro-ph.IM].
- Baranec, C. et al. (2013). “Rise of The Machines: First Year Operations of The Robo-AO Visible-Light Laser-Adaptive-Optics Instrument”. In: *Proceedings of the Advanced Maui Optical and Space Surveillance Technologies Conference, held in Wailea, Maui, Hawaii, September 10-13, 2013, Ed.: S. Ryan, The Maui Economic Development Board*, E48.
- Baranne, A. et al. (1996). “ELODIE: A spectrograph for accurate radial velocity measurements.” In: *A&AS* 119, pp. 373–390.
- Barman, Travis S. et al. (2011). “Clouds and Chemistry in the Atmosphere of Extrasolar Planet HR8799b”. In: *ApJ* 733.1, p. 65. DOI: 10.1088/0004-637X/733/1/65.
- Basri, G. (2000). “Observations of Brown Dwarfs”. In: *ARA&A* 38, pp. 485–519. DOI: 10.1146/annurev.astro.38.1.485.
- Batalha, N. M. (2014). “Exploring exoplanet populations with NASA’s Kepler Mission”. In: *Proceedings of the National Academy of Science* 111, pp. 12647–12654. DOI: 10.1073/pnas.1304196111. arXiv: 1409.1904 [astro-ph.EP].
- Batalha, N. M. et al. (2013). “Planetary Candidates Observed by Kepler. III. Analysis of the First 16 Months of Data”. In: *ApJS* 204, 24, p. 24. DOI: 10.1088/0067-0049/204/2/24. arXiv: 1202.5852 [astro-ph.EP].
- Bauman, S. E. et al. (2014). “Dome venting: the path to thermal balance and superior image quality”. In: *Observatory Operations: Strategies, Processes, and Systems V*. Vol. 9149. Proc. SPIE, 91491K. DOI: 10.1117/12.2056649.

- Beckwith, S. V. W. et al. (1990). “A survey for circumstellar disks around young stellar objects”. In: *AJ* 99, pp. 924–945. doi: 10.1086/115385.
- Berta, Zachory K., Jonathan Irwin, and David Charbonneau (2013). “Constraints on Planet Occurrence around Nearby Mid-to-late M Dwarfs from the MEARTH Project”. In: *ApJ* 775.2, p. 91. doi: 10.1088/0004-637X/775/2/91.
- Beuzit, J.-L. et al. (2008). “SPHERE: a ‘Planet Finder’ instrument for the VLT”. In: *Ground-based and Airborne Instrumentation for Astronomy II*. Vol. 7014. Proc. SPIE, p. 701418. doi: 10.1117/12.790120.
- Biller, B. A. et al. (2006). “Discovery of a Brown Dwarf Very Close to the Sun: A Methane-rich Brown Dwarf Companion to the Low-Mass Star SCR 1845-6357”. In: *ApJL* 641, pp. L141–L144. doi: 10.1086/504256. eprint: astro-ph/0601440.
- Bloemhof, E. E. (2004). “Anomalous intensity of pinned speckles at high adaptive correction”. In: *Optics Letters* 29.2, pp. 159–161. doi: 10.1364/OL.29.000159.
- Bodenheimer, P., O. Hubickyj, and J. J. Lissauer (2000). “Models of the in Situ Formation of Detected Extrasolar Giant Planets”. In: *Icarus* 143, pp. 2–14. doi: 10.1006/icar.1999.6246.
- Bonnefoy, M., T. Currie, et al. (2014). “Characterization of the gaseous companion κ Andromedae b. New Keck and LBTI high-contrast observations”. In: *A&A* 562, A111, A111. doi: 10.1051/0004-6361/201322119. arXiv: 1308.3859 [astro-ph.EP].
- Bonnefoy, M., A.-M. Lagrange, et al. (2011). “High angular resolution detection of β Pictoris b at 2.18 μm ”. In: *A&A* 528, L15, p. L15. doi: 10.1051/0004-6361/201016224.
- Borucki, W. J., D. G. Koch, et al. (2011). “Characteristics of Planetary Candidates Observed by Kepler. II. Analysis of the First Four Months of Data”. In: *ApJ* 736, 19, p. 19. doi: 10.1088/0004-637X/736/1/19. arXiv: 1102.0541 [astro-ph.EP].
- Borucki, W. J., D. Koch, et al. (2010). “Kepler Planet-Detection Mission: Introduction and First Results”. In: *Science* 327, p. 977. doi: 10.1126/science.1185402.
- Bouvier, J., S. P. Matt, et al. (2014). “Angular Momentum Evolution of Young Low-Mass Stars and Brown Dwarfs: Observations and Theory”. In: *Protostars and Planets VI*, pp. 433–450. doi: 10.2458/azu_uapress_9780816531240-ch019. arXiv: 1309.7851 [astro-ph.SR].
- Bouvier, J., F. Rigaut, and D. Nadeau (1997). “Pleiades low-mass binaries: do companions affect the evolution of protoplanetary disks?” In: *A&A* 323, pp. 139–150.
- Bowler, B. P. (2016). “Imaging Extrasolar Giant Planets”. In: *PASP* 128.10, p. 102001. doi: 10.1088/1538-3873/128/968/102001. arXiv: 1605.02731 [astro-ph.EP].

- Bowler, B. P. and L. A. Hillenbrand (2015). “Near-infrared Spectroscopy of 2M0441+2301 AabBab: A Quadruple System Spanning the Stellar to Planetary Mass Regimes”. In: *ApJL* 811, L30, p. L30. doi: 10.1088/2041-8205/811/2/L30. arXiv: 1509.01658 [astro-ph.EP].
- Bowler, Brendan P. et al. (2010). “Near-infrared Spectroscopy of the Extrasolar Planet HR 8799 b”. In: *ApJ* 723.1, p. 850. doi: 10.1088/0004-637X/723/1/850.
- Buenzli, E. and H. M. Schmid (2009). “A grid of polarization models for Rayleigh scattering planetary atmospheres”. In: *A&A* 504.1, pp. 259–276. doi: 10.1051/0004-6361/200911760.
- Burrows, A. et al. (1997). “A Nongray Theory of Extrasolar Giant Planets and Brown Dwarfs”. In: *ApJ* 491, pp. 856–875. doi: 10.1086/305002. eprint: astro-ph/9705201.
- Charbonneau, D., L. E. Allen, et al. (2005). “Detection of Thermal Emission from an Extrasolar Planet”. In: *ApJ* 626, pp. 523–529. doi: 10.1086/429991. eprint: astro-ph/0503457.
- Charbonneau, D., T. M. Brown, et al. (2002). “Detection of an Extrasolar Planet Atmosphere”. In: *ApJ* 568, pp. 377–384. doi: 10.1086/338770. eprint: astro-ph/0111544.
- Chauvin, G. et al. (2004). “A giant planet candidate near a young brown dwarf. Direct VLT/NACO observations using IR wavefront sensing”. In: *A&A* 425, pp. L29–L32. doi: 10.1051/0004-6361:200400056. eprint: astro-ph/0409323.
- Chilcote, J. et al. (2015). “The First H-band Spectrum of the Giant Planet β Pictoris b”. In: *ApJL* 798, L3, p. L3. doi: 10.1088/2041-8205/798/1/L3. arXiv: 1407.4469 [astro-ph.EP].
- Cieza, L. A. et al. (2009). “Primordial Circumstellar Disks in Binary Systems: Evidence for Reduced Lifetimes”. In: *ApJL* 696, pp. L84–L88. doi: 10.1088/0004-637X/696/1/L84. arXiv: 0903.3057 [astro-ph.SR].
- Close, L. M. et al. (2013). “Diffraction-limited Visible Light Images of Orion Trapezium Cluster with the Magellan Adaptive Secondary Adaptive Optics System (MagAO)”. In: *ApJ* 774.2, p. 94. doi: 10.1088/0004-637X/774/2/94.
- Coelho, P. et al. (2007). “Spectral models for solar-scaled and α -enhanced stellar populations”. In: *MNRAS* 382, pp. 498–514. doi: 10.1111/j.1365-2966.2007.12364.x. arXiv: 0708.2790.
- Crepp, J. R., J. A. Johnson, A. W. Howard, G. W. Marcy, J. Brewer, et al. (2014). “The TRENDS High-contrast Imaging Survey. V. Discovery of an Old and Cold Benchmark T-dwarf Orbiting the Nearby G-star HD 19467”. In: *ApJ* 781, 29, p. 29. doi: 10.1088/0004-637X/781/1/29. arXiv: 1311.0280 [astro-ph.EP].

- Crepp, J. R., J. A. Johnson, A. W. Howard, G. W. Marcy, D. A. Fischer, et al. (2012). “The TRENDS High-contrast Imaging Survey. I. Three Benchmark M Dwarfs Orbiting Solar-type Stars”. In: *ApJ* 761, 39, p. 39. doi: 10.1088/0004-637X/761/1/39. arXiv: 1210.3000 [astro-ph.EP].
- Crepp, Justin R. et al. (2015). “Direct Spectrum of the Benchmark T Dwarf HD 19467 B”. In: *ApJL* 798.2, p. L43. doi: 10.1088/2041-8205/798/2/L43.
- Dalcanton, J. et al. (2015). “From Cosmic Birth to Living Earths: The Future of UVOIR Space Astronomy”. In: *ArXiv e-prints*. arXiv: 1507.04779 [astro-ph.IM].
- Dekany, Richard et al. (2013). “PALM-3000: Exoplanet Adaptive Optics for the 5-m Hale Telescope”. In: *ApJ* 776, p. 130. doi: 10.1088/0004-637X/776/2/130.
- Deming, D., S. Seager, L. J. Richardson, et al. (2005). “Infrared radiation from an extrasolar planet”. In: *Nature* 434, pp. 740–743. doi: 10.1038/nature03507. eprint: astro-ph/0503554.
- Deming, D., S. Seager, J. Winn, et al. (2009). “Discovery and Characterization of Transiting Super Earths Using an All-Sky Transit Survey and Follow-up by the James Webb Space Telescope”. In: *PASP* 121, pp. 952–967. doi: 10.1086/605913. arXiv: 0903.4880 [astro-ph.EP].
- Dhillon, V. and T. Marsh (2001). “ULTRACAM - studying astrophysics on the fastest timescales”. In: *NewAR* 45, pp. 91–95. doi: 10.1016/S1387-6473(00)00136-6.
- Dohlen, K. et al. (2008). “The infra-red dual imaging and spectrograph for SPHERE: design and performance”. In: *Ground-based and Airborne Instrumentation for Astronomy II*. Vol. 7014. Proc. SPIE, p. 70143L. doi: 10.1117/12.789786.
- Dressing, Courtney D. and David Charbonneau (2013). “The Occurrence Rate of Small Planets around Small Stars”. In: *ApJ* 767, p. 95. doi: 10.1088/0004-637X/767/1/95.
- Dumusque, Xavier et al. (2012). “An Earth-mass planet orbiting Alpha Centauri B”. In: *Nature* 491.7423, pp. 207–211. doi: 10.1038/nature11572.
- Dumusque, X. et al. (2011). “Planetary detection limits taking into account stellar noise. I. Observational strategies to reduce stellar oscillation and granulation effects”. In: *A&A* 525, A140, A140. doi: 10.1051/0004-6361/201014097. arXiv: 1010.2616 [astro-ph.EP].
- Erskine, D. J. (2003). “An Externally Dispersed Interferometer Prototype for Sensitive Radial Velocimetry: Theory and Demonstration on Sunlight”. In: *PASP* 115, pp. 255–269. doi: 10.1086/345995.
- Erskine, D. J. et al. (2003). “High-Resolution Broadband Spectroscopy Using an Externally Dispersed Interferometer”. In: *ApJL* 592, pp. L103–L106. doi: 10.1086/377703.

- Fitzgerald, Michael P. and James R. Graham (2006). “Speckle Statistics in Adaptively Corrected Images”. In: *ApJ* 637.1, p. 541. DOI: 10.1086/498339.
- Fried, D. L. (1966). “Optical Resolution Through a Randomly Inhomogeneous Medium for Very Long and Very Short Exposures”. In: *Journal of the Optical Society of America (1917-1983)* 56, p. 1372.
- Fruchter, A. S. and R. N. Hook (2002). “Drizzle: A Method for the Linear Reconstruction of Undersampled Images”. In: *PASP* 114.792, p. 144. DOI: 10.1086/338393.
- Gallet, F. and J. Bouvier (2013). “Improved angular momentum evolution model for solar-like stars”. In: *A&A* 556, A36, A36. DOI: 10.1051/0004-6361/201321302. arXiv: 1306.2130 [astro-ph.SR].
- Ge, J. et al. (2006). “The First Extrasolar Planet Discovered with a New-Generation High-Throughput Doppler Instrument”. In: *ApJ* 648, pp. 683–695. DOI: 10.1086/505699. eprint: arXiv:astro-ph/0605247.
- Ghosh, P. and F. K. Lamb (1979). “Accretion by rotating magnetic neutron stars. III - Accretion torques and period changes in pulsating X-ray sources”. In: *ApJ* 234, pp. 296–316. DOI: 10.1086/157498.
- Gilmozzi, R. and J. Spyromilio (2007). “The European Extremely Large Telescope (E-ELT)”. In: *The Messenger* 127.
- Goldman, B. et al. (2009). “Polarisation of very-low-mass stars and brown dwarfs. I. VLT/FORS1 optical observations of field ultra-cool dwarfs”. In: *A&A* 502, pp. 929–936. DOI: 10.1051/0004-6361/200811152. arXiv: 0904.0005 [astro-ph.SR].
- Gomez Gonzalez, C. A. et al. (2016). “Low-rank plus sparse decomposition for exoplanet detection in direct-imaging ADI sequences - The LLSG algorithm”. In: *A&A* 589, A54. DOI: 10.1051/0004-6361/201527387.
- Greenwood, D. P. (1977). “Bandwidth specification for adaptive optics systems”. In: *Journal of the Optical Society of America (1917-1983)* 67, pp. 390–393.
- Guyon, O. (2005). “Limits of Adaptive Optics for High-Contrast Imaging”. In: *ApJ* 629, pp. 592–614. DOI: 10.1086/431209. eprint: astro-ph/0505086.
- Guyon, O., E. A. Pluzhnik, et al. (2006). “Theoretical Limits on Extrasolar Terrestrial Planet Detection with Coronagraphs”. In: *ApJS* 167.1, p. 81. DOI: 10.1086/507630.
- Guyon, O., C. Roddier, et al. (1999). “The Nulling Stellar Coronagraph: Laboratory Tests and Performance Evaluation”. In: *PASP* 111, pp. 1321–1330. DOI: 10.1086/316445.
- Hajian, A. R. et al. (2007). “Initial Results from the USNO Dispersed Fourier Transform Spectrograph”. In: *ApJ* 661, pp. 616–633. DOI: 10.1086/513181. eprint: arXiv:astro-ph/0611495.

- Hardy, John W. (1998). *Adaptive Optics for Astronomical Telescopes*. Oxford Series in Optical and Imaging Sciences. Oxford, New York: Oxford University Press. ISBN: 9780195090192.
- Hartmann, J. (1900). “Bemerkungen über den Bau und die Justirung von Spektrographen”. In: *Zeitschrift Für Instrumentenkunde* 20, pp. 17–58.
- Hartmann, L. and J. R. Stauffer (1989). “Additional measurements of pre-main-sequence stellar rotation”. In: *AJ* 97, pp. 873–880. DOI: 10.1086/115033.
- Hayashi, M. R., K. Shibata, and R. Matsumoto (1996). “X-Ray Flares and Mass Outflows Driven by Magnetic Interaction between a Protostar and Its Surrounding Disk”. In: *ApJL* 468, p. L37. DOI: 10.1086/310222. eprint: astro-ph/9606157.
- Hinkley, Sasha, Ben R. Oppenheimer, R emi Soummer, et al. (2009). “Speckle Suppression Through Dual Imaging Polarimetry, and a Ground-based Image of the HR 4796A Circumstellar Disk”. In: *ApJ* 701.1, p. 804. DOI: 10.1088/0004-637X/701/1/804.
- Hinkley, Sasha, Ben R. Oppenheimer, R. Soummer, et al. (2007). “Temporal Evolution of Coronagraphic Dynamic Range and Constraints on Companions to Vega”. In: *ApJ* 654.1, p. 633. DOI: 10.1086/509063.
- Hinkley, S. et al. (2011). “A New High Contrast Imaging Program at Palomar Observatory”. In: *PASP* 123, p. 74. DOI: 10.1086/658163. arXiv: 1012.0008 [astro-ph.IM].
- Howard, A. W. et al. (2010). “The Occurrence and Mass Distribution of Close-in Super-Earths, Neptunes, and Jupiters”. In: *Science* 330, pp. 653–. DOI: 10.1126/science.1194854. arXiv: 1011.0143 [astro-ph.EP].
- Howard, Andrew W., John Asher Johnson, et al. (2011). “The NASA-UC Eta-Earth Program. II. A Planet Orbiting HD 156668 with a Minimum Mass of Four Earth Masses”. In: *ApJ* 726, p. 73. DOI: 10.1088/0004-637X/726/2/73.
- Howard, Andrew W., Geoffrey W. Marcy, et al. (2012). “Planet Occurrence within 0.25 AU of Solar-type Stars from Kepler”. In: *ApJS* 201, p. 15. DOI: 10.1088/0067-0049/201/2/15.
- Ingraham, Patrick et al. (2014). “Gemini Planet Imager Spectroscopy of the HR 8799 Planets c and d”. In: *ApJL* 794.1, p. L15. DOI: 10.1088/2041-8205/794/1/L15.
- Jensen, E. L. N., R. D. Mathieu, and G. A. Fuller (1996). “The Connection between Submillimeter Continuum Flux and Binary Separation in Young Binaries: Evidence of Interaction between Stars and Disks”. In: *ApJ* 458, p. 312. DOI: 10.1086/176814. eprint: astro-ph/9508099.
- Kaltenegger, L. and W. A. Traub (2009). “Transits of Earth-like Planets”. In: *ApJ* 698, pp. 519–527. DOI: 10.1088/0004-637X/698/1/519. arXiv: 0903.3371 [astro-ph.IM].

- Kasdin, N. Jeremy and Isabelle Braems (2006). “Linear and Bayesian Planet Detection Algorithms for the Terrestrial Planet Finder”. In: *ApJ* 646.2, p. 1260. DOI: 10.1086/505017.
- Knutson, H. A. et al. (2007). “A map of the day-night contrast of the extrasolar planet HD 189733b”. In: *Nature* 447, pp. 183–186. DOI: 10.1038/nature05782. arXiv: 0705.0993.
- Koch, D. G. et al. (2010). “Kepler Mission Design, Realized Photometric Performance, and Early Science”. In: *ApJL* 713, pp. L79–L86. DOI: 10.1088/2041-8205/713/2/L79. arXiv: 1001.0268 [astro-ph.EP].
- Kok, R. J. de, D. M. Stam, and T. Karalidi (2011). “Characterizing Exoplanetary Atmospheres through Infrared Polarimetry”. In: *ApJ* 741.1, p. 59. DOI: 10.1088/0004-637X/741/1/59.
- Krist, John, Bijan Nemati, and Bertrand Mennesson (2015). “Numerical modeling of the proposed WFIRST-AFTA coronagraphs and their predicted performances”. In: *Journal of Astronomical Telescopes, Instruments, and Systems* 2.1, pp. 011003–011003. DOI: 10.1117/1.JATIS.2.1.011003.
- Kuhn, J. R., D. Potter, and B. Parise (2001). “Imaging Polarimetric Observations of a New Circumstellar Disk System”. In: *ApJL* 553, pp. L189–L191. DOI: 10.1086/320686. eprint: astro-ph/0105239.
- Lafrenière, David, Christian Marois, Rene Doyon, et al. (2009). “HST/NICMOS Detection of HR 8799 b in 1998”. In: *ApJL* 694.2, p. L148. DOI: 10.1088/0004-637X/694/2/L148.
- Lafrenière, David, Christian Marois, Renè Doyon, et al. (2007). “A New Algorithm for Point-Spread Function Subtraction in High-Contrast Imaging: A Demonstration with Angular Differential Imaging”. In: *ApJ* 660.1, p. 770. DOI: 10.1086/513180.
- Law, N. M., C. Baranec, and R. L. Riddle (2014). “Twelve thousand laser-AO observations: first results from the Robo-AO large surveys”. In: *Adaptive Optics Systems IV*. Vol. 9148. Proc. SPIE, 91480A. DOI: 10.1117/12.2056994.
- Liu, Michael C. (2004). “Substructure in the Circumstellar Disk Around the Young Star AU Microscopii”. In: *Science* 305.5689, pp. 1442–1444. DOI: 10.1126/science.1102929.
- Lovis, C. and F. Pepe (2007). “A new list of thorium and argon spectral lines in the visible”. In: *A&A* 468, pp. 1115–1121. DOI: 10.1051/0004-6361:20077249.
- Liot, B. (1939). “The study of the solar corona and prominences without eclipses (George Darwin Lecture, 1939)”. In: *MNRAS* 99, p. 580. DOI: 10.1093/mnras/99.8.580.
- Liot, Barnard (1929). In: *Ann. Observ. Paris (Meudon)* 8, p. 161.

- Macintosh, B. A. et al. (2008). “The Gemini Planet Imager: from science to design to construction”. In: *Adaptive Optics Systems*. Vol. 7015. Proc. SPIE, p. 701518. DOI: 10.1117/12.788083.
- Macintosh, Bruce et al. (2014). “First light of the Gemini Planet Imager”. In: *Proceedings of the National Academy of Sciences* 111.35, pp. 12661–12666. DOI: 10.1073/pnas.1304215111.
- Macintosh, B. et al. (2015). “Discovery and spectroscopy of the young jovian planet 51 Eri b with the Gemini Planet Imager”. In: *Science* 350, pp. 64–67. DOI: 10.1126/science.aac5891. arXiv: 1508.03084 [astro-ph.EP].
- Mahadevan, Suvrath et al. (2008). “Measuring Stellar Radial Velocities with a Dispersed Fixed-Delay Interferometer”. In: *ApJ* 678, pp. 1505–1510. DOI: 10.1086/533514.
- Maire, J. et al. (2010). “Data reduction pipeline for the Gemini Planet Imager”. In: *Ground-based and Airborne Instrumentation for Astronomy III*. Vol. 7735. Proc. SPIE, p. 773531. DOI: 10.1117/12.858028.
- Marley, M. S. et al. (2012). “Masses, Radii, and Cloud Properties of the HR 8799 Planets”. In: *ApJ* 754, 135, p. 135. DOI: 10.1088/0004-637X/754/2/135. arXiv: 1205.6488 [astro-ph.EP].
- Marley, Mark S. and Sujana Sengupta (2011). “Probing the physical properties of directly imaged gas giant exoplanets through polarization”. In: *MNRAS* 417.4, pp. 2874–2881. DOI: 10.1111/j.1365-2966.2011.19448.x.
- Marois, C., R. Doyon, et al. (2005). “TRIDENT: An Infrared Differential Imaging Camera Optimized for the Detection of Methanated Substellar Companions”. In: *PASP* 117, pp. 745–756. DOI: 10.1086/431347. eprint: astro-ph/0504652.
- Marois, C., D. Lafrenière, R. Doyon, et al. (2006). “Angular Differential Imaging: A Powerful High-Contrast Imaging Technique”. In: *ApJ* 641, pp. 556–564. DOI: 10.1086/500401. eprint: astro-ph/0512335.
- Marois, C., D. Lafrenière, B. Macintosh, et al. (2008). “Confidence Level and Sensitivity Limits in High-Contrast Imaging”. In: *ApJ* 673, 647-656, pp. 647–656. DOI: 10.1086/523839. arXiv: 0709.3548.
- Marois, Christian, René Doyon, et al. (2000). “Efficient Speckle Noise Attenuation in Faint Companion Imaging”. In: *PASP* 112.767, p. 91. DOI: 10.1086/316492.
- Marois, Christian, Bruce Macintosh, et al. (2008). “Direct Imaging of Multiple Planets Orbiting the Star HR 8799”. In: *Science* 322.5906, pp. 1348–1352. DOI: 10.1126/science.1166585.
- Mawet, D. et al. (2014). “Fundamental Limitations of High Contrast Imaging Set by Small Sample Statistics”. In: *ApJ* 792.2, p. 97. DOI: 10.1088/0004-637X/792/2/97.

- Mayor, M. and D. Queloz (1995). “A Jupiter-mass companion to a solar-type star”. In: *Nature* 378, pp. 355–359. doi: 10.1038/378355a0.
- Melis, C. et al. (2014). “A VLBI resolution of the Pleiades distance controversy”. In: *Science* 345, pp. 1029–1032. doi: 10.1126/science.1256101. arXiv: 1408.6544 [astro-ph.SR].
- Ménard, F., X. Delfosse, and J.-L. Monin (2002). “Optical linear polarimetry of ultra cool dwarfs”. In: *A&A* 396.3, pp. L35–L38. doi: 10.1051/0004-6361/20021657.
- Mennesson, B. et al. (2016). “The Habitable Exoplanet (HabEx) Imaging Mission: preliminary science drivers and technical requirements”. In: *Space Telescopes and Instrumentation 2016: Optical, Infrared, and Millimeter Wave*. Vol. 9904. Proc. SPIE, p. 99040L. doi: 10.1117/12.2240457.
- Metchev, S. A. et al. (2015). “Weather on Other Worlds. II. Survey Results: Spots are Ubiquitous on L and T Dwarfs”. In: *ApJ* 799, 154, p. 154. doi: 10.1088/0004-637X/799/2/154. arXiv: 1411.3051 [astro-ph.SR].
- Miles-Páez, P. A. et al. (2013). “Linear polarization of rapidly rotating ultracool dwarfs”. In: *A&A* 556, A125, A125. doi: 10.1051/0004-6361/201321851. arXiv: 1306.6314 [astro-ph.SR].
- Millar-Blanchaer, M. A. et al. (2015). “Beta Pictoris’ Inner Disk in Polarized Light and New Orbital Parameters for Beta Pictoris b”. In: *ApJ* 811, 18, p. 18. doi: 10.1088/0004-637X/811/1/18. arXiv: 1508.04787 [astro-ph.EP].
- Muirhead, P. S. et al. (2011). “Precise Stellar Radial Velocities of an M Dwarf with a Michelson Interferometer and a Medium-Resolution Near-Infrared Spectrograph”. In: *PASP* 123, p. 709. doi: 10.1086/660802. arXiv: 1103.0004 [astro-ph.IM].
- Murphy, M. T. et al. (2007). “High-precision wavelength calibration of astronomical spectrographs with laser frequency combs”. In: *MNRAS* 380.2. arXiv:astro-ph/0703622, pp. 839–847. doi: 10.1111/j.1365-2966.2007.12147.x.
- Ngo, H. et al. (2015). “Friends of Hot Jupiters. II. No Correspondence between Hot-Jupiter Spin-Orbit Misalignment and the Incidence of Directly Imaged Stellar Companions”. In: *ApJ* 800, 138, p. 138. doi: 10.1088/0004-637X/800/2/138. arXiv: 1501.00013 [astro-ph.EP].
- Oppenheimer, B. R. et al. (2008). “The Solar-System-Scale Disk around AB Aurigae”. In: *ApJ* 679, 1574-1581, pp. 1574–1581. doi: 10.1086/587778. arXiv: 0803.3629.
- Osorio, M. R. Zapatero, J. A. Caballero, and V. J. S. Bejar (2005). “Optical Linear Polarization of Late M and L Type Dwarfs”. In: *ApJ* 621.1, p. 445. doi: 10.1086/427433.

- Ostriker, E. C. and F. H. Shu (1995). “Magnetocentrifugally Driven Flows from Young Stars and Disks. IV. The Accretion Funnel and Dead Zone”. In: *ApJ* 447, p. 813. DOI: 10.1086/175920.
- Otten, Gilles P. P. L. et al. (2017). “On-sky Performance Analysis of the Vector Apodizing Phase Plate Coronagraph on MagAO/Clio2”. In: *ApJ* 834.2, p. 175. DOI: 10.3847/1538-4357/834/2/175.
- Papaloizou, J. and J. E. Pringle (1977). “Tidal torques on accretion discs in close binary systems”. In: *MNRAS* 181, pp. 441–454. DOI: 10.1093/mnras/181.3.441.
- Patience, J. et al. (2002). “A High Angular Resolution Multiplicity Survey of the Open Clusters α Persei and Praesepe”. In: *AJ* 123, pp. 1570–1602. DOI: 10.1086/338431. eprint: astro-ph/0111156.
- Pepe, F. et al. (2011). “The HARPS search for Earth-like planets in the habitable zone: I. Very low-mass planets around HD 20794, HD 85512, and HD 192310”. In: *A&A* 534, A58. DOI: 10.1051/0004-6361/201117055.
- Perrin, M. D., J. R. Graham, et al. (2004). “Laser Guide Star Adaptive Optics Imaging Polarimetry of Herbig Ae/Be Stars”. In: *Science* 303, pp. 1345–1348. DOI: 10.1126/science.1094602. eprint: astro-ph/0402615.
- Perrin, M. D., J. Maire, et al. (2014). “Gemini Planet Imager observational calibrations I: Overview of the GPI data reduction pipeline”. In: *Ground-based and Airborne Instrumentation for Astronomy V*. Vol. 9147. Proc. SPIE, 91473J. DOI: 10.1117/12.2055246. arXiv: 1407.2301 [astro-ph.IM].
- Perrin, Marshall D., Gaspard Duchene, et al. (2015). “Polarimetry with the Gemini Planet Imager: Methods, Performance at First Light, and the Circumstellar Ring around HR 4796A”. In: *ApJ* 799.2, p. 182. DOI: 10.1088/0004-637X/799/2/182.
- Perrin, Marshall D., Anand Sivaramakrishnan, et al. (2003). “The Structure of High Strehl Ratio Point-Spread Functions”. In: *ApJ* 596.1, p. 702. DOI: 10.1086/377689.
- Perryman, Michael (2011). *The Exoplanet Handbook*. Cambridge University Press. ISBN: 978-1-139-49851-7.
- Perryman, M. et al. (2014). “Astrometric Exoplanet Detection with Gaia”. In: *ApJ* 797, 14, p. 14. DOI: 10.1088/0004-637X/797/1/14. arXiv: 1411.1173 [astro-ph.EP].
- Petigura, E. A., A. W. Howard, and G. W. Marcy (2013). “Prevalence of Earth-size planets orbiting Sun-like stars”. In: *Proceedings of the National Academy of Science* 110, pp. 19273–19278. DOI: 10.1073/pnas.1319909110. arXiv: 1311.6806 [astro-ph.EP].
- Pollack, J. B. et al. (1996). “Formation of the Giant Planets by Concurrent Accretion of Solids and Gas”. In: *Icarus* 124, pp. 62–85. DOI: 10.1006/icar.1996.0190.

- Potter, D. E. (2006). “High Precision Differential Photometry of the Transit and Secondary Eclipse of HD209458b”. In: *AAS Meeting Abstracts*. Vol. 38. Bulletin of the American Astronomical Society, p. 1173.
- Pueyo, Laurent (2016). “Detection and Characterization of Exoplanets using Projections on Karhunen Loeve Eigenimages: Forward Modeling”. In: *ApJ* 824.2, p. 117. DOI: 10.3847/0004-637X/824/2/117.
- Racine, R. et al. (1999). “Speckle Noise and the Detection of Faint Companions”. In: *PASP* 111, pp. 587–594. DOI: 10.1086/316367.
- Radigan, Jacqueline et al. (2014). “Strong Brightness Variations Signal Cloudy-to-Clear Transition of Brown Dwarfs”. In: *ApJ* 793.2, p. 75. DOI: 10.1088/0004-637X/793/2/75.
- Radigan, J. et al. (2012). “Large-amplitude Variations of an L/T Transition Brown Dwarf: Multi-wavelength Observations of Patchy, High-contrast Cloud Features”. In: *ApJ* 750, 105, p. 105. DOI: 10.1088/0004-637X/750/2/105. arXiv: 1201.3403 [astro-ph.SR].
- Rebull, L. M. et al. (2016). “Rotation in the Pleiades with K2. I. Data and First Results”. In: *AJ* 152, 113, p. 113. DOI: 10.3847/0004-6256/152/5/113. arXiv: 1606.00052 [astro-ph.SR].
- Ricker, G. R. (2014). “The Transiting Exoplanet Survey Satellite Mission”. In: *Journal of the American Association of Variable Star Observers (JAAVSO)* 42, p. 234.
- Riddle, R. L. et al. (2014). “The Robo-AO automated intelligent queue system”. In: *Software and Cyberinfrastructure for Astronomy III*. Vol. 9152. Proc. SPIE, 91521E. DOI: 10.1117/12.2056534. arXiv: 1407.4484 [astro-ph.IM].
- Robinson, Tyler D. and Mark S. Marley (2014). “Temperature Fluctuations as a Source of Brown Dwarf Variability”. In: *ApJ* 785.2, p. 158. DOI: 10.1088/0004-637X/785/2/158.
- Rybicki, George B. and Alan P. Lightman (1979). *Radiative Processes in Astrophysics*. John Wiley & Sons. ISBN: 978-0-471-82759-7.
- Salama, M. et al. (2016). “Robo-AO Kitt Peak: status of the system and deployment of a sub-electron readnoise IR camera to detect low-mass companions”. In: *Society of Photo-Optical Instrumentation Engineers (SPIE) Conference Series*. Vol. 9909. Proc. SPIE, 99091A. DOI: 10.1117/12.2233741. arXiv: 1608.02985 [astro-ph.IM].
- Samuele, R. et al. (2007). “Experimental Progress and Results of a Visible Nulling Coronagraph”. In: *2007 IEEE Aerospace Conference*, pp. 1–7. DOI: 10.1109/AERO.2007.353077.
- Schmid, H. M. et al. (2006). “Search and investigation of extra-solar planets with polarimetry”. In: *IAU Colloq. 200: Direct Imaging of Exoplanets: Science & Techniques*. Ed. by C. Aime and F. Vakili, pp. 165–170. DOI: 10.1017/S1743921306009252.

- Seager, S. and D. Deming (2010). “Exoplanet Atmospheres”. In: *ARA&A* 48, pp. 631–672. DOI: 10.1146/annurev-astro-081309-130837. arXiv: 1005.4037 [astro-ph.EP].
- Seager, S., M. Turnbull, et al. (2015). “The Exo-S probe class starshade mission”. In: *Techniques and Instrumentation for Detection of Exoplanets VII*. Vol. 9605. Proc. SPIE, 96050W. DOI: 10.1117/12.2190378.
- Seager, Sara (2010). *Exoplanets*. University of Arizona Press. ISBN: 978-0-8165-2945-2.
- Sengupta, Sujan and Vinod Krishan (2001). “Probing Dust in the Atmosphere of Brown Dwarfs through Polarization”. In: *ApJL* 561.1, p. L123. DOI: 10.1086/324559.
- Sengupta, Sujan and Mark S. Marley (2009). “Multiple Scattering Polarization of Substellar-mass Objects: T Dwarfs”. In: *ApJ* 707.1, p. 716. DOI: 10.1088/0004-637X/707/1/716.
- Shack, R. V. and B. C. Platt (1971). “Production and Use of a Lenticular Hartmann Screen”. In: *Spring Meeting of the Optical Society of America*. Ed. by Dow S. Chairman. Optical Society of America. Tucson, Arizona: Optical Society of America.
- Shaklan, Stuart and Francois Roddier (1988). “Coupling starlight into single-mode fiber optics”. In: *Applied Optics* 27.11, p. 2334. DOI: 10.1364/AO.27.002334.
- Shapiro, S. S. and M. B. Wilk (1965). “An Analysis of Variance Test for Normality (Complete Samples)”. In: *Biometrika* 52.3/4, pp. 591–611. DOI: 10.2307/2333709.
- Sheehy, C. D., N. McCrady, and J. R. Graham (2006). “Constraining the Adaptive Optics Point-Spread Function in Crowded Fields: Measuring Photometric Aperture Corrections”. In: *ApJ* 647, pp. 1517–1530. DOI: 10.1086/505524. eprint: astro-ph/0604551.
- Shi, Fang et al. (2016). “Low-order wavefront sensing and control for WFIRST-AFTA coronagraph”. In: *Journal of Astronomical Telescopes, Instruments, and Systems* 2.1, pp. 011021–011021. DOI: 10.1117/1.JATIS.2.1.011021.
- Shu, F. H. et al. (1988). “Mass loss from rapidly rotating magnetic protostars”. In: *ApJL* 328, pp. L19–L23. DOI: 10.1086/185152.
- Simon, M. et al. (1995). “A lunar occultation and direct imaging survey of multiplicity in the Ophiuchus and Taurus star-forming regions”. In: *ApJ* 443, pp. 625–637. DOI: 10.1086/175554.
- Soummer, R., L. Pueyo, and J. Larkin (2012). “Detection and Characterization of Exoplanets and Disks Using Projections on Karhunen-Loève Eigenimages”. In: *ApJL* 755, L28, p. L28. DOI: 10.1088/2041-8205/755/2/L28. arXiv: 1207.4197 [astro-ph.IM].

- Soummer, R. et al. (2007). “Speckle Noise and Dynamic Range in Coronagraphic Images”. In: *ApJ* 669.1, p. 642. DOI: 10.1086/520913.
- Sparks, W. B. and H. C. Ford (2002). “Imaging Spectroscopy for Extrasolar Planet Detection”. In: *ApJ* 578, pp. 543–564. DOI: 10.1086/342401. eprint: astro-ph/0209078.
- Spergel, D. et al. (2015). “Wide-Field Infrared Survey Telescope-Astrophysics Focused Telescope Assets WFIRST-AFTA 2015 Report”. In: *ArXiv e-prints*. arXiv: 1503.03757 [astro-ph.IM].
- Stam, D. M. (2008). “Spectropolarimetric signatures of Earth-like extrasolar planets”. In: *A&A* 482.3, pp. 989–1007. DOI: 10.1051/0004-6361:20078358.
- Stauffer, J. R., G. Schultz, and J. D. Kirkpatrick (1998). “Keck Spectra of Pleiades Brown Dwarf Candidates and a Precise Determination of the Lithium Depletion Edge in the Pleiades”. In: *ApJL* 499, pp. L199–L203. DOI: 10.1086/311379. eprint: astro-ph/9804005.
- Stauffer, J. et al. (2016). “Rotation in the Pleiades with K2. III. Speculations on Origins and Evolution”. In: *AJ* 152, 115, p. 115. DOI: 10.3847/0004-6256/152/5/115. arXiv: 1606.00057 [astro-ph.SR].
- Steinmetz, T. et al. (2008). “Laser Frequency Combs for Astronomical Observations”. In: *Science* 321, pp. 1335–. DOI: 10.1126/science.1161030. arXiv: 0809.1663.
- Stevenson, D. J. (1982). “Formation of the giant planets”. In: *Planet. Space Sci.* 30, pp. 755–764. DOI: 10.1016/0032-0633(82)90108-8.
- Strand, K. A. (1943). “61 Cygni as a Triple System”. In: *PASP* 55, pp. 29–32. DOI: 10.1086/125484.
- Struve, O. (1952). “Proposal for a project of high-precision stellar radial velocity work”. In: *The Observatory* 72, pp. 199–200.
- Student (1908). “The Probable Error of a Mean”. In: *Biometrika* 6.1, pp. 1–25. DOI: 10.2307/2331554.
- Swets, J., W. P. Tanner, and T. G. Birdsall (1961). “Decision processes in perception”. eng. In: *Psychological Review* 68, pp. 301–340.
- Tanner, W. P. and J. A. Swets (1954). “A decision-making theory of visual detection”. eng. In: *Psychological Review* 61.6, pp. 401–409.
- Tata, R. et al. (2009). “Optical linear polarization in ultra cool dwarfs - A tool to probe dust in the ultra cool dwarf atmospheres”. In: *A&A* 508.3, pp. 1423–1427. DOI: 10.1051/0004-6361/200911830.
- Uyama, T. et al. (2017). “The SEEDS High-Contrast Imaging Survey of Exoplanets Around Young Stellar Objects”. In: *AJ* 153, 106, p. 106. DOI: 10.3847/1538-3881/153/3/106. arXiv: 1604.04697 [astro-ph.EP].

- van Eyken, J. C., J. Ge, and S. Mahadevan (2010). “Theory of Dispersed Fixed-delay Interferometry for Radial Velocity Exoplanet Searches”. In: *ApJS* 189, pp. 156–180. DOI: 10.1088/0067-0049/189/1/156. arXiv: 1005.5564 [astro-ph.IM].
- Vanderburg, Andrew, Juliette C. Becker, et al. (2016). “Five Planets Transiting a Ninth Magnitude Star”. In: *ApJL* 827.1, p. L10. DOI: 10.3847/2041-8205/827/1/L10.
- Vanderburg, Andrew, Allyson Bieryla, et al. (2016). “Two Small Planets Transiting HD 3167”. In: *ApJL* 829.1, p. L9. DOI: 10.3847/2041-8205/829/1/L9.
- Wahhaj, Zahed et al. (2013). “The Gemini NICI Planet-Finding Campaign: The Companion Detection Pipeline”. In: *ApJ* 779, p. 80. DOI: 10.1088/0004-637X/779/1/80.
- Wertz, Olivier et al. (2017). “VLT/SPHERE robust astrometry of the HR8799 planets at milliarcsecond-level accuracy Orbital architecture analysis with PyAstrOFit”. In: *A&A* 598, A83.
- Wiktorowicz, S. J. et al. (2014). “Gemini planet imager observational calibrations VII: on-sky polarimetric performance of the Gemini planet imager”. In: *Ground-based and Airborne Instrumentation for Astronomy V*. Vol. 9147. Proc. SPIE, p. 914783. DOI: 10.1117/12.2056616. arXiv: 1407.2307 [astro-ph.IM].
- Wilcox, Rand R. (2009). *Basic Statistics: Understanding Conventional Methods and Modern Insights*. Oxford University Press. ISBN: 978-0-19-804301-0.
- Wilken, Tobias et al. (2012). “A spectrograph for exoplanet observations calibrated at the centimetre-per-second level”. In: *Nature* 485.7400, pp. 611–614. DOI: 10.1038/nature11092.
- Wilson, R. E. (1953). “General catalogue of stellar radial velocities.” In: *Carnegie Institute Washington D.C. Publication*.
- Young, E. J., N. J. Kasdin, and A. Carlotti (2013). “Image analysis with speckles altered by a deformable mirror”. In: *Techniques and Instrumentation for Detection of Exoplanets VI*. Vol. 8864. Proc. SPIE, 88640S. DOI: 10.1117/12.2025061.
- Zapatero Osorio, M. R. et al. (2011). “Near-infrared Linear Polarization of Ultracool Dwarfs”. In: *ApJ* 740, 4, p. 4. DOI: 10.1088/0004-637X/740/1/4. arXiv: 1107.2498 [astro-ph.SR].
- Zhao, M. et al. (2014). “A Survey of the Hottest Jupiter Atmospheres via Secondary Eclipses”. In: *AAS Meeting Abstracts#223*. Vol. 223. AAS Meeting Abstracts, p. 207.06.
- Zurlo, A. et al. (2016). “First light of the VLT planet finder SPHERE - III. New spectrophotometry and astrometry of the HR 8799 exoplanetary system”. In: *A&A* 587, A57. DOI: 10.1051/0004-6361/201526835.